DESIGN AND ANALYSIS OF BOOMS FOR WHEELED MOBILE PLATFORM FOR CROP PHENOTYPING

A Thesis Submitted to the
College of Graduate and Postdoctoral Studies
In Partial Fulfillment of the Requirements
For the Degree of Master of Science
In the Department of Mechanical Engineering
University of Saskatchewan
Saskatoon

By

Qianwei Zhang

© Copyright Qianwei Zhang, December, 2018. All rights reserved.

Permission to Use

In presenting this thesis/dissertation in partial fulfillment of the requirements for a Postgraduate degree from the University of Saskatchewan, I agree that the Libraries of this University may make it freely available for inspection. I further agree that permission for copying of this thesis/dissertation in any manner, in whole or in part, for scholarly purposes may be granted by the professor or professors who supervised my thesis/dissertation work or, in their absence, by the Head of the Department or the Dean of the College in which my thesis work was done. It is understood that any copying or publication or use of this thesis/dissertation or parts thereof for financial gain shall not be allowed without my written permission. It is also understood that due recognition shall be given to me and to the University of Saskatchewan in any scholarly use which may be made of any material in my thesis/dissertation.

Requests for permission to copy or to make other uses of materials in this thesis/dissertation in whole or part should be addressed to:

Head of the Department of Mechanical Engineering
University of Saskatchewan, College of Engineering
3B48 Engineering Building, 57 Campus Drive
Saskatoon, Saskatchewan, S7N 5A9, Canada

OR

Dean
College of Graduate and Postdoctoral Studies
University of Saskatchewan
116 Thorvaldson Building, 110 Science Place
Saskatoon, Saskatchewan S7N 5C9 Canada

Abstract

Crop phenotyping is frequently used by breeders and crop scientists to monitor the growth of plants and to relate them to genotypes of plants. Seemingly, this contributes to better crop growth and results in higher yield in solving food insecurity from growing world population. Instead of traditional crop monitoring, which is labor intensive, high-throughput phenotyping (HTP) using ground-based vehicle has several advantages over manual methods. Equipped with advanced sensors, the high-throughput phenotyping platforms quickly, accurately, and automatically, measure and record plant traits, such as appearance, height, and temperature.

Although there have been many studies on plant phenotyping, there is still needs for ground-based HTP platform to perform accurate phenotyping on targeted crops (e.g. canola and wheat). Previous studies using ground-based HTP platforms focus primarily on leafy plants rather than densely cultivated crops. Besides, the previous platforms are designed for specific vehicles or sensors, and they are inappropriate for canola or wheat, which are targeted crops of this study. In this research, the main objective is to develop appropriate mechanical structures that are attached to different wheeled mobile platforms for HTP study. Using sensors attached to these mechanical booms, data are collected automatically for several traits such as height, temperature, greenness, and photos. These collected data are compared with manual measured data to evaluate the performance of the system, including suitability of mechanical structure. Three generations of the HTP platform are developed. The 1st and 2nd generation booms with simple structures use C-channel as the key component. While developing these booms, the stress, deformation, and vibration, are assessed with the finite element analysis (FEA). Meanwhile, it is necessary to understand the actual vibration pattern of these relatively long cantilever beams when attached to moving vehicles; however, previous research have little or limited investigation on vibrations influence on long booms in a farm setting. Thus, part of this research investigates how different factors, such as vehicle selection, vehicle speed, sensor locations, and road conditions, influence the boom attached to a farm machine, its vibration, and its effects on sensors performance for phenotyping. Then, an ideal operating conditions for HTP were obtained. The measurements from sensors confirm that the proposed mechanical structures and their ideal operating conditions are fulfilling the requirements for accurate sensor measurements. Finally, the 3rd generation boom/robotic arm featured of a hybrid structure is proposed and analyzed for its

kinematics and dynamics suitability. Through the calculation and simulation, it shows that this robotic arm meets the requirements, including long-reach and high-payload capability, while maintaining a lightweight and relatively compact size after folding. Moreover, comparing results from path planning routines between Newton-Euler iterative method and simulations, it illustrates that they correlate well.

In this study, I contribute mainly in development of two general-purpose phenotyping booms, evaluate their performance through stress, deformation, and vibration analyses, and compare results obtained through analytical and experimental methods. Besides, factors influencing vibrations of booms in farm fields are analyzed for improving quantity and quality of data collections. Also, my contribution is on development of the 3rd generation boom (a 5-DOF robotic arm) for crop monitoring and its analysis for kinematics and dynamics performance through numerical and hand calculation. As a result, this research generates 2 papers about vibrations and mechanical structure of HTP platforms.

Acknowledgements

I would like to express my sincere gratitude to my supervisor Prof. Reza Fotouhi and my advisory committee members, Prof. Chris Zhang and Dr. Reza Moazed, for the support and guidance throughout my graduate study.

I would also like to thank Natural Sciences and Engineering Research Council of Canada (NSERC) for funding this research through The Global Institute for Food Security - Plant Phenotyping and Imaging Research Centre (GIFS-P^{2}IRC) and Cargill Canada Ltd. for providing equipment, test field, and support for performing tests.

I also appreciate the help from Douglas Bitner, Mechanical Engineering department of University of Saskatchewan to performing and collecting data for vibration tests. The help from Katy Navabi and Amber Sawchuk are also appreciated. Robotics Lab members, including Mostafa Bayati, Majid Khak Pour, Farzam Ayatizadeh Tafti, Joshua Cote, Keegan Wegner, and Danny Wu also provided many supports. I am sincerely grateful for all the help received throughout my research.

Finally, I want to thank my parents for supporting my study and providing consistent guidance throughout my growth without which I could not go this far.

Table of Contents

List of Tables

List of Figures

List of Abbreviations

Listed below are the symbols and abbreviations used most frequently in the text. Occasionally, the same symbol may have a different meaning defined in the text.

D-H	Denavit–Hartenberg
DOF	Degree of Freedom
FEA	Finite Element Analysis
FOV	Field of View
GIFS	Global Institute for Food Security
HTP	High Throughput Phenotyping
LiDAR	Light Detection and Ranging
NDVI	Normalized Difference Vegetation Index
NSERC	Natural Sciences and Engineering Research Council of Canada
P^2IRC	Plant Phenotyping and Imaging Research Centre
UAV	Unmanned Aerial Vehicle
UGV	Unmanned Ground-based Vehicle

Chapter 1 Introduction

1.1 Background

In 2017, more than one in ten people were suffering from the insufficient intake of food and nutrient, and this number has been increasing in the past few years [1]. In fact, the situation may get worse by the end of this century, when the estimated world population is reaching 11.2 billion [1] [2]. To feed such huge population, it is essential to increase the quantity of food supplies and the quality of food; however, the land, equipment, and natural resources for growing crops are limited. One potential solution to rising crop yield with limited resources is through improving breeding techniques such as genotyping and phenotyping [3]. Since the phenotype of a plant directly reflects features such as photosynthesis efficiency and accumulated biomass, choosing a crop with the correct phenotype implies potentially higher yield. Furthermore, for a crop, its genotype and growing environment influence its phenotype, so measuring and assessing the physical characteristics of crops is important for selecting crops with preferred genotype.

In recent years, the development of genetic approaches in molecular level advances the breeding techniques significantly as breeders cultivate a variety of genotypes in a short time. To test different genotypes, breeders need to grow crops in large scale and analyze their phenotypes; however, measuring physical properties such as height and temperature manually is labor-intensive and time-consuming. Thus, traditional phenotyping methods become a bottleneck for contemporary plant science research and crop breeding, so HTP (High Throughput Phenotyping) is required [4].

HTP significantly reduces the data collection time in large fields while generating high accuracy data by quantifying physical properties and avoiding human induced error. Actually, performing HTP successfully can potentially improve the selection of crops with strong genotypes for use in breeding [5]. So far, many researches have been conducted to replace human with HTP platforms using machines and electronic sensors [6]. The two major categories of HTP platforms, aerial and ground-based platforms, use different sensors to measure crop traits, such as height and color. As a result, implementing HTP platforms increase the accuracy, amount of data, and efficiency while reduces cost outstandingly.

1.2 Motivation

To fully describe the crop growth, phenotyping collects large amounts of data from plants describing their physical appearances, such as height, temperature, physical appearance, and greenness. Since each feature may require several sensors for measurements and sensors can have very different operating requirements, it requires a stable platform to implement these sensors simultaneously. This platform should reduce vibrations and have proper mounting locations such that it meets all sensors' requirements.

Even though a few companies and researchers have developed some HTP platforms, they have several shortcomings [6, 7]. First, existing HTP platforms with phenotyping sensors have limited access to the field. UAVs (Unmanned Aerial Vehicles) are typically restrained by its battery. The ordinary fly time of battery powered UAVs designed for small payloads are between few minutes to less than an hour, and extra attachments can significantly reduce the fly duration. They can carry for a wide range of light weight sensors, especially cameras, but they are unsuitable for heavy or sensitive instruments, such as LiDAR (Light Detection and Ranging) or fluorescence camera. On the other hand, ground-based vehicles are preferable for carrying more sensors and collecting large amount of high-accuracy data. These platforms work continuously for hours, but it is typically slower and the size of vehicles or attached booms also limits the range of measurements. Second, most HTP platforms carrying phenotyping equipment are not fully automatic; instead, they require lots of human assistance. In fact, sensors are typically fixed to the mobile device rather than using adjustable actuators. Even though some flexible devices adapt to small leaf plants such as lettuce, they are inappropriate for tall crops, including wheat or canola [8]. They can barely accommodate the large height or reach change during various stages during crop growth. Meanwhile, since many crops grow very fast during their maturity, platforms normally require frequent adjustment to have good measurements. However, for those involve human adjustments, it is not only time consuming and labor intensive, but also influences the measurement accuracy. Third, these HTP platforms lack commonality. Although farmers and breeders grow different crops, they are measuring similar physical properties. Current HTP platforms are typically designed to be attached to the specific type of vehicles or developed as an unrepeatable system such that a platform developed for wheat can be barely applied to measure canola growth, though both systems measure similar features. Finally, many

HTP platforms use commercial platforms or vehicles, but only a few HTP platforms are fully commercialized by now [9, 10]. Some devices like BoniRob are commercially available, however, most platforms are still in the research stage. Particularly, no platforms have been developed for canola or similar crops when canola itself contributes roughly C$26.7 billion annually to Canadian economy [11]. There is a strong demand for HTP for monitoring and breeding canola. Hence, a new ground-based platform performing HTP is required, especially, for canola.

The new platform developed is expected to solve these existing problems and have several improvements. Majorly, instead of manual height/length adjustment, the boom should perform it automatically when phenotyping in canola, wheat, or others. This device should have enough payload capacity for common phenotyping sensors. Besides, it should provide enough height and distance adjustments to each individual sensor if required to ensure the accuracy of range and quality measurements.

1.3 Literature Review

HTP platforms can be categorized into three types, including aerial-based, ground-based stationary, and ground-based vehicles. Aerial based systems are very fast and efficient for various measurements. UAVs use a wide variety of sensors, including digital cameras, thermal infrared sensors, hyperspectral cameras, multispectral cameras and LiDAR systems. They have easy access to fields, high data resolution and volume, fast speed of evaluation the field, and low operation cost, but they also have disadvantages such as high initial costs, low platform reliability, limited sensor capability [7, 12, 13].

Comparing to aerial based platforms, Ground-based platforms typically have a higher data resolution with lower cost, and they have better access to individual crop for measurement or 3D (Three Dimensional) modeling. There are two categories of ground-based HTP platforms, including stationary system and ground-based vehicles. Stationary systems normally have high accuracy and long working duration, but with limited mobility. For example, Xiao et al. proposed a robotic system for monitoring leaf plant breeding [8]. This system with a 3-DOFs (Degrees of Freedom) screening robotic arm was fixed at a counter and monitors the leaf plant from desired angles. Besides, Researchers used similar concepts on large objects up to 1 m,

where they applied a 6 DOF robotic arm to construct high-resolution 3D geometry and color texture images [14]. Other than leaves, HTP is also developed for root growth [15, 16, 17]. Stationary platforms also include system that the major structure is fixed while some components can move. Shanghai Jiao Tong University proposed a high throughput screening robot for rice breeding [18]. This robot used a truss system to support the manipulator module and controlled its motion through direct current servo motors. Even though most of these systems were developed for the indoor purpose, some were applied to outdoor use. For example, Virlet et al. applied a gantry-crane based system developed by LemnaTec to monitor crops, mainly wheat, with high resolution images [19, 20].

Several HTP research works have been conducted using platforms developed in the category of ground-based vehicles to measure physical properties of plants. The ground-based platforms can be subdivided into two categories, namely human involved vehicles and UGVs (Unmanned Ground-based Vehicles). Many human involved vehicles take advantage of existing farming equipment and have a lower cost. Baker et al. constructed a phenotyping platform using a high-clearance tractor as the carrier for the boom allowed it to maneuver easily in the field [21, 22]. At the front of this platform, it had two booms holding 4 sets of sensors, majorly ultrasound transducers and green seekers, to collect data from cotton. Meanwhile, UGVs require minimum human assistance while they have a more complex system and higher cost than conventional platforms. Some UGVs have been applied to phenotyping small plants. Cooperating with Robert Bosch and Amazonen-Werke, Ruckelshausen developed BoniRob, an automated field robot, to screen individual plant [23]. Burud et al. monitored spring wheat using the light-weight Thorvald I agriculture platform which had a low gravity center [24]. Meanwhile, several researchers constructed automated UGV based HTP platform for phenotyping tall plants. One research focused on the sorghum crops designed a phenotyping robot that could travel between crops to perform multiple measurements without damaging the crops [25]. This robot had two major parts including trailer and sensor boom that reached different heights through a vertical mast. Fermandez et al. designed another platform for similar crop measurements. This phenotyping robot was progressed from a tractor with auto-steering capability [26]. In this platform, an extension rig controlled the height of two stereo cameras taking pictures from different angles for 3D image reconstruction. In both robots, they adjusted the height through vertical linear actuators. UGV based HTP platforms were also applied to other crops, such as grapes.

Kicherer et al. applied PHENObot to monitor the growth of grapes using a multi-camera-system [27]. This automated HTP platform took pictures of grapes at a specific height with a linear actuator system to analyze their physical properties including size and color.

The issue with these platforms is that most platforms either attach sensors directly to the vehicles or only use short booms, but few uses only booms and there is limited research to investigate vibration characteristic of booms that carry imaging equipment. Some researchers studied the vibration of a high-clearance phenotyping platform [28]. However, no research has been conducted vibration analysis on a long boom in the field for the crop phenotyping purpose. Besides, most of these HTP platforms were fixed to specific locations at the vehicle, they have less adaptability. The platform designed for wheat may not work for another tall crop. Furthermore, sensors were normally constrained to view crops either from the top or the side, there is a need to increase the flexibility of end effectors.

Employing robotic arms to HTP platform is a potential solution, where it can significantly enhance the reach and the control of FOV (Field of View) of sensors. Ideally, this combined system provides more access to crops in farm fields such that more crops are reached at the same location, and the same crop can be monitored from different view angle though phenotyping. This should increase the quality and quantity of collected data during crop growth. Since the increasing amount of data of crops provides breeders/farmers a better understanding of the field, it would also help understanding of the relationship between genotypes and phenotypes for them.

Previously, robotic arms have been applied to numerous applications, such as industrial and medical. Many works were performed to develop robotic arms with different configurations, to study their kinematics and dynamics, or to perform path planning. Among developed robotic arms, they are typically classified into the serial manipulator, parallel manipulator, and a combination of both. Serial and parallel manipulators with simple structures have been systematically studied in the past several decades. For example, Urrea designed and proposed control for a 6-DOF SCARA manipulator [29]. However, serial manipulators have limitations on payload, while parallel kinematics machines have complex structures making them hard to control. In many situations, a hybrid robotic arm which takes advantages from both types of arms is a better solution, so many research works have been conducted to design hybrid systems and

to study their performance. For example, Tao proposed a simple robotic arm and studied kinematics and workspace of a 4-DOF hybrid palletizing robot [30]. Also, Gherman developed a 5 DOF hybrid parallel robot for surgical application and constructed an inverse dynamic model of the robotic arm [31].

Combining robotic arms with UAVs can increase accessibility to the field during phenotyping, but only a few studies were conducted recently. Sueller-Sim et al. proposed a mobile robotic platform, including a 2-DOF robotic arm to monitor the crops like sorghum or corn with side-facing stereo cameras [32]. Shafiekhani et al. considered a new robotic architecture using two robots which were Vinoculer and Vinobot [33]. Vinoculer was a mobile observation tower using a telescopic arm that inspected the entire field, and the other UGV robot with a robotic arm collected data for individual plants through multiple lightweight sensors. With the combination of these robots, researchers increased the measuring range substantially. However, these arms still either were incapable of moving sensors to the side of the vehicle or had inadequate reach or payload of multiple sensors. To perform the plant phenotyping from a longer distance in large fields, a novel robotic arm is required.

1.4 Statement of Problem

The primary problem is lacking a proper HTP platform to perform phenotyping for densely cultivated crops including canola and spring wheat. To be more specific, an appropriate mechanical structure, a boom/robotic arm, of HTP platform which can carry sensors and reduce ground induced vibration is desired for phenotyping (data collection) on a rough farm field. This established boom/robotic arm shall function on two types of fields, namely the canola field and wheat field. Demonstrated in Figure 1.1, canola grown in breeding fields were in rows and spaced by 2 m unpaved paths for farm vehicles to travel. The total number of 252 plots were divided into 3 rows such that each row had 84 plots that each one had desired genotype in the first two years, and the entire phenotyping plot number was increased to over 2800 in 2018. Plots, which are 6 m long by 1.8 m wide each, are spaced by 0.2 m wide winter canola growing in between. The existence of winter canola space breeding canola and protects them from lodging, so it is important to avoid damaging them. Meanwhile, wheat fields had similar plot orientation where each plot is about 3.6 m long by 1.2 m wide with 0.3 m spacing in between.

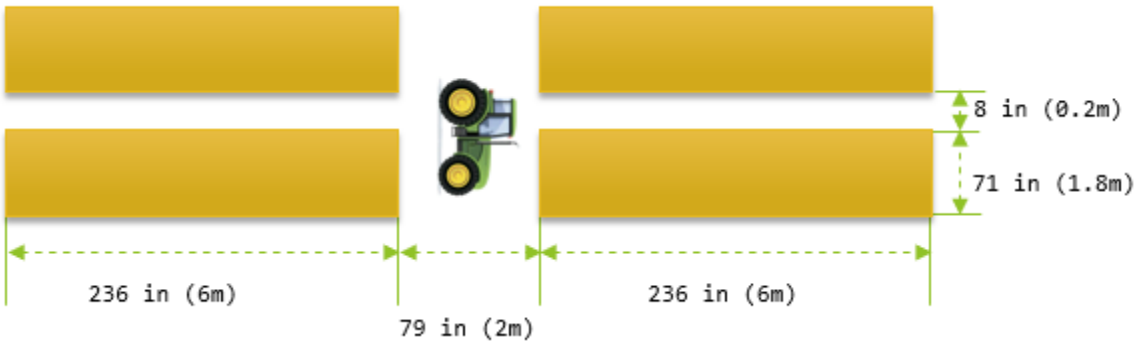

Figure 1.1: Schematic of Test Field

A novel solution is required for developing a generalized mechanical structure attached to available or potential vehicles when it meets all requirements for selected sensors.

1.5 Objectives and Methodology

The objective of this research is to develop a new mechanical platform having enough capacity to support selected sensors for plant phenotyping purpose. There are three major components in this research,

1) Determine whether it is possible to develop a transportable boom with universal mounting features so that it can be attached to various platforms/vehicles.
2) Using vibration analysis to understand how farm fields generated vibrations influence the developed system, including vehicle, boom, and sensors.
3) Investigate if it is necessary to develop a robotic arm, particularly for crop phenotyping. If so, it is important to understand the performance, which can be verified using kinematics, dynamics, and path planning analyses.

To acquire a robust platform, the process of developing this platform involved 3 stages of different booms, including 1st generation non-foldable boom, 2nd generation foldable boom, and a 3rd generation 5 DOFs (degree of freedom) robotic arm. The functionality of each boom was analyzed theoretically during the design and development stage. For 1st and 2nd generation booms, the theoretical analyses include loading capacity, stress analysis, static displacement, and vibration analysis. The analytical and simulation results achieved through software including SolidWorks, ANSYS, MATLAB, and Excel, and were compared to ensure the accuracy of these analyses. Furthermore, the vibration features experimentally tested in the farming fields were

analyzed using FFT (Fast Fourier Transform), and results were compared with theoretical values. In addition, since the 3rd generation robotic arm had a complex structure, it required kinematics analysis and dynamics analysis. The analytical solution for dynamic analysis was obtained through the Newton-Euler approach, while the simulation of inverse dynamics was numerically solved though Simscape toolbox in MATLAB Simulink. The physical properties used in these two approaches were obtained from a preliminary robotic arm model constructed in SolidWorks. The difference between the two models was obtained by comparing the trajectory of the end effector and actuating forces required at each joint.

1.6 Outline of the Thesis

This thesis has 5 chapters altogether. Chapter 1 introduces the development and categories of HTP and HTP platforms. This chapter also discusses the shortcoming of current systems and the specific issues with canola and wheat phenotyping which lead to the motivation of this research.

Chapter 2 covers the design and analysis of developing mechanical structure of three phenotyping platforms sequentially and reveals some test results from 1st and 2nd generation boom.

The vibration tests performed on 1st and 2nd generation booms in farm field are described in Chapter 3. The chapter also compared test results with theoretical values and showed the performance of developed booms.

Chapter 4 investigates the kinematics and dynamics of 3rd generation boom, a 5 DOF robotic arm. To find the proper actuators, a preliminary design was constructed to obtain physical properties that are applied to both analytical solution and simulations. These results from analytical and simulation methods were compared and discussed in this section.

Finally, Chapter 5 summarizes the main contribution and concludes the thesis.

Chapter 2 Design of Booms and Robotic Arm and Novelties

As discussed in Chapter 1, plant phenotyping is important for crop selection to solve food and nutrient insufficient problems, where traditional methods require intensive labors. The potential solution, high throughput phenotyping platforms, helps measuring physical properties of plants in large scale. By investigating the collected data, it can benefit the understanding of relationships between genotypes and phenotypes. However, there are some shortcomings of existing platforms as almost no phenotyping platform has been developed specifically for canola.

This chapter discusses the development of the mechanical structure of a novel ground-based phenotyping mobile platform, which was completed in three generations. The platform was initially designed for a densely cultivated canola; it was gradually improved for a more general purpose to measure other crops, such as wheat and lentil. The concepts, components, functionalities, and performance of these platforms are covered in the following sections. Besides, it explains the theoretical analysis and simulations for developing the mechanical structure of these booms, and FEA (Finite Element Analysis) was used in simulation part, which includes stress, deformation, and vibration analysis.

2.1 Background

The primary goal was to develop a HTP platform carrying various sensors for crop phenotyping purpose in several stages as described previously. The final version of the developed HTP platform is a general platform performs phenotyping for a variety of plants, but the primary targets include canola and wheat. For canola breeding field, located in Aberdeen, Canada, the surface texture is clay loam such that the soil stays packed in dry condition. This feature creates a rough surface condition of the unpaved field shown in Figure 2.1. It is estimated that the average of valley-to-peak distance is about 5 to 10 cm, and the average peak-to-peak distance is roughly 15 cm. Consequently, vibration introduced by traveling vehicles in this field condition can significantly influence the accuracy of measurement from designated sensors, especially digital cameras for taking photos and sensors for measuring heights. In the initial crop phenotyping stages, the chosen breeding field has a total of 252 plots equally divided into 3 rows where 2 pathways had a 2.4 m (8 feet) wide path permitting the access of farming vehicles. Each plot is a section of land approximately 1.8 m wide by 6 m long, and two adjacent plots are

spaced by a 0.3 m (1 foot) wide winter canola. Ideally, continuously monitoring and measuring each crop is required from seeding to maturity when a fully-grown canola canopy can be as tall as 1.4 m. In the meantime, the other breeding field of wheat in Kernen farm near Saskatoon has a similar orientation, where each plot is 3.8 m (12.5 feet) long by 1.2 m (4 feet) wide, and there is a 1.8 m (6 feet) path in between 2 adjacent rows for the farm vehicle passage. A fully-grown wheat is lower than a canola, and the average height is around 1.2 m. The size and height of booms were designed according to this information.

Figure 2.1: Surface Condition in Test Farming Field (Aberdeen, SK)

There are three generations of the platform where each one has three major components, including vehicles, mechatronic devices, and booms. It is essential to select an available vehicle with the correct size and loading capacity. Besides, the vehicles with features of cruise control, hydraulic system, and vibration reduction will smooth data collection. Three types of vehicles were selected, including a high-clearance swather (Zürn Model 550), a 4ft-tractor (Massey Ferguson Model 1523), and a 6ft-tractor (Massey Ferguson Model 1529). The 2 m wide swather shown in Figure 2.2 has a clearance up to 1.6 m with a 50 kW engine. The 1.07 m wide 4ft-tractor weights 594 kg with a 16.8-kW engine, and the other 1.47 m 6ft-tractor is 1169 kg with 21.2 kW power. All these vehicles had hydraulic systems and cruise control features. The high-clearance swather is equipped with a hydraulic system to lift connected equipment. Meanwhile, 4ft and 6ft tractors are using 3-point hitch for quick connection to other tools and lifting attachments through hydraulics. These tractors are not only commonly available for the farming/breeding purpose, but also stable and affordable. Potentially, they can support the

developed HTP platform for large-scale purpose. The other important element of this HTP platform is mechatronic devices. To correctly and accurately measure physical properties of each plot, transducers in HTP platform should measure several traits, including appearance, height, temperature, and greenness; therefore, several sensors are considered, including high resolution cameras (Canon D70 and Web camera Logitech Pro: C920 and C615), ultrasound sensors (Honeywell 943), infrared thermometers (Apogee SI-131), and NDVI sensors (Holland ACS-430). Moreover, these sensors are connected to a laptop via a data logger to collect and save data. They are placed in the overhead position to collect data that describes the crop growth. Since each sensor has its working range and a preferred measuring distance, it requires a bridging component to connect these sensors and vehicles while adjusting physical heights between them. This crucial piece is a boom that provides physical support, height adjustment, small vibration, and transportability.

Figure 2.2: Zürn 550 Swather Used in Canola Field for Monitoring Crops

Based on the background information, there are some general design requirements to be considered through the boom developing process. To be more specific, these constrains for the platform are listed as following,

1) To develop a boom with universal mounting features that can be attached to various platforms/vehicles.
2) The boom should have various mounting locations for selected sensors including cameras, thermometers, NDVI (Normalized Difference Vegetation Index) sensors, ultrasonic sensors, etc.

3) The boom should be adjustable in height such that it can monitor different types of crops including canola, wheat, lentil, etc. from seeding to maturity.
4) The boom should reach desired locations to allow sensors measuring each plot completely.
5) The boom should have small vibrations during operation to ensure the proper function of selected sensors.
6) The boom should be transportable without being taken apart.

These design requirements were considered through the design of several booms/robotic arms for phenotyping. Initialed with the simplest structure, the boom is improved gradually until a multi-purpose robotic arm. Details of these booms are covered in the following sections.

2.2 The First-Generation Boom

The 1st generation platform is developed according to the minimum requirements for crop phenotyping. This platform has a simple mechanical structure to support a wide variety of sensors for measuring canola's physical properties in a breeding farm.

2.2.1 Mechanical Structure of the First-Generation Boom

The major requirements for this platform include holding sensors in desired range and height, introducing minimum vibration to sensors from the farm field, working properly in a rough field environment, and being user-friendly during both assembling and operations. To fulfill these requirements, the developed platform has following features, such as height adjustable structure, active or passive vibration control through the rigid structure, and minimum number of components.

To be more specific, first, the measurements from boom should cover the whole plot. Since each plot is 6 m long and can be accessed from both ends, to reduce the complexity and weight of the structure, a 3 m long arm on one side is sufficient to cover the whole plot when measured once from each end; However, most sensors measure a range of canopies, so reducing the length of the boom to 2 m can still have same performance and avoid duplicating trait measurements for the center part of a plot. Meanwhile, collecting data from both plots on the left and right sides of the vehicle simultaneously increases the plant phenotyping efficiency. Considering the width of

the path which is 2 m, the total length of the boom is 6 m long. For height adjustment, it is achieved through three parts, namely, swather, rear tool holder, and mechanical structure of the boom. Both heights of swather and rear tool holder are adjusted though equipped hydraulics, which provides roughly 1 m change when combined. Nevertheless, it is insufficient for monitoring the whole growing stage of canola. Hence, the boom is designed with a mounting plate allowing the sensors to be placed at a lower or a higher position. Second, some sensors require small vibration to give accurate measurements. Equipment such as cameras and ultrasound sensors are sensitive to height changes, so 6 inches high C-channel is introduced to minimize the structure deflection in the boom due to vibration. It should also be noticed that C-channel has a much larger section moment of inertia about its shorter edge, so using C-channel allows fewer height changes when vibrates along the long axis. This can be seen in the Chapter 3, vibration test. Third, rough farming field conditions require a durable boom. In farming fields, the boom is suffered from the uneven surface, dust, and rain. Several methods are utilized to reduce the influence from critical surroundings including, painting or galvanizing to prevent corrosion, bolt connections to increase reliability, and altering gravity center to improve stability. Finally, simple structure reduces labor requirements of assembling and disassembling of the boom, while allowing multiple sensor attachments during operations. Since, the swather also performs other types of work, especially, during the harvest season, the developed boom should be easy to assemble/disassemble without specific knowledge or abundant instruction.

As shown in Figure 2.3, components of the 1st generation platform include a C-channel boom, a connection plate for C-channel, turnbuckles and other pieces. The main section of the platform is a 6 m long C-channel beam that is attached to a mounting plate through 4 bolts to either the lower or upper position. The mounting plate has 4 connection locations for four pins which connect the lower part of the mounting plate to the rear tool holder of the swather and attach the upper part of it to 2 turnbuckles. Meanwhile, the other end of the turnbuckles is connected to a bar that is secured to the swather through lock pins and support plates. As a result, the tool holder, boom mounting plate, and turnbuckles formed a trapezoid that controls the direction of sensors. Since changing the length of hydraulics in the rear tool holder and swather influences the heights of the tool holder and the boom, this also affects the orientation of the sensors. To ensure that sensors are perpendicular to the ground, length of turnbuckles is adjusted to compensate the angle change.

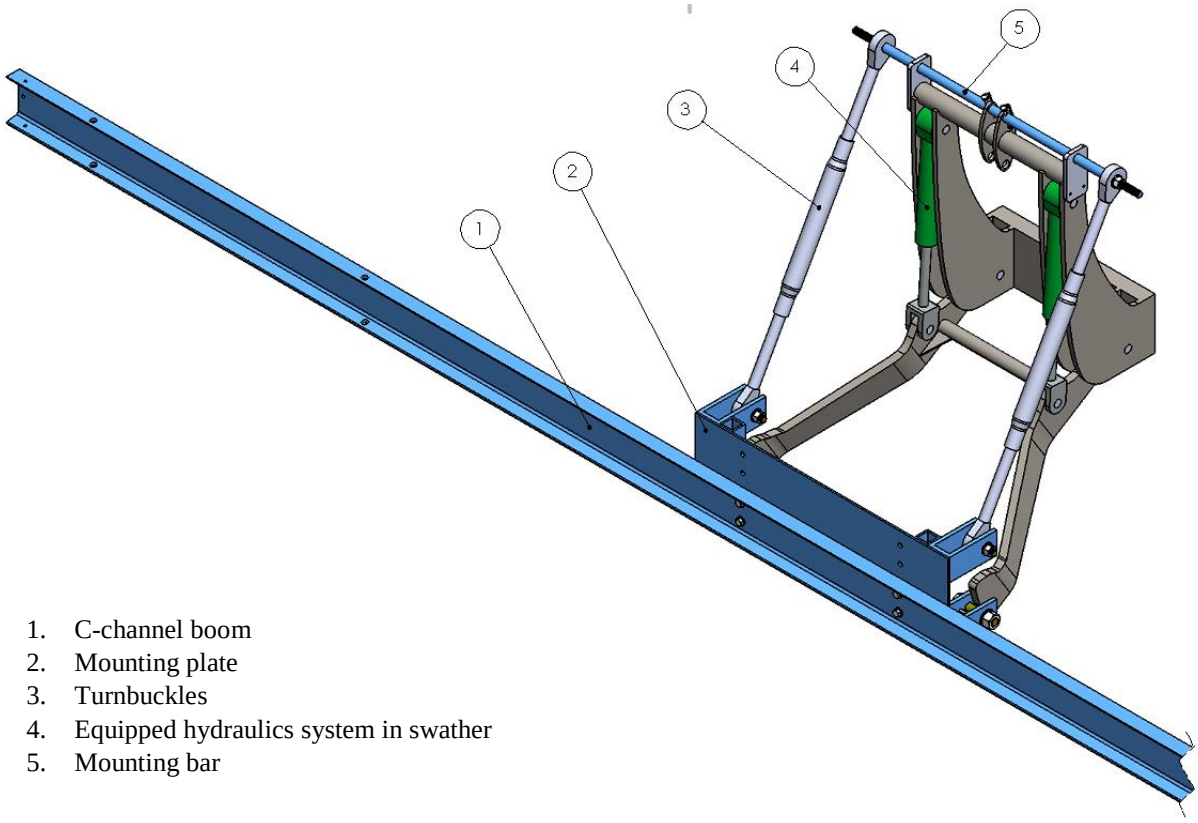

1. C-channel boom
2. Mounting plate
3. Turnbuckles
4. Equipped hydraulics system in swather
5. Mounting bar

Figure 2.3: Assembly of Developed 1st generation Boom

The mechanical structure of the 1st generation boom allows easy assembling, quick adjustment, and low manufacturing costs. First, components and bolt connection design facilitate the platform assembly process. After attaching pings to the mounting plate, operators lift the plate and set it to the jaw of the rear tool holder. Then, they can connect turnbuckles to the mounting bar and the plate before attaching the C-channel boom. The whole operation is straightforward. Besides, operators could mount selected sensors including ultrasound sensors and cameras via pre-drilled holes on the boom with minimum efforts. During assembling and disassembling tests, it took less than one hour for four people to accomplish this task. Second, the whole platform provided enough height and angle adjustment for phenotyping. The major height adjustment came from three sources, namely connection plate, rear tool holder, and swather chassis. The design of the connection plate gives extra height adjustability for the boom, which is about 12 inches, and the rear tool holder is adjustable for 23 inches. Finally, simple structure and connections reduced the operation and maintenance cost.

2.2.2 FEA of the First-Generation Boom

During the development, FEA is used to understand the performance of the 1st generation boom. Analyses, including stress and deformation, are performed in ANSYS workbench. Based on the actual measurements of the swather and design dimensions of the 1st generation boom, a model involves the tool holder and boom is generated in the 3D modeling software, SolidWorks, and transferred into FEA software later for analysis. Several assumptions are made in stress analysis of this model. First, connections between components are fixed. Since the trapezoid formed by the tool holder and the boom is stable when hydraulics keeps one of the inner angles fixed, this assumption is valid. Besides, it assumes that both hydraulic cylinders and turnbuckles assembly are rigid and act as one piece. It is observed that both components have barely any internal movements during operation, so the deflection is negligible. Additionally, the material for all components are assumed to be AISI 1020 steel. Even though the applied material for C-channel is A36 when manufactured, both materials have similar mechanical properties. Since the heat treatment and other factors can influence the mechanical properties, AISI 1020 that is well understood is more appropriate to start the analysis. Meanwhile, labeled in Figure 2.4, the applied forces include gravitational acceleration (A), 50 N load applied to each end of the boom due to weights of sensors (B & C), and fixed support at the end of the swather's tool holder (D). Finally, the whole structure is meshed with tetrahydro elements in FEA where results are demonstrated in Figure 2.5.

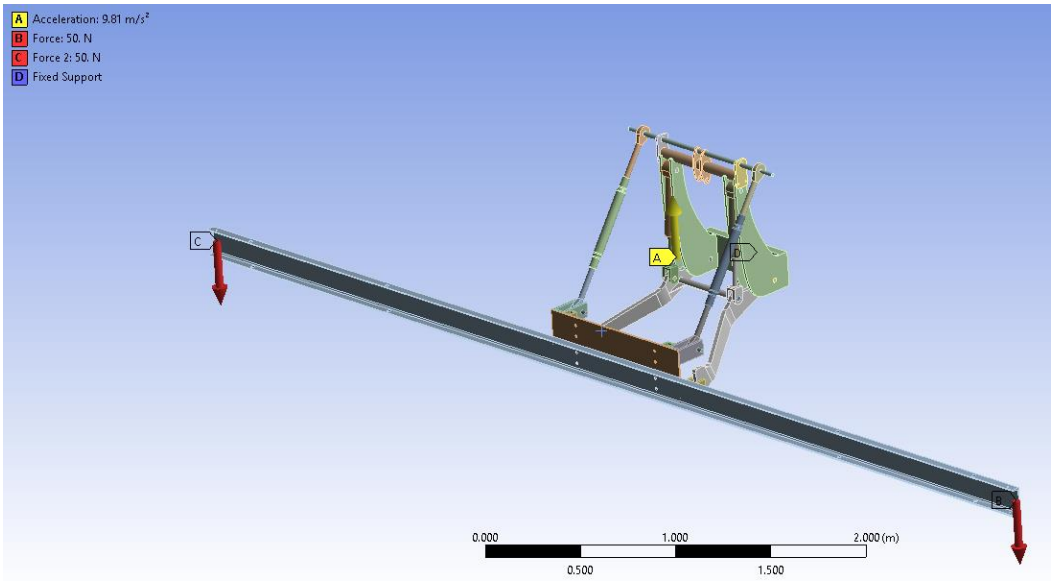

Figure 2.4: Boundary Conditions in FEA Analysis of 1st Generation Boom

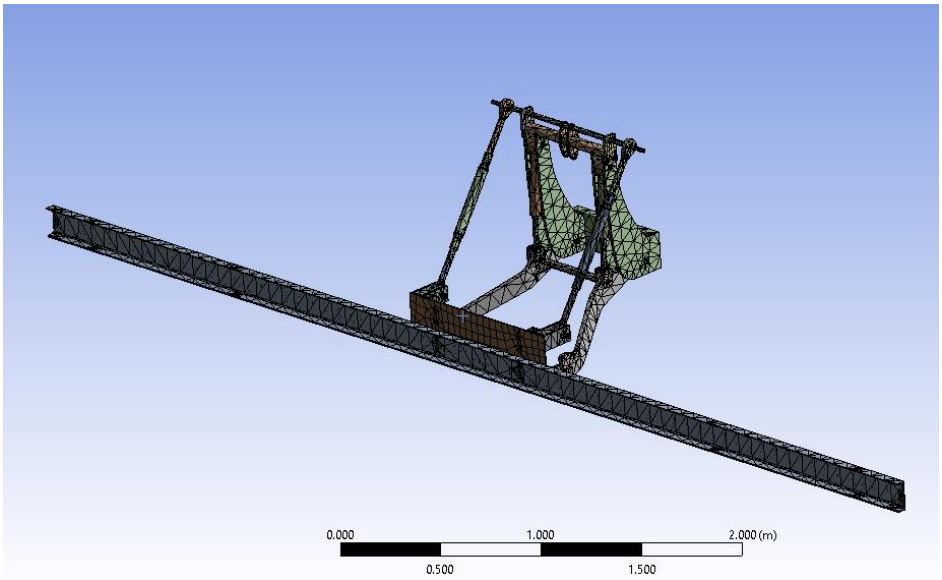

Figure 2.5: Meshed Body in FEA Analysis of 1st Generation Boom

Since the deflection and vibration are more important than stress, a strong structural material is applied to reduce the deflection during vibration. The 6 inches C-channel ensures the maximum stress is well below the ultimate tensile stress. Displayed in Figure 2.6, the boom has a maximum deflection at the boom tip, and it is about 1 mm in the static case. The overall stress distribution along the structure is below the yield stress when the maximum stress is found at the top section where the supporting bar locates.

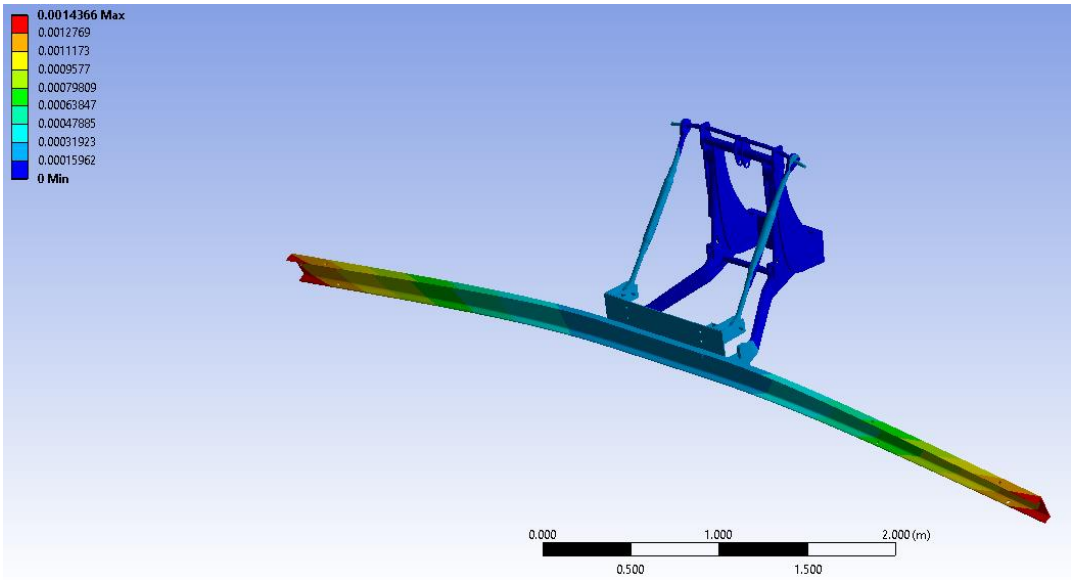

Figure 2.6: Deflection in FEA Analysis of 1st Generation Boom

2.2.3 Performance

The developed boom was manufactured, assembled, and tested in the field to assess its performance. The primary experiment was to investigate its vibration characteristics, where a few tests were performed on the boom to find its natural frequencies and vibration amplitude during regular phenotyping process. The details and results of vibration tests performed are covered in Chapter 3. Meanwhile, the fully assembled 1st generation HTP platform with all sensors attached (Figure 2.7) completed several data collections through the canola growth in 2016, 2017, and 2018. After analyzing the collected data, it indicated that the quality of measurements met initial requirements from breeders.

Figure 2.7: 1st Generation Boom Assembled with Sensors

The content in taken photos reveals the distance is well maintained between cameras and the crops, and picture quality indicates the boom's vibration has limited influences to designated cameras. For example, Figure 2.8 and Figure 2.9 show photos of crops in different stages from a DSLR camera and a web camera. These figures clearly display the canola growth in those stages.

Figure 2.8: Photos of Canola at Maturity Stage from DSLR Camera Mounted on the 2nd Generation Boom on Swather with 1.6 mph

Figure 2.9: Photos of Canola at Flowering Stage from Webcam on the 2nd Generation Boom on Swather with 1.6 mph

Another way to evaluate the developed 1st generation boom is through the crop height measurements by comparing the crop height measurements from ultrasound sensors to manually obtained values. The ultrasound sensors measured the distance between the top of the crop and the boom. By subtracting this value from the boom's height, the crop height is calculated. Meanwhile, the manual measurements come the average height measurement of three selected crops in each plot using a meter stick. Figure 2.10 demonstrates this difference for 30 canola growing plots measured on July 30, 2017. It confirms a good correlation between automated and manual measured height when the average difference is about 3.6%. This satisfies breeders' expectations. It should be noticed that measured crop heights from sensors are influenced by the boom's vibration and the tilt of the vehicle, so there are some systematic errors. The major error from tilt can potentially be solved by implementing two ultrasound sensors to measure the height difference and calculate the tilting angle. Then, the height measurements can be corrected. Besides, adding active vibration control can also solve this problem.

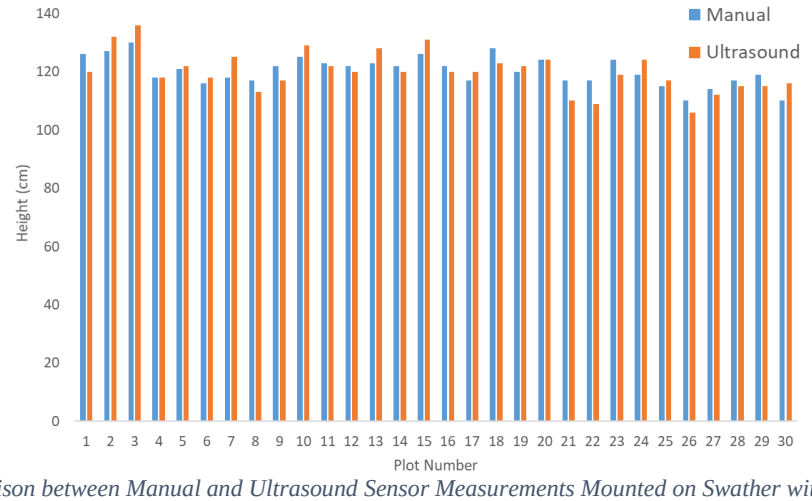

Figure 2.10: Comparison between Manual and Ultrasound Sensor Measurements Mounted on Swather with 1.6 mph on July 18, 2017

2.3 The Second-Generation Platform

Based on the analysis and performance of the 1st generation boom, a 2nd generation platform was developed with a similar structure; however, the structure was redesigned to implement features like highway transportability, multiple vehicle adaptability, and multiple sensor adjustability.

2.3.1 Mechanical Structure of the Second-Generation Boom

The 2nd generation boom has a similar structure to the 1st generation boom, but it uses a smaller size structural material. This boom also has two types of adapters (type A and B) to fit on different vehicles, swathers, and tractors. Models of this platform are demonstrated in Figure 2.11 and Figure 2.12, where Figure 2.11 shows the 2nd generation platform (type A) designed for high-clearance swather and the other one using the type B platform for tractors equipped with 3-point hitch category 1 connection (ASAE S217.12 standard) is shown in Figure 2.13. Type A platform is specially designed for the same swather carrying the 1st generation boom; however, since most farming tractors have 3 point-hitch connection, type B platform is a more universal platform intended for attaching and detaching operations.

The 2nd generation platform involves several improvements majorly in reducing the weight, adding folding mechanism, providing more sensors attaching locations, and increasing transportability. First, to reduce the weight and facilitate installation, the 2nd generation boom is divided into 3 sections, involving a centerpiece and two end sections that are made from 5 by 6.2 C-channel using steel. Since the weight of each section is about 1/3 of the previous boom, it requires less operators to assemble the boom. In the actual test, two operators can assemble/disassemble the boom quickly for both types of booms. Besides, the size of other components like turnbuckles are also reduced to have a lighter structure while minimizing the compromise of performance. The performance of this boom is analyzed through FEA and field tests as that for the 1st generation and is described in the following sections.

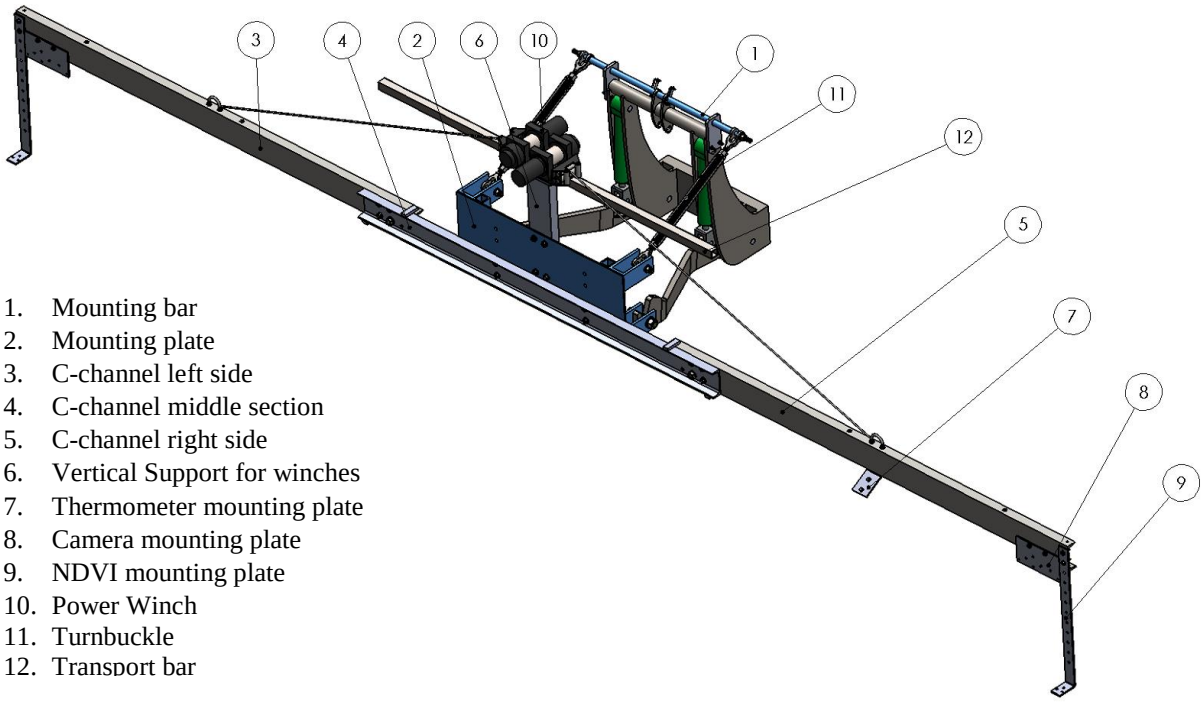

1. Mounting bar
2. Mounting plate
3. C-channel left side
4. C-channel middle section
5. C-channel right side
6. Vertical Support for winches
7. Thermometer mounting plate
8. Camera mounting plate
9. NDVI mounting plate
10. Power Winch
11. Turnbuckle
12. Transport bar

Figure 2.11: Assembly of Developed 2nd Generation Boom (Type A)

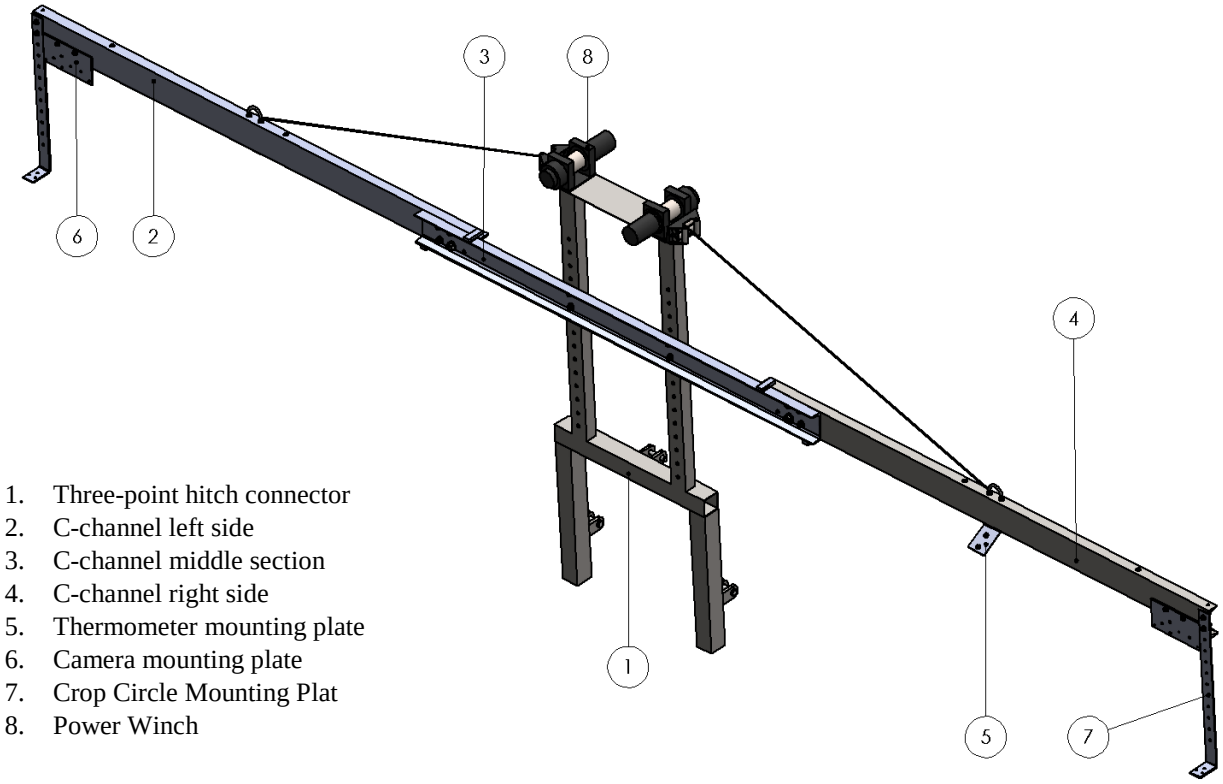

1. Three-point hitch connector
2. C-channel left side
3. C-channel middle section
4. C-channel right side
5. Thermometer mounting plate
6. Camera mounting plate
7. Crop Circle Mounting Plat
8. Power Winch

Figure 2.12: Assembly of Developed 2nd Generation Boom (Type B)

Figure 2.13: 3-Point Hitch Connection between 2nd Generation Boom (Type B) and Tractor

The second improvement is enhancing transportability by implementing folding operations through winches. The expanded booms shown in Figure 2.11 and Figure 2.12 are the configurations when performing data collection, and Figure 2.14 demonstrates the orientation of the boom during transportation. In the folding process, four connection bolts on each side, except the large bolt acting as a rotary pin, are removed to allow the movement of the left/right end section shown in Figure 2.15. Then, electric powered winches pull the cable to lift the end sections from horizontal to vertical position. Finally, bolts are placed back into the same location on the end section to secure the boom during transportation. To facilitate folding operations, two blocks on each side, including one piece welded to the top of the C-channel middle section and the other one welded to the bottom, restrain the rotation of the left/right side of the boom to 90 degrees. In the data collection configuration (expanded), two stoppers hold the end pieces in position when bolts are removed before the folding operation to reduce labor requirements and risk of injury. During the folding process, the upper pieces stop rotating end section after reaching the vertical position and allow workers to insert and tight bolts. In this case, it also reduces operating risk and manpower.

Figure 2.14: Assembly of Developed 2nd Generation Boom in Folded Configuration

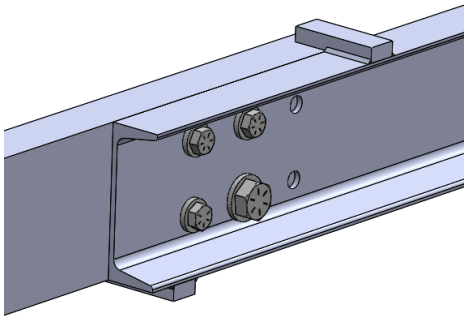

Figure 2.15: Connection between Center Piece and End Piece of the Boom

Another enhancement is improving boom adjustability for sensors through redesigned turnbuckles, connection components, and crop circle mounting plate. The turnbuckles are redesigned to lighter weight pieces with more adjustability such that they can cover the whole moving range specified by the rare tool holder on the swather. Besides, the 2nd generation boom has a new piece for crop circle adjustment. Most sensors are height independent, and cameras with adjustable lens are less sensitive to height changes. However, crop circles are different as the angle of view of the crop circle is fixed. Since its FOV is determined by the distance from the crop, adjacent plots influence the reading when this sensor is placed too far from the plot. To address this issue, a crop circle mounting plate which has 10 holes spaced by 2 inches (5cm) is implemented into the boom system. Figure 2.16 exhibits the structure of this component and bolt connection among this piece, the boom, and crop circle. Besides, cameras and thermometers are designed with special mounting plates to secure them and facilitate their movements. Furthermore, for type B boom, it uses an H-shape connection piece (component 8 in Figure 2.12) having multiple holes spaced by 2.4 inches (6 cm) on it. It provides 31.2 inches (0.8 m) adjustment to the boom and sensors from 28.2 inches (0.71 m) to 59.4 inches (1.5m). When

considering the height adjustment from tractors, the adjustable height range is roughly from 0.75m to 1.8m. This is enough for wheat phenotyping, and it can potentially be applied to other crops, including lentils and fava beans.

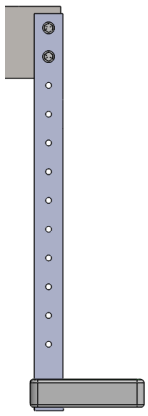

Figure 2.16: The Assembly of Crop Circle and Mounting Plate

2.3.2 FEA for the Second-Generation Boom

The stress and deformation analysis are performed on the 2nd generation booms with FEA. As the process for the 1st generation boom analyses, a model of the boom is built in the 3D modeling software and transferred into FEA software for analysis. Same assumptions are made in the stress analysis, including fixed connections between components, rigid hydraulic cylinder and turnbuckles assembly, and AISI 1020 steel as the major material. Meanwhile, labeled in Figure 2.17, boundary conditions for FEA include fixed support at 4 pin connection located at the mounting plate (A), 50 N load applied to each end of the boom due to gravitational force from sensors (B & C), 300 N vertically from the winch (D), and gravitational acceleration (E). Finally, the whole structure is meshed with tetra-hydro elements majorly in FEA where results are demonstrated in Figure 2.18. The stress and deformation of the 2nd generation booms are calculated numerically.

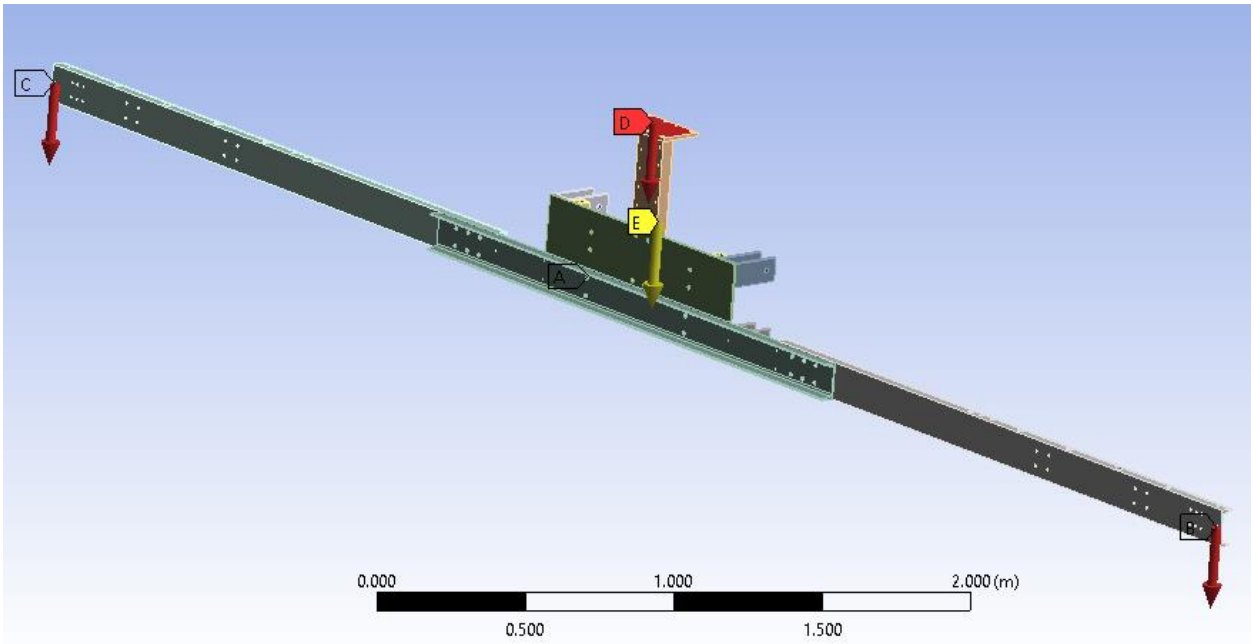

Figure 2.17: Boundary Conditions in FEA Analysis of 1st Generation Boom

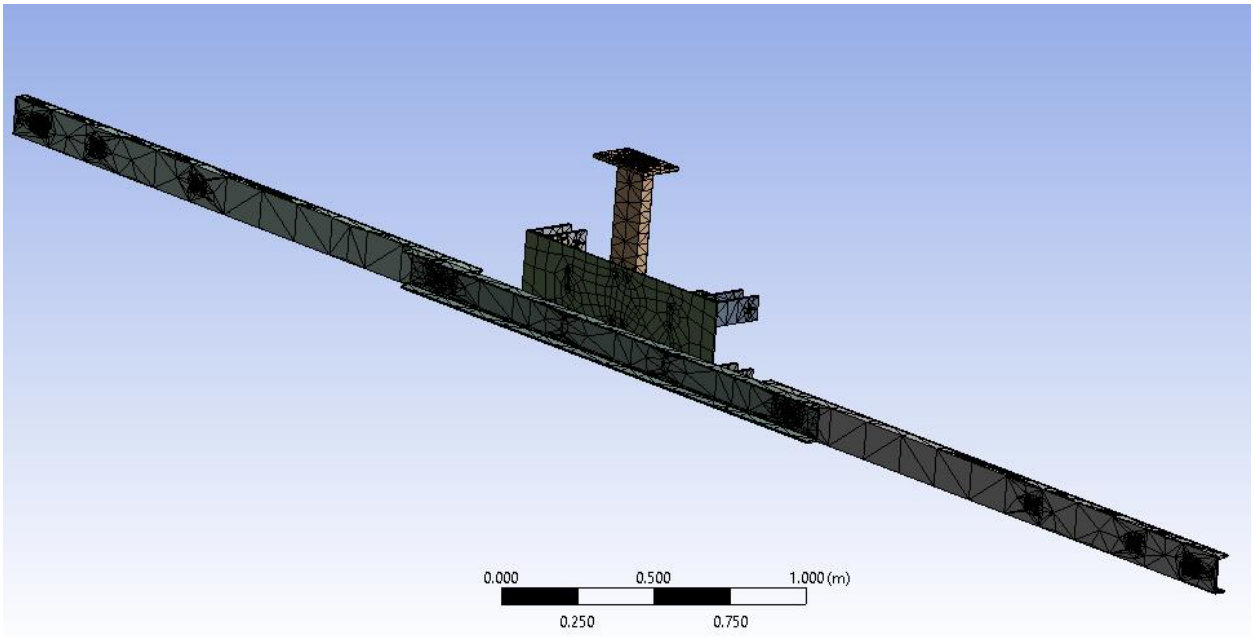

Figure 2.18: Meshed Body in FEA Analysis of 1st Generation Boom

Since the deflection and vibration are more critical than stress, the strong structure material is applied to reduce deflection during vibration. Figure 2.19 shows that the boom has 1.3 mm maximum deflection at the boom tip in the static case. Using the 5 by 6.2 C-channel, the overall stress distribution along the structure is significantly below the yield stress where the maximum stress is 11.2 MPa.

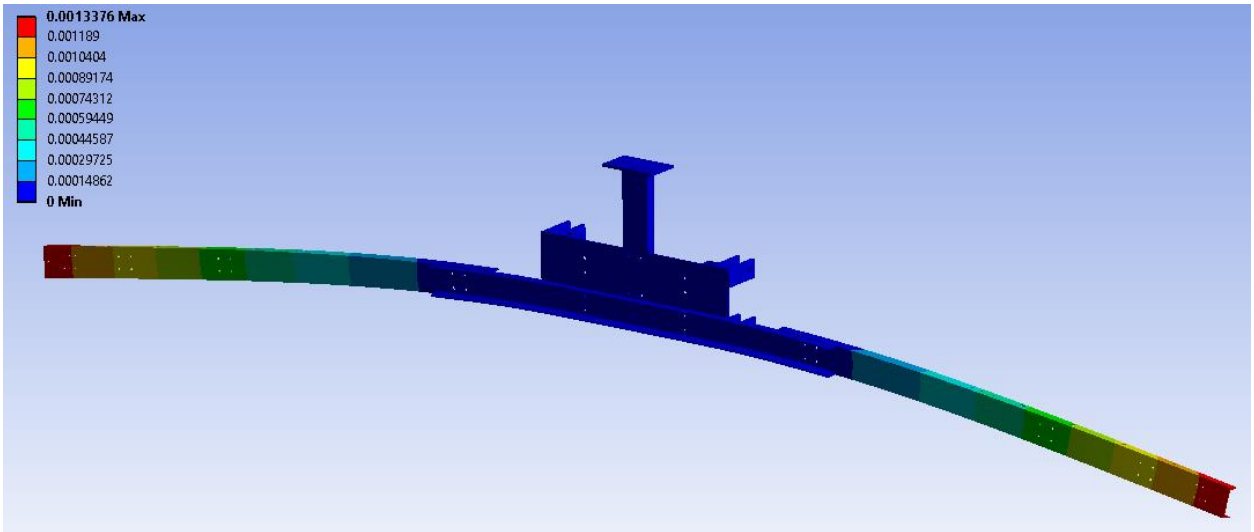

Figure 2.19: Deflection in FEA Analysis of 2nd Generation Boom

2.3.3 Folding Analysis

To design a proper folding mechanism, it is necessary to analyze the strength of each cable such that it does not break during lifting operation, and the maximum pulling power of electrical winches should also be verified. To calculate the stress during lifting, a few assumptions are made to simplify the calculation. First, since a winch winds its cable at very low speed, it is assumed that the whole boom is statically balanced at each moment during the lifting. Second, only half of the boom is analyzed due to symmetry. Third, the center of the boom is assumed to be fixed. Forth, the center of each winch is lined up with the center of end sections, so the boom is simplified to 2-dimensional geometry.

Figure 2.20 shows the free body diagram of the boom and winch system where point A refers to the location that sensors are attached to; point B refers to where the cable is anchored to; point C is the joint between two sections of the boom; and, point D is the center of the boom. When taking sum of the moment about point C of section AC, there is

$$G_b \cdot S_1 + F_{app} \cdot d_2 - (T \cdot sin\alpha) \cdot d_{mount} - (T \cdot \cos\alpha) \cdot h_2 = 0 \qquad (2.1)$$

Where G_b, the weight of the boom, is 25 kg;

G_{app}, the total equivalent weight of all sensors, is 5 kg;

T, the tension load inside the cable,

d_2, the horizontal displacement from attached sensors to joint C;

h, the vertical displacement from winch location to the center of the boom;

d_{mount}, the horizontal distance from cable anchor point B to joint C;

h_2, the vertical distance from cable anchor point B to joint C;

α, the angle between cable and horizontal location is between 0 to 90 degrees.

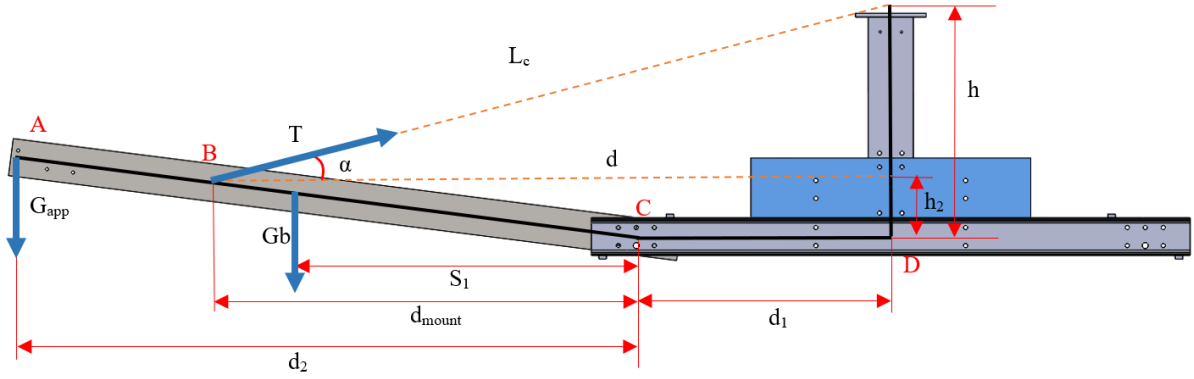

Figure 2.20: Free Body Diagram of the Boom for the Tension Load in the Cable

When the boom is rotating from horizontal to the vertical direction (0 to 90°), different height of the vertical section generates different loading patent in the cable. Various heights are selected to compare loading inside the cable, where results are plotted in Figure 2.21. It shows that the maximum tension appears at 0° angle when the boom is horizontal for all cases; and, the maximum stresses when the cross-section of the cable is assumed to be uniform is decreasing with respect to increasing length of the vertical component. Since there are physical constrains of the length of the vertical part such as the height limitation in transportation regulations, the total weight of the boom, and considerations for installation and maintenance, 0.5m (20 inches) height is selected when the tension in the cable is 1548 N (348 Lb.). On the other side, a wide range of commercial power winches or hoists can handle this load. It should be noticed that major power winches use a 12 V battery as a power source when the power consumption and generated heat are positively related to the applied load. To safely complete the pulling process, a proper safety factor should be considered.

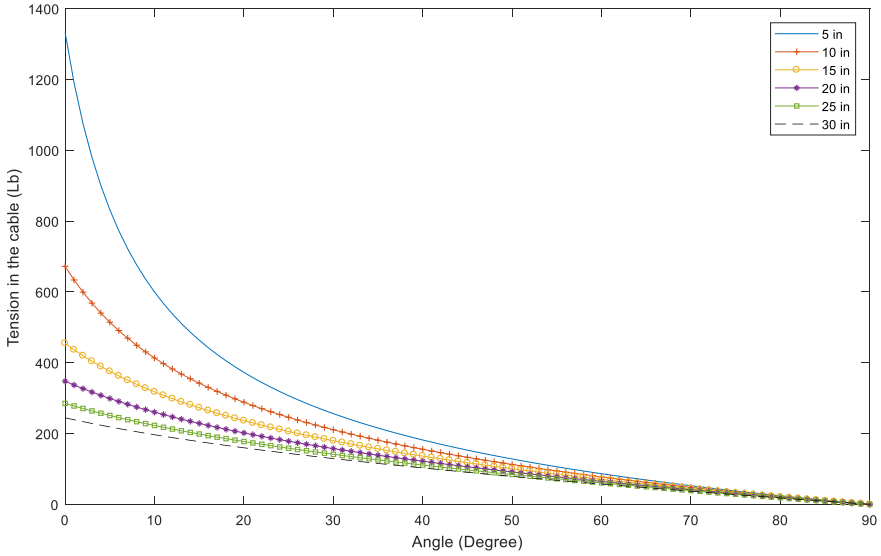

Figure 2.21: Change of Tension Load in the Cable from 0 to 90° at Different Winch Height

The selected winch is a commercial winch designed for pulling vehicles, so it is necessary to determine its actual pulling capacity. The product indicates that it has 3500 Lb. pulling capacity of a rolling vehicle but did not specify the lifting capability. A test was performed with a universal testing machine shown in Figure 2.22. In this test, the winch is anchored at the bottom of the pulling machine and the cable is attached to the pulling section. Then, the machine and the winch both started to pull the winch cable while the pulling load is recorded by the load cell is displayed on the computer next to the machine. The tension measured is gradually increased from roughly 0 to the maximum of 1759 Lb. Even though the test result is smaller than 3500 Lb., it is enough to lift the boom during the folding procedure.

Figure 2.22: Universal Testing Machine for Pulling Capacity Tests

2.3.4 Performance

The 2nd generation boom was assembled and tested in the farm fields. Figure 2.23 shows the type A boom attached to the swather for canola measurements, and Figure 2.24 shows type B boom for wheat measurements. When fully assembled, the folding test was performed on the actual boom as well and it takes about 10 seconds to lift either side. More importantly, the measurements from different sensors have similar accuracy and quality to those from the 1st generation boom, and they also satisfy the breeders' requirements.

Figure 2.23: 2nd Generation Boom Mounted on a Swather (Type A in folded, and expanded boom positions)

Figure 2.24: 2nd Generation Boom Mounted on a 6ft-Tractor (Type B) in Wheat Field

However, there are several limitations of the 2nd generation boom. First, it doesn't have any active vibration control, except the passive structural damping only. This limits vibration reduction to certain frequency range, and the platform has limited adaptability to low frequencies vibrations when the ground is rough. The boom can barely compensate the height change due to the unleveled ground. Second, the height of the boom requires manual adjustment before each run. It is time-consuming to change the boom height and facing angle so that sensors are at the best height. On average, it takes approximately 15 minutes to adjust the boom, and it requires another 20 minutes to calibrate all four ultrasound sensors. Third, the distance between the sensors and the boom changes during operation. The recently developed software for controlling sensors does not allow zoom in/out for DSLR cameras or webcam and sensors like green seekers cannot zooming in/out; however, crops with different genotype may have different height. The changing distance between crops and sensors due to vibration during operation can result in inaccurate measurements and blur pictures. It requires some mechanism to adjust the height of the boom through the operation. Thus, a more advanced boom is proposed in order to solve these issues.

2.4 The Third-Generation Platform

The 1st and 2nd generation booms require lots of human involvements and have limited automation. To automatically monitor a large breeding farm with thousands of plots, a smarter and more advanced platform is required. Hence, a 3rd generation, fully automated platform, involving both an autonomous mobile robot and robotic arm(s), is proposed. This section focusses on the development of the mechanical structure of this robotic arm, and Chapter 4 covers the analysis of this arm.

Comparing to previous booms, the 3rd generation boom has further design requirements for mobility and payload considerations. First, the 3rd generation robotic arm should have more flexibility which will potentially allow the arm to implement active vibration control that can significantly reduce the vibration amplitude. The robotic arm should also reach different locations at the required height to meet data collection requirements from seeding to maturity and give a full description of the crop growth. Essentially, the arm should at least have a 2.5 m maximum reach from the center of the base to the end-effector and have an adjustable height between 0.5 m to 2 m at such distance, so it can cover the 6 m long breeding field as the 1st and

2nd generation booms. Second, it should have a payload of 10 kg at the 2.5 m location to carry existing and potential sensors. Since the end effector includes multiple sensors, such as digital cameras, ultrasound sensors, thermometers, and LiDAR, currently the total weight of these sensors are around 6 kg. The 10 kg payload not only meets the requirements of existing sensors, but also leaves additional capacity for additional equipment to be considered, such as multi-spectrum cameras and hyper-spectrum cameras. Third, this arm should have a total weight of less than 100 kg for maintenance and transportation purpose. The potential vehicles for carrying the robotic(s), including UGV Grizzly, are powered by batteries, so a lightweight design will increase the data collection duration and extend phenotyping coverage. This will also enhance the performance of the robotic arm and allow it to work for a longer duration. Finally, the repeatability of this robotic arm is designed for 5 mm when traveling. The arm is designed for field application, and major sensors, including webcam and ultrasound sensors, are sensitive to location change. Besides, considering the limitations of vehicles GPS which has at least 2 to 3 cm error in its location accuracy, the arm is unnecessary to have ultra-high precision or repeatability.

In the developing stage, configurations of several robotic arm are considered to fulfill design requirements, as shown in Figure 2.25, where R and P refer to Revolution joint and Prismatic joint accordingly. Figure 2.25-a shows an arm with 3 revolute joints which has a simple structure and can reach multiple locations at the required angle, but this arm can be too long to be placed on a small UGV. The other issue is that the arm can reach a certain point in the space with only one configuration, so it is not capable to reach the position if anything blocks its path. Both Figure 2.25-b and 23-c demonstrate robotic arms with 2 revolute joints and 1 prismatic joint when 23-b allows the motion perpendicular to upper arm and 23-c allows the end section to move in that same direction of the upper section. Figure 2.25-d shows a robotic arm with 4 DOFs, so each section is shorter that other 3 arms. However, all these arms are serial manipulators. Putting motors at the joints create several problems. First, a longer link requires a larger torque at the corresponding joint, so a heavier motor, larger power supply, and more complex mechanism are needed for such joints. Second, a motor can introduce imbalance to the system when a motor is located at one side of the robotic arm. Therefore, a parallel arm is proposed with the same number of DOFs shown in Figure 2.26. Unlike serial manipulators that require a motor at each joint, a parallel mechanism has several links connecting to the same

common base such that its motion is influenced by each link. This allows mounting actuators to be placed at a lower position when having same number of DOFs as a serial arm. In general, comparing to the serial robot, parallel arms can carry heavier payloads with higher accuracy.

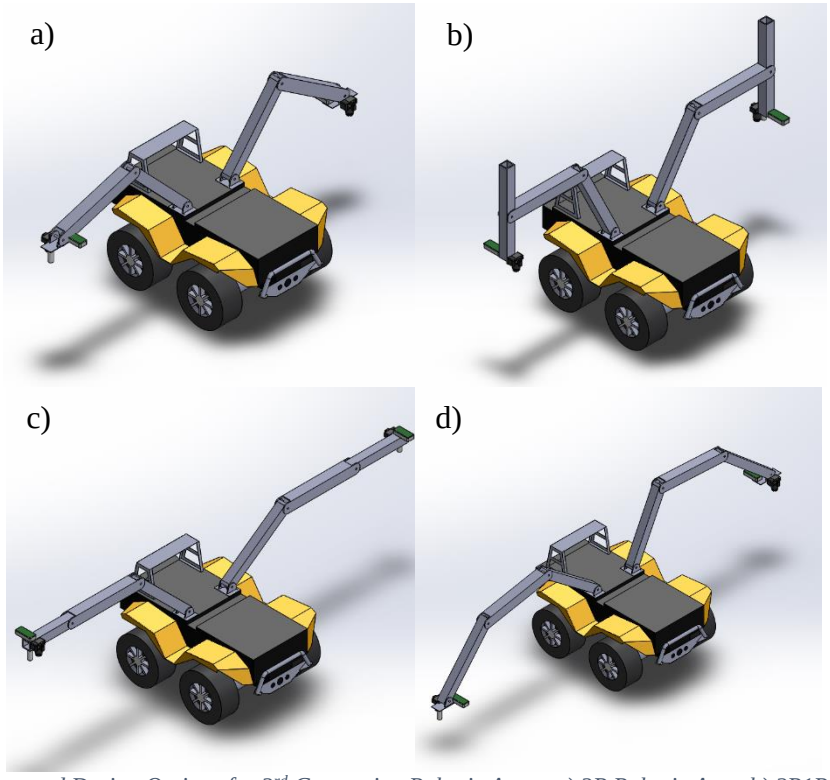

Figure 2.25: Proposed Design Options for 3rd Generation Robotic Arms: a) 3R Robotic Arm; b) 2R1P-1 Robotic Arm; c) 2R1P-2 Robotic Arm; d) 4R Robotic Arm

The proposed robotic arm is a hybrid manipulator with both serial and parallel links. This arm has 5 DOFs including 4 revolute joints and 1 prismatic joint. The arm has 6 major sections which are approximately 1 m long individually, including the base, lower arm, parallel links, upper arm, extension arm, and end effector. The base of this robotic arm allows it to be connected to different UGVs. The upper arm connects to the parallel links through pin connection, so its motion is controlled by the rotation of parallel links. On the other end, the upper arm connects to the extension arm through a linear actuator which transfers rotation to linear motion. The end effector has an L-shape bracket such that different sensors can be attached. Meanwhile, the arm has 5 rotate motors. One of the motors provides the rotation of the base, so it turns the robotic arm when the vehicle while its moving. Two motors with corresponding speed reducers control the motion of the parallel section where one motor controls the motion of the lower arm and the other one manipulates the upper arm rotation through parallel links. Furthermore, a prismatic

joint guarantee that the arm can reach the same location with different orientations to avoid contact with potential obstacles. Finally, a small motor regulates the angle of the end effector such that the field of view of sensors covers the top of an individual plot or they are at the desired orientation.

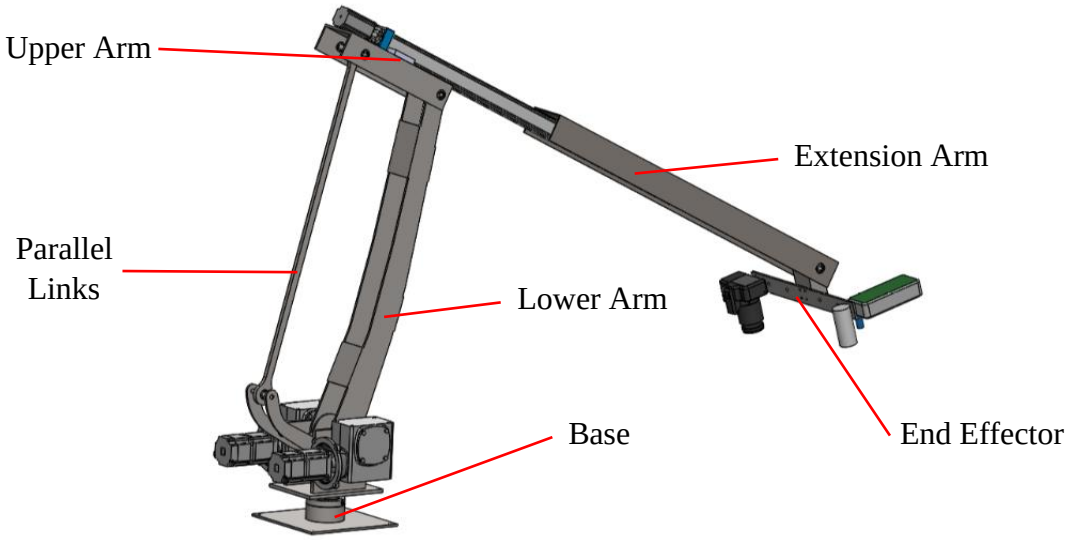

Figure 2.26: The Proposed Structure of the 3rd Generation Robotic Arm for Plant Phenotyping

The 3rd generation boom (a robotic arm) has several advantages. First, the robotic arm has a wide workspace and can be adjusted automatically. Comparing to previous booms, this manipulator can reach different distance and height rather than sampling at four fixed locations during phenotyping. Currently, booms collect data at 1 m and 2 m from the edge of a plot; however, the new arm can gather data at any distance, which offers a better observation and analysis of the field through more data collection locations. This feature also resolves the demand of using mounting plates and adjusting the height of the boom to keep a proper distance between sensors and crops for accurate measurements. Potentially, the arm adjusts its height atomically for each series of plots, the height of which typically various significantly due to different genotype and environment. Second, the flexibility of this arm increases its functionality in a constrained workspace. The total 5 DOF can still reach the desired position if part of the path is blocked by some obstacles. It also extends the working duration by choosing a more efficient path, such as a path with less shift of the gravity center. Third, vibration induced to the sensors can be reduced through active vibration control of the robotic arm. Using encoders and

inertial measurement unit, motors in the arm will compensate the height change due to low-frequency vibrations from the uneven ground. This set up can largely reduce the error in height measurements. Finally, the design can increase the phenotyping speed. Since breeders focus more on the center of a plot, the robotic arm allows the data collection from only desired locations while vehicle is moving at a constant speed without any stop. The end effector of the robotic arm can stay still at the center of each plot for short period of time until all data is collected, and it quickly skip the border between plots to next desired location. In this way, requirements of faster data collection speed and higher data accuracy is met.

2.5 Summary

This chapter discussed the development of three phenotyping booms from the 1st generation boom of a simple structure to the 3rd generation robotic arm with a more advanced mechanism. The 1st and 2nd generation booms were examined for their stress and deformation, and they were tested in the field for measurement accuracy. Through field tests, it proved that these booms are stable, adjustable, and reliable for mounted sensors to collect data from crops.

Chapter 3 Vibration Experiments and Simulation on the 1st and 2nd Generation Booms

Most farm fields in Saskatchewan have uneven surface introducing significant vibration to the farm equipment. Breeders perform negligible surface treatment after seeding, so the path between crops are rough. While operation vehicles in these fields, large vibration displacements have been observed at the boom end during phenotyping. Since data collection process involves high accuracy sensors and sensitive equipment, such as cameras, ultrasound sensors, and LiDAR, to collect a large amount of data, the introduced vibration significantly influenced the reliability of the HTP platform, functionality of sensors, and accuracy of the collected data. It is important to investigate how different factors impact the vibration such that the vibration in sensors can be minimized though optimization mechanical structure. In this way, more accurate data measurements are acquired.

This chapter covers the experiment apparatus, the methodology applied for analysis, process, and test results, of the vibration experiments on the 1st and 2nd generation booms. The significance of the results and potential sources of error are also discussed in this chapter. To understand how vibration affects boom's performance, it is important to discover its vibration characteristics such as the frequency and amplitude; thus, vibration experiments are performed. These tests include two essential components, namely laboratory verifications and field experiments. In laboratory tests, vibration sensors are verified for its capacity and accuracy in a controlled environment. While in field experiments, vibration sensors are placed at selected locations on the boom to measure its acceleration or displacement changes. Then, applying Fast Fourier Transform to these collected data converts results from the time domain to the frequency domain. Finally, the obtained results from different test conditions are compared with simulation results to investigate how different factors, such as vehicle speed and road pavement, influence boom's vibration.

3.1 Vibration Tests in the Laboratory Environment

To ensure the proper function of devices and the reliability of experiment results, it is necessary to find the capability and accuracy of equipment by performing vibration tests in a controlled laboratory environment. In the vibration tests, essential apparatus for data collection

involve vibration transducers, amplifiers, and an oscilloscope. To be more specific, vibration sensors (accelerometers) includes Bruel & Kjar Type 4370 and 4371 transducers that are capable of measuring frequencies from 0.1 Hz to roughly 4.5 kHz and 12 kHz separately. It should be noticed that these are uniaxial sensors that they only measure vibration in one direction, and vibrations in the perpendicular direction have a minor influence on the measurements. Besides, amplifiers, type 2635 from Bruel & Kjar, magnify these sensors' signal to the required level while filtering out both undesired low-frequency and high-frequency signals. A 4-channels oscilloscope manufactured by Keysight displays and stores measurements for further data analysis. In addition, for calibration and verification purpose, vibration tests also involve equipment including a multimeter, a vibration generator, a shake table, etc. Details of laboratory vibration tests are discussed in the following sections.

Acquiring measurements with high accuracy requires sensor calibration before performing any tests. In the calibration test, each transducer was attached to a vibration exciter which generates vibrations (Model Bruel & Kjar Type 4294) at a specific level of $10 m/s^2$ acceleration, 10 mm/s velocity or 10 μm displacement at 159.2 Hz (1000rad/s). Then, the transducer was connected to a multimeter/scope via an amplifier as shown in Figure 3.1. For easy reading, each amplifier was adjusted such that the output from the connected corresponding accelerometer is magnified to 1 V RMS signal as displayed on the multimeter.

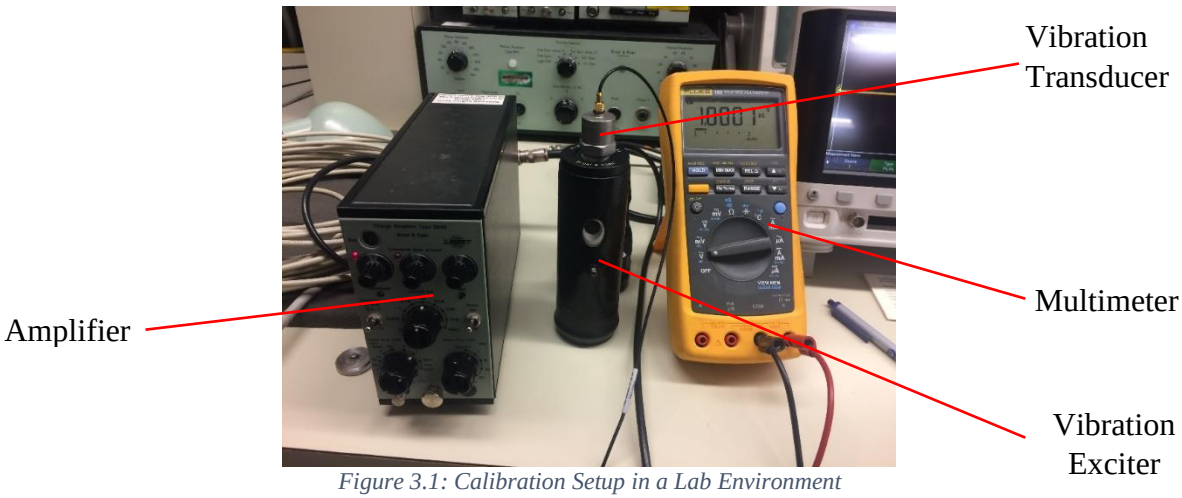

Figure 3.1: Calibration Setup in a Lab Environment

After calibration, it is important to verify that sensor measurements are accurate, so a laboratory set up examined these sensors by measuring vibrations generated from a controlled source with known frequencies. Figure 3.2 demonstrates a schematic diagram, and Figure 3.3

shows the actual set up of the equipment connection in a laboratory environment. In this test, a vibration generator and an amplifier generated a specific signal with a known frequency and displacement for a shaker table. These devices could produce a vibration up to 50 Hz with 0.1 Hz increment. As shown in Figure 3.3, the accelerometer which was attached to the top surface of the shake table measured the table's movement, and the results were displayed on the oscilloscope.

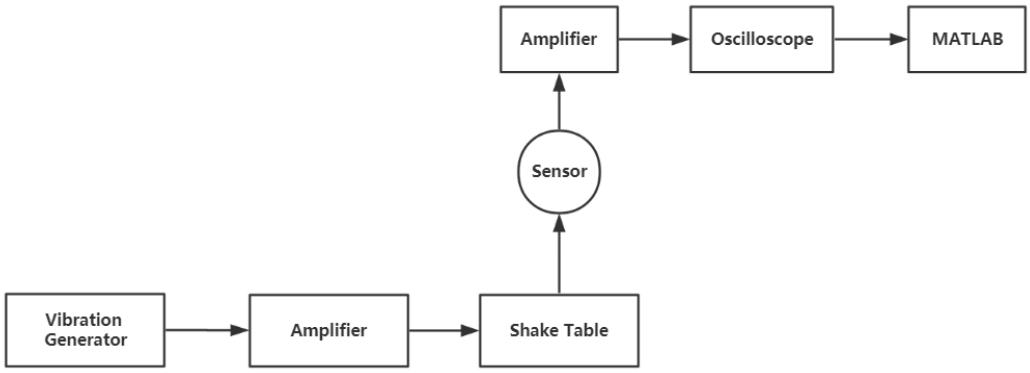

Figure 3.2: Schematic Diagram of Vibration Tests in the Laboratory Environment

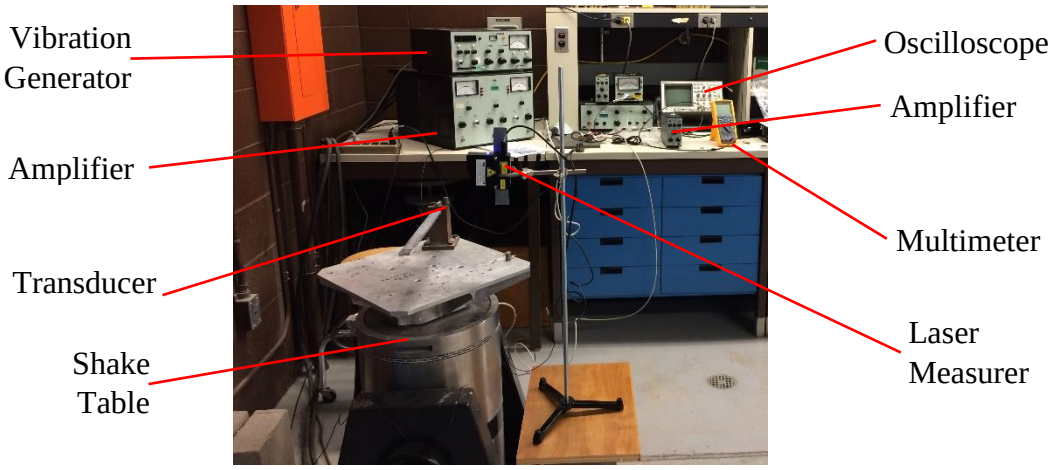

Figure 3.3: Setup of Vibration Test in a Control Lab Setting

Through these devices, the accuracy of sensor measurements was tested both in frequency and amplitude. To verify the accuracy of frequency measurements, vibration generator created vibration at desired frequencies, including 5 Hz, 10 Hz, 30 Hz, etc., where signals appeared on the oscilloscope. For example, Figure 3.4 shows one set of sensor measurements when the input signal was at 5 Hz. Counting peaks in Figure 3.2, it turns that the frequency measured was 5 Hz, which matches the signal's frequency from the vibration source. Meanwhile, displacements were

verified through a laser distance measurement by comparing its value in the oscilloscope reading. Several measurements were taken at various frequencies. Since oscilloscope reading was in voltage, it required a conversion between voltage and displacement. As described in the previous section, the relation is 10 µm for 1 V at 159 Hz. However, demonstrated in Amplifier type 2635 from Bruel & Kjar., the amplifier gain was not constant for displacement measurements at different frequencies as shown in Appendix A: Amplifier type 2635 from Bruel & Kjar. To find the actual voltage gain at a certain frequency, the following equation was used,

$$G_{dB} = 20 \log_{10} \left(\frac{P}{P_0} \right) dB \qquad (3.1)$$

where, P is measured power; P_0 is reference power; and, G_{db} is the ratio expressed in decibel. With this equation, the converted displacement matched the measurements from the laser measurement system. Therefore, the accuracy of the accelerometer measurements was verified by both frequency and amplitude.

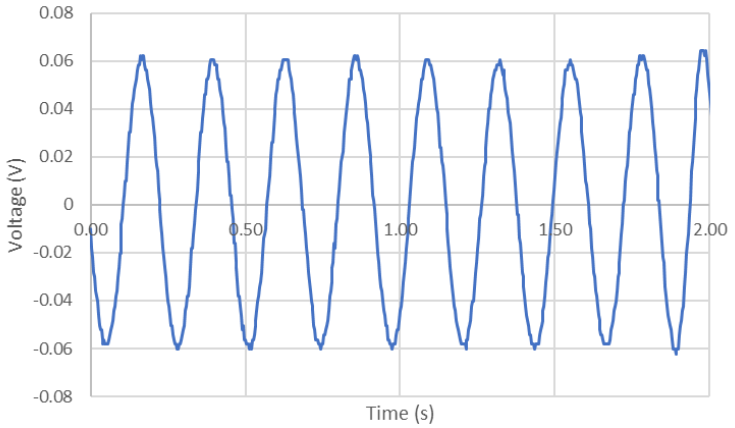

Figure 3.4: Displacement Measurements of 5 Hz and 14 Hz Signal in a Lab Environment

3.2 Vibration Experiments in the Field Environment

Four sets of tests were performed to observe the vibration characteristics of the booms mounted on different vehicles. Two field tests were performed on the 1st generation boom attached to a swather (Zürn 550). The first test measured the acceleration change at different locations on the boom on May 31, 2017, and the second test measured the displacement change on July 25, 2017. The other two tests utilized the same equipment while the amplifier setups were slightly different. For 2nd generation boom, field tests were performed on two different kinds of the tractors namely 4ft tractor (Massey Ferguson Model 1523) and 6ft tractor (Massey Ferguson Model 1529) on Oct 5, 2017. In the experiments, the boom was excited by a hammer

from vertical and horizontal direction separately to measure the natural frequency. Then, sensors were placed at the desired locations on the boom.

3.2.1 Field Experiment Setup

For the 1st generation boom, field tests utilized similar equipment, including accelerometers, amplifiers, an oscilloscope, batteries, and a converter, to measure acceleration or displacement changes. Figure 3.5 illustrates a schematic diagram of equipment connection. In this test, the oscilloscope was powered by a 12V battery via a 12 V to 110 V converter. Listed in Table 3.1 and Table 3.2 are locations (left end, center, and right end) of two sensors, “Sensor 1” and “Sensor 2”, on the boom. Figure 3.6 shows the overall set up of the equipment and Figure3.7 shows vertical and horizontal placement of sensors. Then, each accelerometer transmitted output signals in voltage to a scope through an amplifier (Figure 3.8). Finally, measured data, including time and voltage, was saved to an external flash drive for FFT analysis.

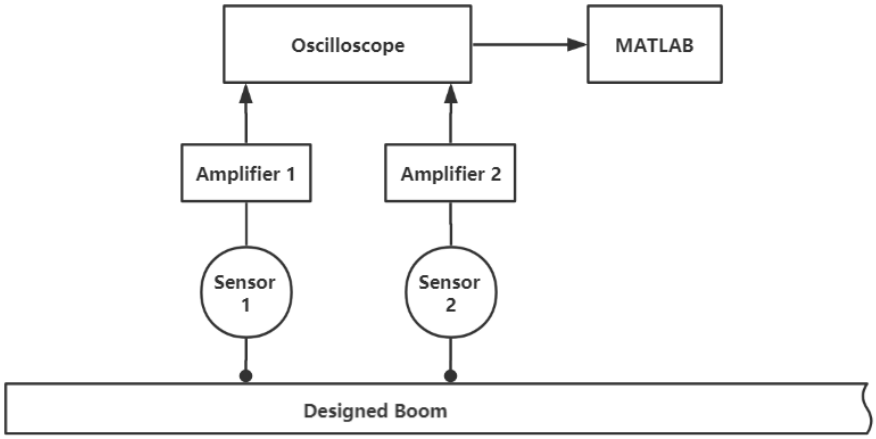

Figure 3.5: Schematic of Vibration Test Equipment for 1st Generation Boom

Figure 3.6: Overall Setup for 1st Generation Boom Field Vibration Experiments

Figure3.7: Sensor Located at the Center (Vertically) and Left End (Horizontally) of the Boom

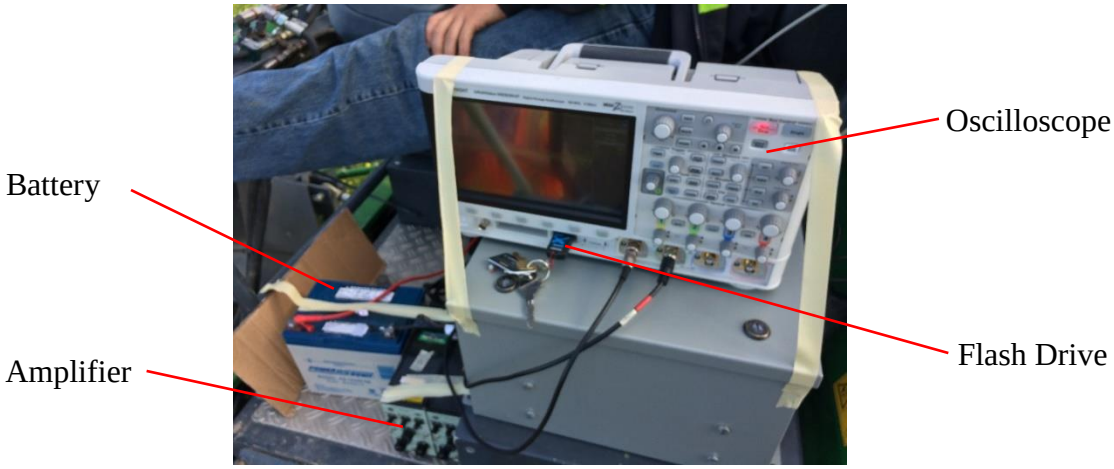

Figure 3.8: Oscilloscope and Amplifiers Applied in the Field Tests

Two sets of experiments performed on the 2nd generation boom with the same equipment as the 1st generation boom except using an additional set of amplifier and accelerometer which was calibrated as discussed in section 3.1. Sensors and amplifiers were marked with three different

color labels, namely Yellow (Y), green (G), and blue (B) accordingly for identification. A schematic diagram of the connections is demonstrated in Figure 3.9. Sensors were placed at different locations during the field tests as shown in

Table 3.3 and Table 3.4. Figure 3.10 and Figure 3.11 exhibits locations and orientations of three sensors during two tests.

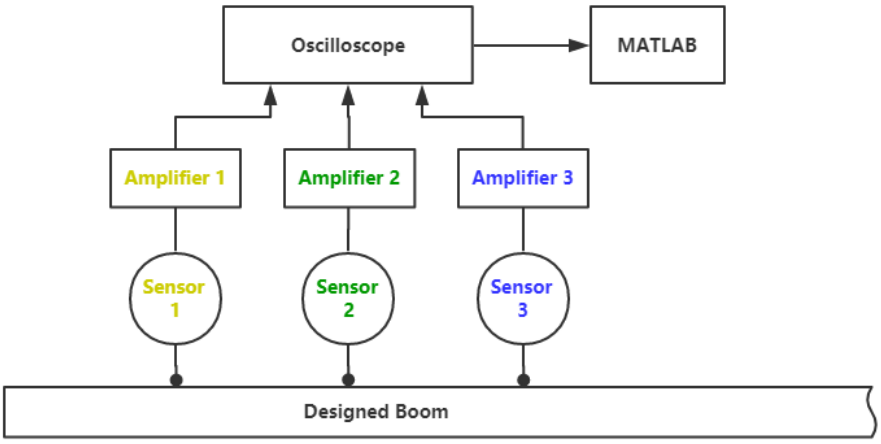

Figure 3.9: Schematic of Vibration Test Equipment for 2nd Generation Boom

Figure 3.10: Sensors Located at Left End of the Boom Vertically

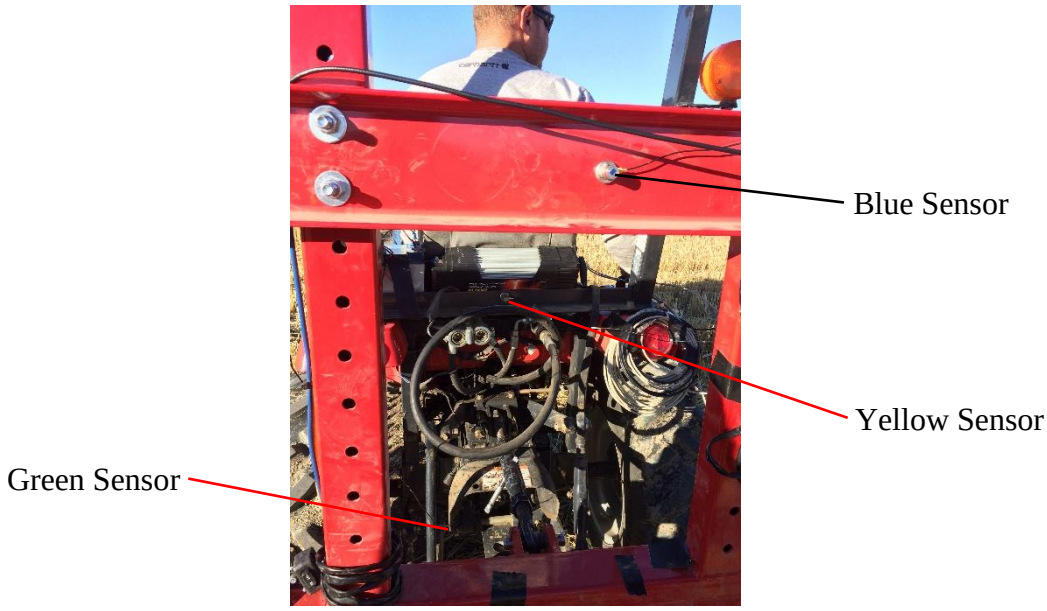

Figure 3.11: Sensor Located at Center of the Boom Tractor, 3-Point Hitch, Tractor Frame Horizontally

3.2.2 Procedure and Parameters for Field Test

Before performing the actual experiments, equipment was connected and tested to ensure vibration transducers could generate the same output when placed at the same location on the boom. For natural frequency measurements, a hammer applied a mild impact to the boom end from vertical and horizontal direction separately to excite vibrations which were then picked up by the attached sensors. The major section of field experiments was performed on moving vehicles. In these experiments, sensors were attached to desired locations, and amplified accelerometer measurements were recorded for a fixed duration while the vehicles were operating at a steady speed. After the data had been collected and saved, swather was stopped to reallocate sensors. Finally, this procedure was repeated until all configurations and locations were tested as planned in Table 3.1 to Table 3.4.

Table 3.1 demonstrates vibration experiments with acceleration measurements performed on May 31, 2017. The data were measured when swather operated at 0.7m/s (1.6 mph). This is the speed of the Swather during phenotyping data collection and capturing pictures. Two sensors were placed at different positions with either vertical or horizontal orientations, and each row in the table indicates one trail. In the position column, boom-center refers to the center of the whole boom; Left/right refer to the left/right end of the boom; tractor-center refers to the center of the swather's chassis. Orientation describes sensors placement vertically or horizontally. The scope

number is corresponding sequential test number and saved file's name. Since most tests are repeated several times for each setup, scope number is a range.

Table 3.1: May 31, 2017 Field Test Performed Using Acceleration Measurements on Swather in Aberdeen

	Sensor 1		Sensor 2		
Trail #	Position	Orientation	Position	Orientation	Scope Saved #
Field Tests					
1	Boom--Center	Vertical	Boom--Left	Vertical	1-5
2	Boom--Center	Horizontal	Boom--Left	Horizontal	6-10
3	Boom--Left	Vertical	Boom--Left	Vertical	11-12
4	Boom--Left	Vertical	Boom--Left	Horizontal	13-17
5	Boom--Right	Vertical	Boom--Left	Vertical	18-22
6	Tractor--Center	Vertical	Boom--Left	Vertical	23-27
7	Tractor--Center	Horizontal	Boom--Left	Horizontal	28-32
Natural Frequency					
8	Boom--Center	Vertical	Boom--Left	Vertical	33-34
9	Boom--Center	Horizontal	Boom--Left End	Horizontal	35-36
Lab Test for	Verification				
10	Lab Test	Vertical			

Table 3.2 shows the measurements on July 25, 2017. Amplifiers were set to displacement mode at 10 Hz to measure the displacement. This table includes extra columns, namely speed and track. Speed shows the actual swather speed while performing these tests, where 1.6 mph (0.7 m/s) is the current swather speed during phenotyping and 4.5 mph (2 m/s) is the potential speed for future phenotyping operations. The boom was also tested on two unpaved roads that are numbered as 1 and 2 in track column with a similar surface roughness.

Table 3.2: July 25, 2017 Field Test Performed Using Displacement Measurements on Swather in Aberdeen

	Sensor 1		Sensor 2				
Trail #	Position	Orientation	Position	Orientation	Speed	Track	Scope Saved #
Natural Frequency- Calibration Test							
1	Boom--Left	Vertical	Boom--Left	Vertical			2
Natural Frequency							
2	Boom--Left	Vertical	Boom--Left	Horizontal			3-4
Field Test - Calibration							
3	Boom--Left	Vertical	Boom--Left	Vertical			5
Field Tests							
4	Boom--Left	Vertical	Boom--Right	Vertical	1.6	1	6
5	Boom--Left	Horizontal	Boom--Right	Horizontal	1.6	1	7
6	Boom--Left	Vertical	Boom--Center	Vertical	1.6	1	8
7	Boom--Left	Horizontal	Boom--Center	Horizontal	1.6	1	9
8	Boom--Left	Vertical	Tractor--Left End	Vertical	1.6	1	10
9	Boom--Left	Horizontal	Tractor--Left End	Horizontal	1.6	1	11
10	Boom--Center	Vertical	Tractor--Left End	Vertical	1.6	1	12
11	Boom--Center	Horizontal	Tractor--Left End	Horizontal	1.6	1	13
12	Boom--Center	Horizontal	Tractor--Left End	Horizontal	4.5	1	14
13	Boom--Center	Vertical	Tractor--Left End	Vertical	4.5	1	15
14	Boom--Left	Vertical	Boom--Right	Vertical	4.5	1	16
15	Boom--Left	Horizontal	Boom--Right	Horizontal	4.5	1	17
16	Boom--Left	Vertical	Boom--Center	Vertical	4.5	1	18
17	Boom--Left	Horizontal	Boom--Center	Horizontal	4.5	1	19
18	Boom--Left	Horizontal	Boom--Center	Horizontal	1.6	2	20
19	Boom--Left	Vertical	Boom--Center	Vertical	1.6	2	21
20	Boom--Left	Vertical	Boom--Right	Vertical	1.6	2	22
21	Boom--Left	Horizontal	Boom--Right	Horizontal	1.6	2	23

Table 3.3 shows measurements performed on a 6ft tractor on Oct 5, 2017. Amplifiers were set to displacement mode at 1 Hz for all experiments except trail 9 and 10 measured acceleration. Three sensors referred to yellow, green, and blue, were marked as Y, G, and B. Tractors did not have a speedometer, but they were controlled by gear setting and tachometer reading, where it was set to 2nd low gear at 2100 rpm. The equivalent speed was around 1.6 mph (0.7 m/s) which is similar to the swather's operating speed.

Table 3.3: October 05, 2017 Field Test Performed Using Displacement Measurements on 6 feet Tractor in Kernen field

	Yellow Sensor		Green Sensor		Blue Sensor		
Trail #	Position	Orientation	Position	Orientation	Position	Orientation	Scope Saved #
Natural Frequency- Calibration Test							
1	Boom--Left	Vertical	Boom--Left	Vertical	Boom--Left	Vertical	4-5
Natural Frequency							
2	Boom--Left	Vertical	Boom--Left-Mid	Vertical	Boom--Left	Horizontal	6-7
3	Boom--Left	Horizontal	Boom--Left-Mid	Horizontal	Boom--Left	Vertical	8
Field Test - Calibration							
4	Boom--Left	Vertical	Boom--Left	Vertical	Boom--Left	Vertical	9
Field Tests							
5	Boom--Left	Vertical	Boom--Left-Mid	Vertical	Boom--Center	Vertical	10-12
6	Boom--Left	Horizontal	Boom--Left-Mid	Horizontal	Boom--Center	Horizontal	13-15
7	Tractor--Seat	Horizontal	Tractor--3pt Hitch	Horizontal	Boom--Center	Horizontal	16-17
8	Tractor--Seat	Vertical	Tractor--3pt Hitch	Vertical	Boom--Center	Vertical	18
9*	Tractor--Seat	Horizontal	Tractor--3pt Hitch	Horizontal	Boom--Center	Horizontal	19
10*	Boom--Left	Horizontal	Boom--Left-Mid	Horizontal	Boom--Center	Horizontal	20

* Acceleration

Table 3.4 shows measurements performed on a 4ft tractor on Oct 5, 2017. Amplifiers were set to displacement mode of 1 Hz, except trail 19 and 20 measured the acceleration. The tractor was operated at the same speed of 1.6 mph roughly, where the gear was set to 1st high and the tachometer reading was 1750 rpm. Trail 21 performed displacement measurements at high speed (3rd high 1800 rpm), roughly 5 mph (2.2 m/s), and trail 22 tested the boom's frequency response on a paved road.

Table 3.4: October 05, 2017 Field Test Performed Using Displacement Measurements on 4 feet Tractor in Kernen field

	Yellow Sensor		Green Sensor		Blue Sensor		
Trail #	Position	Orientation	Position	Orientation	Position	Orientation	Scope Saved #
Natural Frequency- Calibration Test							
11	Boom--Left	Vertical	Boom--Left	Vertical	Boom--Left	Vertical	21
Natural Frequency							
12	Boom--Left	Vertical	Boom--Left-Mid	Vertical	Boom--Left	Horizontal	22
13	Boom--Left	Horizontal	Boom--Left-Mid	Horizontal	Boom--Left	Vertical	23
Field Test - Calibration							
14	Boom--Left	Vertical	Boom--Left	Vertical	Boom--Left	Vertical	24
Field Tests							
15	Boom--Left	Vertical	Boom--Left-Mid	Vertical	Boom--Center	Vertical	25-27
16	Boom--Left	Horizontal	Boom--Left-Mid	Horizontal	Boom--Center	Horizontal	28-30
17	Tractor--Seat	Horizontal	Tractor--3pt Hitch	Horizontal	Boom--Center	Horizontal	33
18	Tractor--Seat	Vertical	Tractor--3pt Hitch	Vertical	Boom--Center	Vertical	31-32
19*	Boom--Left	Horizontal	Boom--Left-Mid	Horizontal	Boom--Center	Horizontal	34-35
20*	Boom--Left	Horizontal	Boom--Left-Mid	Horizontal	Boom--Center	Horizontal	36
21**	Boom--Left	Vertical	Boom--Left-Mid	Vertical	Boom--Center	Vertical	37-38
22***	Boom--Left	Horizontal	Boom--Left-Mid	Horizontal	Boom--Center	Horizontal	39

* Acceleration; ** High Speed; *** Paved Road

Table 3.5 shows measurements performed on a 4ft tractor on Oct 5, 2017. Amplifiers were set to measure the acceleration. The tractor was operated at three different speed, including 1.1 mph, 1.6 mph, and 3.2 mph.

Table 3.5: August 23, 2018, Field Test Performed Using Acceleration Measurements on 6 feet Tractor in Kernen field

	Yellow Sensor		Green Sensor		Blue Sensor				
Trail #	Position	Orientation	Position	Orientation	Position	Orientation	Scope Saved #		
1	Boom--Left	Vertical	Boom--Left	Vertical	Boom--Left	Vertical			
Natural Frequency									
2	Boom--Left	Vertical	Boom--Left-Mid	Vertical	Boom--Left	Horizontal		1, 2, 3	
3	Boom--Left	Horizontal	Boom--Left-Mid	Horizontal	Boom--Left	Vertical		4, 5	
Field Test Speed							1.1 mph	1.6 mph	3.2 mph
4	Boom--Left	Vertical	Boom-Center	Vertical	Boom--Left-mid	Vertical	6, 7, 8	9	10
5	Boom--Left	Vertical	Swather-chassis	Vertical	Boom--Center	Vertical	11	12	13
6	Boom--Left	Horizontal	Boom-Center	Horizontal	Boom--Left-mid	Horizontal	14	15	16
7	Boom--Left	Horizontal	Swather-chassis	Horizontal	Boom--Center	Horizontal	17, 18	19	11, 12

3.2.3 Verification of FFT Method

Fast Fourier Transform (FFT) method converts a signal from the time domain to the frequency domain. This method was applied to find the frequency of the boom with data collected in the field tests. To verify the accuracy of this method, the natural frequency found numerically by analyzing the free vibration of the boom with FFT was compared with that from an analytical solution. The major component of the boom is a steel 5x6.7 C-channel. Since it was attached to a connection plate by 4 bolts in the middle, the boom was simplified as a 3 m long cantilever beam. Using the equation from [34], the analytical solution was calculated from

$$\omega = (\beta l)^2 \sqrt{\frac{EI}{\rho A l^4}} \tag{3.2}$$

where ω is the natural frequency of vibration, and βl is 1.875 for the first mode of vibration; E, Young's modulus, is 200 GPa; I, area moment of inertia, is $3.10*10^{-6}$ m^4; ρ, material density, is 7800 kg/m^3; A, cross-section area, is $1.257*10^{-3}$ m^2; and l, the length of the beam, is 3 m. And, natural frequency f in Hz is from

$$f = \frac{\omega}{2\pi} \tag{3.3}$$

The calculated natural frequency of this beam is 15.64 Hz (98.26 rad/s), and Appendix B: Analytical Solution of Vibrations of C-channel Boom shows the detailed calculation.

The movement of this cantilever beam was simulated using FEA software ANSYS classic. Since it was attached to a connection plate by 4 bolts in the middle, the boom was simplified as a 3 m long cantilever beam using steel 5x6.7 C-channel. The analytical solution was derived for the 2D beam, a 3D beam element, BEAM188, including 6 DOF. It was fixed in y-direction movement and both x-direction of rotation and z-direction of rotation to convert it to a 2D element. Figure 3.12 shows the FEA model, including 8 elements and 9 nodes. Modal analysis results of this beam were compared to the analytical solution as shown in Table 3.6.

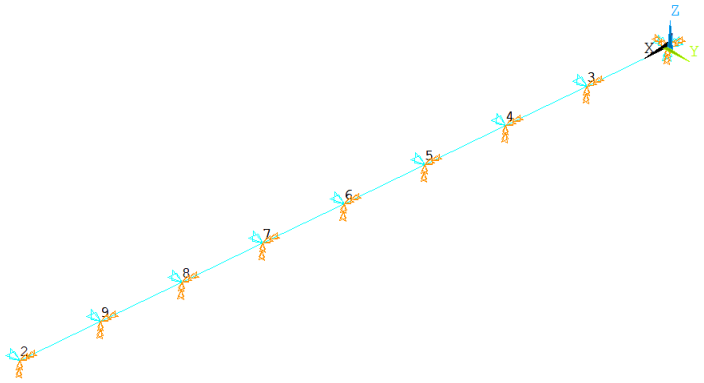

Figure 3.12: FEA Model of a 3 m Long 5x6.7 C-channel Beam

Table 3.6: Error Comparison from FEA Methods to Analytical Solution

# of Nodes	FEA Frequency	Error
1	14.473	7.64%
2	15.624	0.28%
3	15.627	0.26%
4	15.609	0.38%
5	15.597	0.46%
8	15.581	0.56%
10	15.577	0.58%
20	15.572	0.62%
100	15.570	0.63%

In the transient analysis, a 100 lb. impact load applied to the free end of the beam from 0.0001 to 0.0002 second generated beam end displacements in Figure 3.13-a. Figure 3.13-b is the FFT response in the frequency domain where the most outstanding peak is 15.60 Hz that is very close to the analytical solution, 15.64Hz. This showed that FFT routine used for analyzing experimental results is reliable. Appendix C: ANSYS Code for Vibration Verification includes the code for this section.

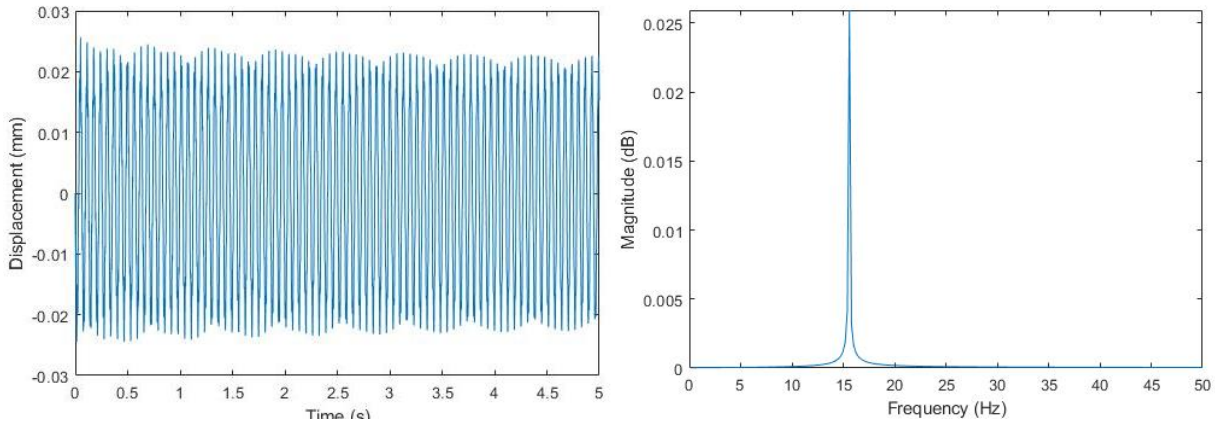

Figure 3.13-a: Displacement and FFT Frequency Response of 3 m Long Cantilever Beam End from FEA

3.3 Vibration Test Results and Discussion

Data measured from field experiments were further verified using FFT. The significances of the results are discussed in this Section to reveal how different factors influence each boom.

3.3.1 Vibration Test Results of the First-Generation Boom

As listed in Table 3.7, a model for 1st generation boom using 6 x 8.2 C-channel was built for FEA to find different vibration modes. The calculated modes are natural frequencies listed in the table, and corresponding mode shapes which are eigen vectors of the system are plotted in Figure 3.14. The figure shows the first 4 mode shapes from FEA and their corresponding frequencies, where vibration in the X-Y plane is considered as horizontal vibration, and in X-Z plane as vertical. Mode 1, 4, and 7 include horizontal displacements, while the others are in vertical displacements.

Table 3.7: Modals Calculated with FEA for 1st Generation Boom

Mode	Frequency (Hz), FEA	vibration direction	Horizontal (Hz)	Vertical (Hz)
1	4.8	Horizontal	4	
2	14.1	Vertical		
3	22.7	Vertical		
4	30.1	Horizontal	26	
5	47.2	Vertical		
6	79.1	Vertical		64
7	86.5	Horizontal	86	
8	114.4	Vertical		
9	130	Vertical		133

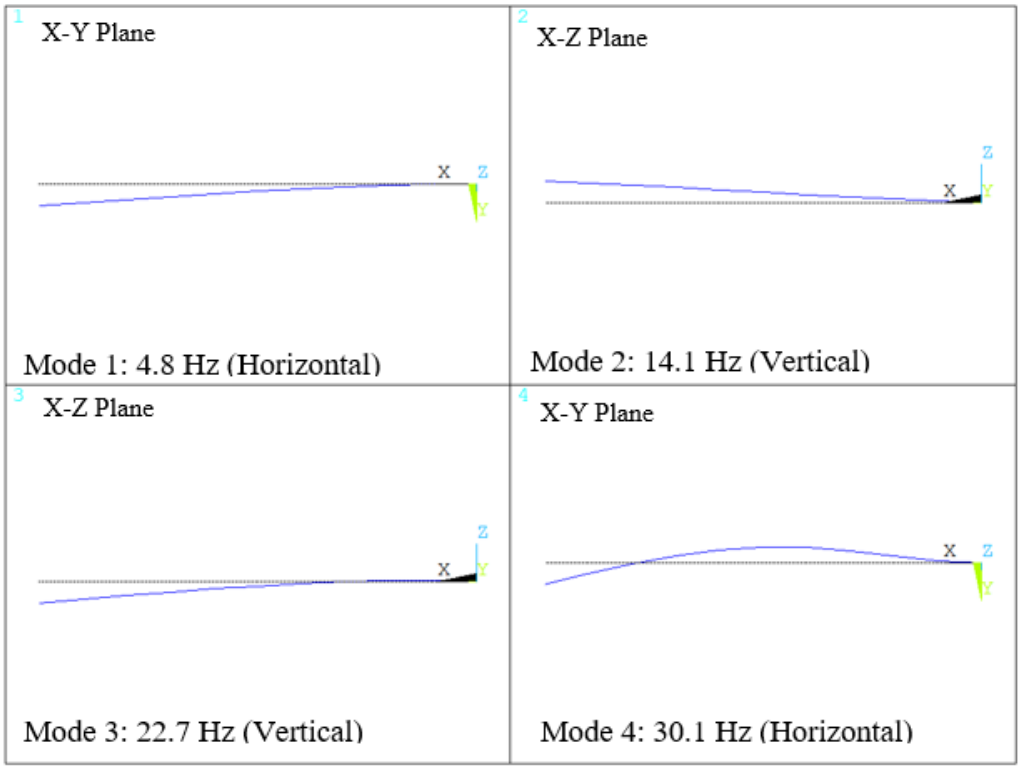

Figure 3.14: FEA Results- First 4 Mode Shapes of 6 x 8.2 C-channel

In the field experiments, both acceleration and displacement measurements for the 1st generation boom were performed, but only higher frequencies were recorded for acceleration measurements due to the equipment limitations. In these experiments, accelerometers were placed on the left end of the boom horizontally (or vertically) to measure acceleration changes caused by a horizontal (or vertical) impact shown in Figure 3.15. Measurements were analyzed with FFT. For example, Figure 3.16-a shows acceleration changes caused by vertical impact when sensor 1 and sensor 2 were placed vertically at the left end and the center of the boom separately. Figure 3.16-b is the frequency response of the measurements. In the horizontal direction, the dominant frequency is 26 Hz, and other outstanding frequencies include 4Hz and 83 Hz which corresponds to FEA values of 30.1 Hz, 4.8 Hz, and 86.5 Hz in Table 3.7. Same tests were performed in the vertical direction, where 64 Hz and 133 Hz are observed while corresponding FEA values are 79.1 Hz and 130 Hz. The difference is due to simplifying the link between the boom and the swather to fixed connections; meanwhile, the actual connection allows some movements, especially in the vertical direction. Thus, the difference is larger in the vertical direction. Overall, experimental results are consistent with FEA values.

Figure 3.15: Vertically and Horizontally Mounted Sensors at the Left End of the 1st Gen Boom

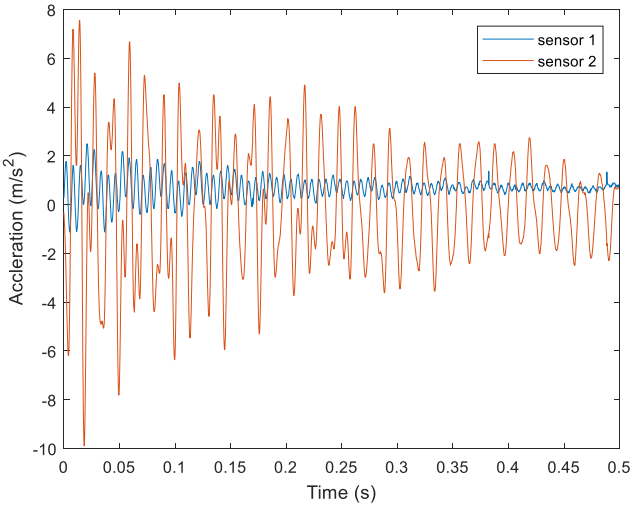

Figure 3.16-a: Experimental Natural Frequency Measurements of Acceleration of 1st Generation Boom (May 31, Scope 34)

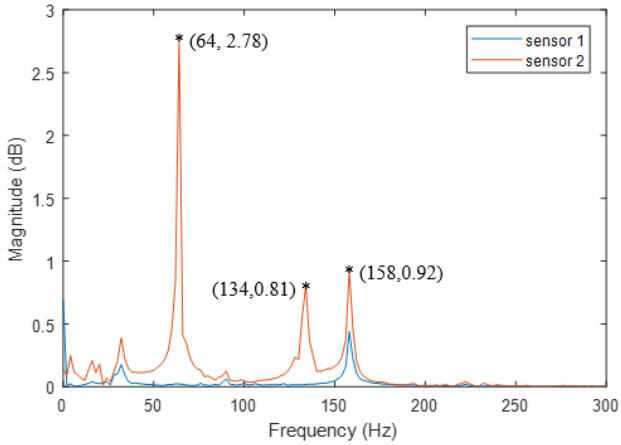

Figure 3.16-b: Natural Frequency Response of 1st Generation Boom (May 31, Scope 34)

After observing boom's motion, it showed that the selected sensors, such as ultrasound sensors and cameras, were more sensitive to low-frequency vibrations, so displacement measurements were investigated when data were sampled at a lower rate with a longer duration. First, both sensors were verified to give same measurements and spectrums before field tests. Some of these verification results were demonstrated in Figure 3.17. Then, tests were performed as listed in Table 3.2.

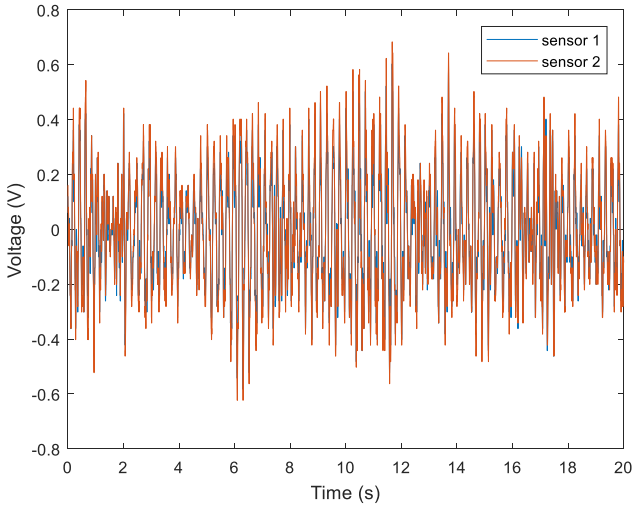

Figure 3.17-a: Experimental Measurements of Output Signal from Both Transducers in Displacement Tests (May 31, Scope 5)

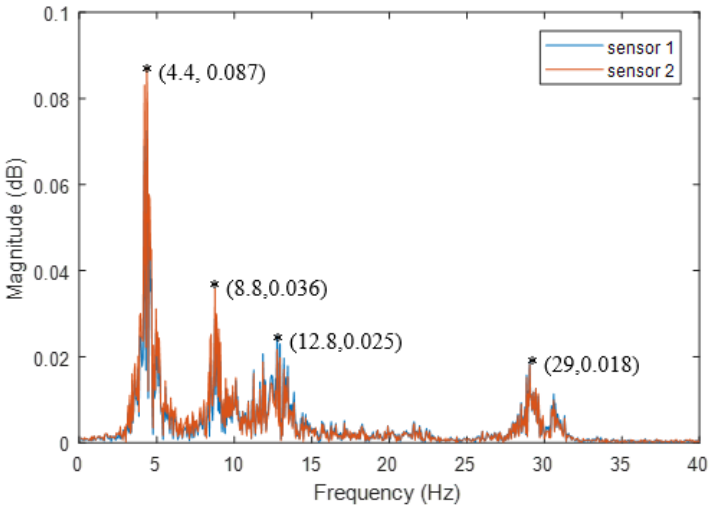

Figure 3.17-b: Frequency Response of Output Signal from Both Transducers in Displacement Tests (May 31, Scope 5)

Forced vibration experiments were performed to investigate how vibrations influence the boom. By placing sensors at different locations on the boom and swather when the vehicle was traveling at 1.6 mph or 4.5 mph on 2 paths, vibrations were documented and compared. For example, one of measurements taken at the left end of the boom when the swather was traveling

at 1.6 mph is shown in Figure 3.18. After comparing measurements from different locations, it stated that vibration spectrums were similar in both horizontal and vertical measurements. The most dominant frequency was around 4.3 Hz and other outstanding frequencies include 8.8 Hz, 12.8 Hz, and 30 Hz. After converting the measurements from voltage to displacement, the maximum deflection was about 17 mm. In addition, when Tractor was traveling at a higher speed, roughly 4.5 mph, the measured frequency was about 11.9 Hz. Figure 3.19 shows these results where the maximum deflection was about 16mm at the tip of the boom. Therefore, the tractor activated the closest natural frequency to its operating speed.

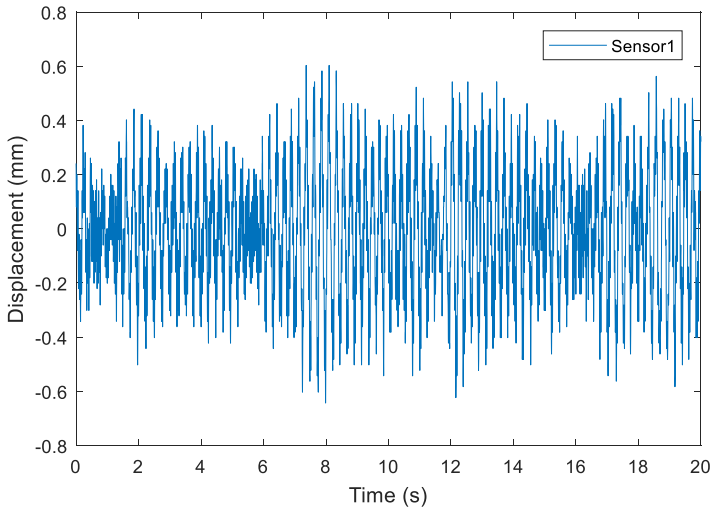

Figure 3.18-a: Vertical Displacement of 1st Gen Boom Left End of Swather at 1.6 mph Speed (July 25, Scope 9)

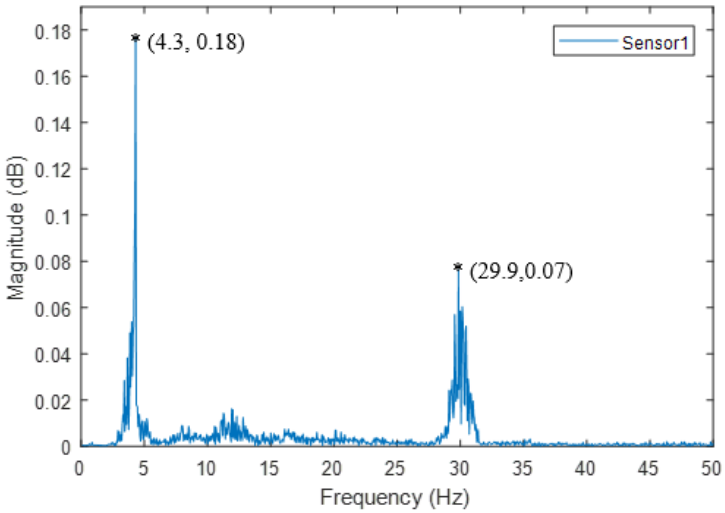

Figure 3.18-b: Frequency Response of 1st Gen Boom Left End of Swather at 1.6 mph Speed (July 25, Scope 9)

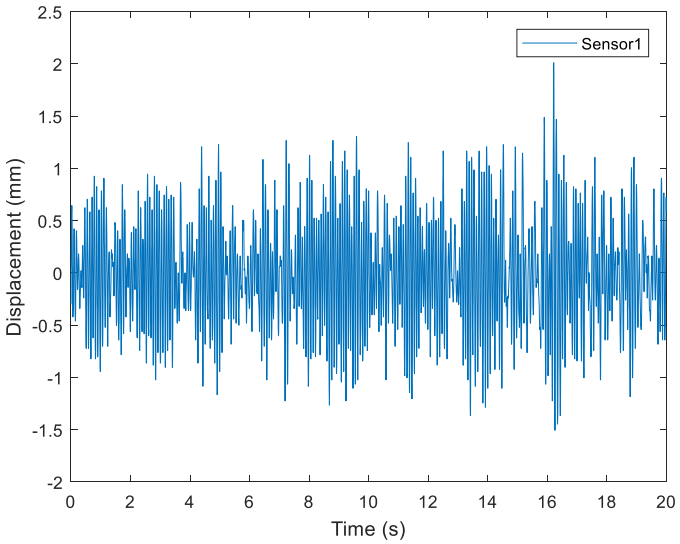

Figure 3.19: Vertical Displacement of 1st Gen Boom Left End of Swather at 4.5 mph Speed (July 25, Scope 16)

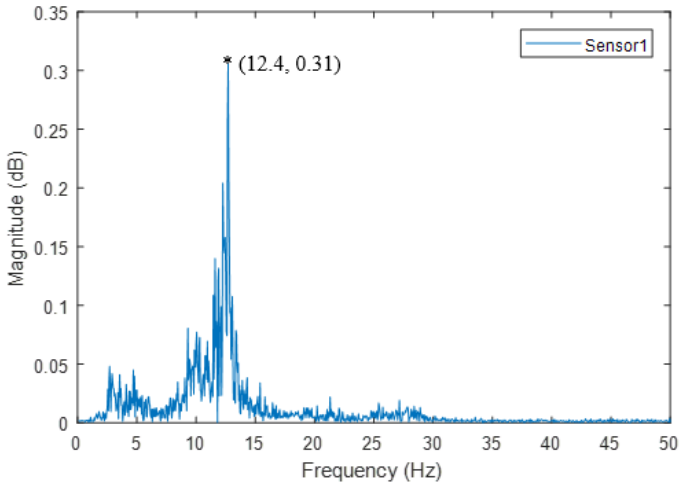

Figure 3.19-b: Frequency Response of 1st Generation Boom Left End of Swather at 4.5 mph Speed (July 25, Scope 16)

On another path (track 2) with a similar surface condition, even though measured frequency peaks were slightly different shown in Figure 3.20, the dominant frequency was still around 4.3 Hz when other outstanding frequencies included 8.7 Hz and 29.1 Hz. These results were very similar to those from track 1.

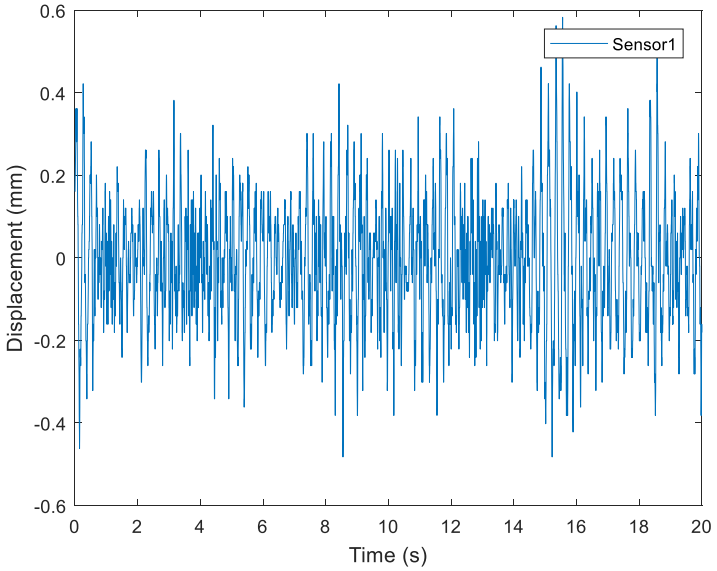

Figure 3.20-a: Vertical Displacement of 1st Gen Boom Left End of Swather on a Different Road (July 25, Scope 22)

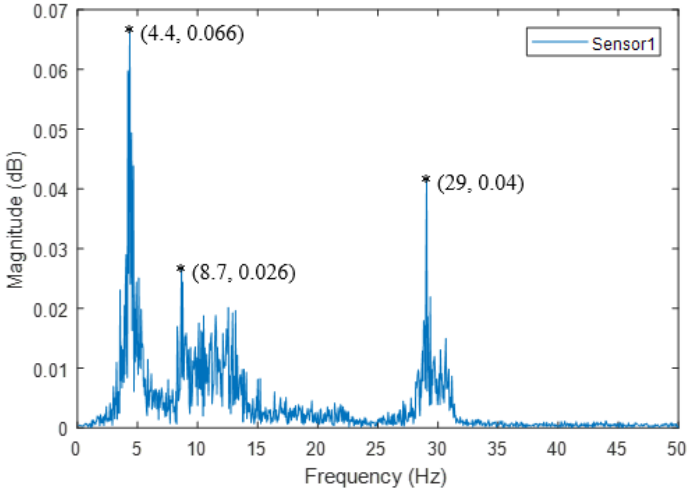

Figure 3.20-b: Frequency Response of 1st Gen Boom Left End Vertically on a Different Road (July 25, Scope 22)

The overall results for 1st generation boom are listed in Appendix D: Frequency Analysis Results, and the major results are summarized in Table 3.8. At the 1.6mph speed, the vibration frequency of the vehicle is 4.4 Hz when it activates the boom to vibrate around 4.3 Hz which is close to the 4.8 Hz natural frequency from FEA results; and, at 4.5 mph speed, the 12.5 Hz Vehicle vibration induces the 11.9 Hz Vibration to the boom when the 2nd mode vibration from FEA is 14.1 Hz. Thus, considering the rough path surface, the vibration measurements are consistent with FEA.

Table 3.8: Vibration Frequency Measurements in 1st Generation Boom

Speed	Road #	Swather Dominant Frequency (Hz)	Boom Dominant Frequency (Hz)
1.6 mph	1	4.4	4.3
1.6 mph	2	4.3	
4.5 mph	1	12.5	11.9

3.3.2 Vibration Test Results and Discussion for the Second-Generation Boom

As listed in Table 3.9, a model for 2nd generation boom using 5*6.7 C-channel was built for FEA to find different vibration modes. The analysis results reveal that mode 1, 4, 6, and 10 include horizontal displacements, while the others are in vertical displacements. The first four mode shapes are shown in Figure 3.21.

Table 3.9: FEA Results- Natural Frequencies for the 2nd Generation Boom

Mode	Frequency (Hz)	Vibration Direction
1	4.3	Horizontal
2	13.5	Vertical
3	22.2	Vertical
4	27.3	Horizontal
5	50.9	Vertical
6	76.6	Horizontal
7	83.7	Vertical
8	113.8	Vertical
9	121.8	Vertical
10	151.1	Horizontal

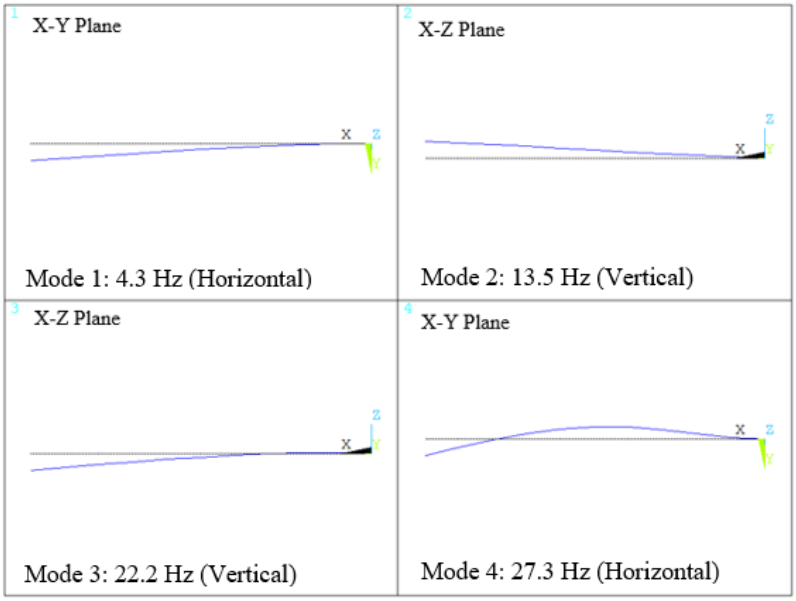

Figure 3.21: FEA results- First 4 Mode Shapes of 5 x 6.7 C-channel

Before experiments, three sensors were tested at the same location on the boom when the boom was impacted with a hammer. Figure 3.22 illustrates the location of 3 sensors which are

labeled as green, yellow, and blue, when the boom was impacted once during one test on August 5, 2018. Figure 3.23 shows measurements where three sensors measured the same patent data with identical peaks and data duration, but the output voltages had some differences when the vibrations were damped. The reason is that these sensors are very sensitive, so equipment, including amplifiers and cables, can induce significant noise to the output when vibration is very small.

Figure 3.22: Sensor Location of Natural Frequency Measurements Performed on 2nd Gen Boom

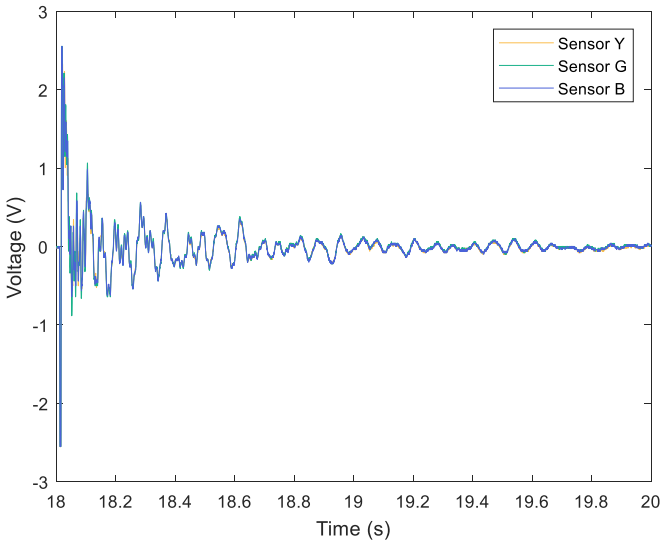

Figure 3.23: Natural Frequency Measurements from Sensor Calibration Experiment (Aug 23, Scope 1)

To find boom vibration frequencies during the phenotyping process, acceleration measurement was carried out, to find high frequencies. The dominant vibration frequency measured from the 6-ft tractor was around 124 Hz, while other vibration frequencies included 88 Hz, 160 Hz, and 214 Hz. Vibration measurements and FFT results of the left end of the boom are

demonstrated in Figure 3.24. For boom attached to the 6-ft tractor, it showed that the dominant vibration frequency was 159 Hz and other outstanding frequencies include 4.7 Hz, and 123 Hz. The boom and the tractor had similar vibration frequencies about 124 Hz and 160 Hz, when the activated boom vibration is 1st mode around 4.7 Hz. When the same boom was attached to a 4ft tractor shown in Figure 3.25, the dominant frequency was 10.1 Hz corresponding to the 2nd mode.

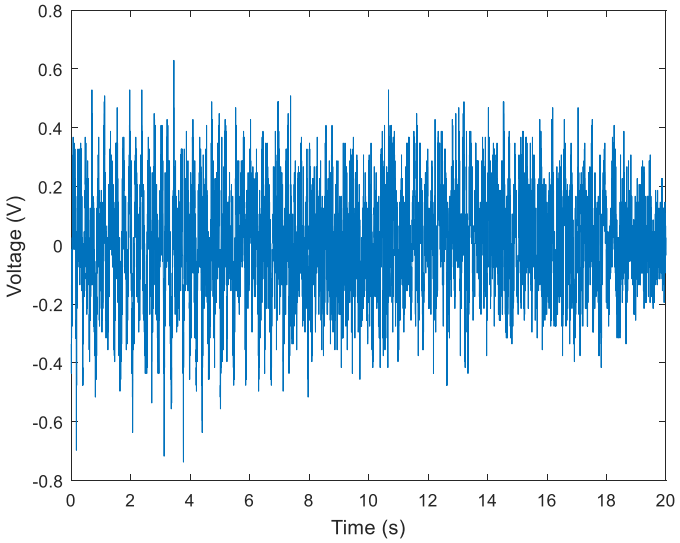

Figure 3.24-a: Horizontal Sensor Measurements of 2nd Gen Boom Left End of 6-ft Tractor (Oct 05, Scope 20)

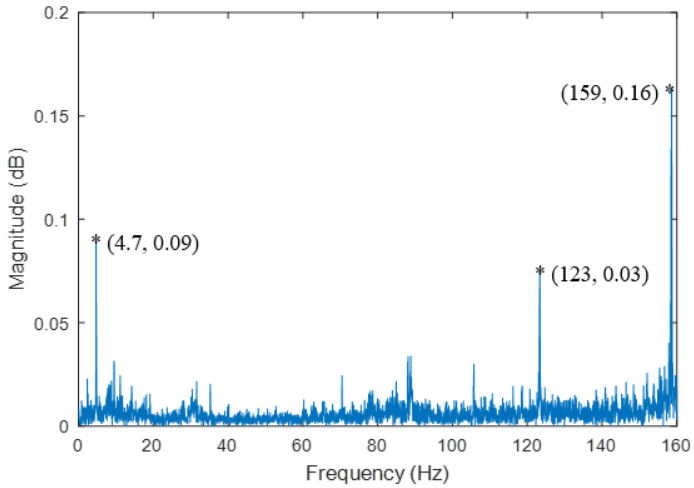

Figure 3.24-b: Frequency Measurements of 2nd Gen Boom Left End of 6-ft Tractor (Oct 05, Scope 20)

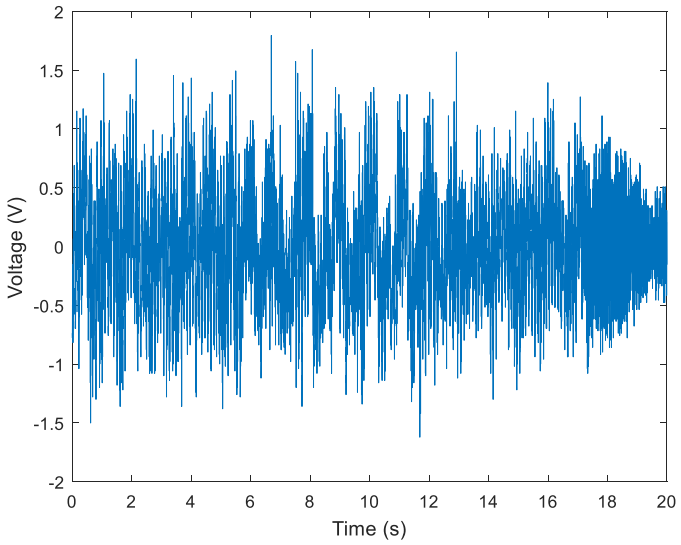

Figure 3.25-a: Vertical Sensor Measurements of 2nd Gen Boom Left End of 6-ft Tractor (Oct 05, Scope 35)

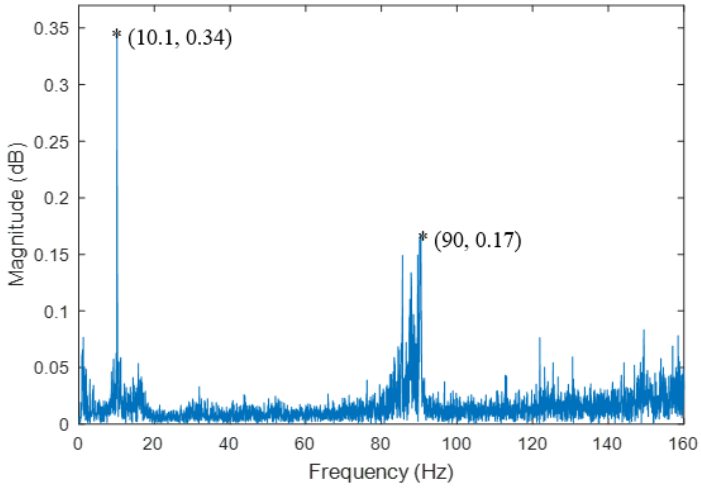

Figure 3.25-b: Vertical Sensor-Measurements of 2nd Gen Boom Left End of 6-ft Tractor (Oct 05, Scope 35)

To find vibrations caused by traveling on rough roads, the amplifier was set to 1 Hz mode to collect low-frequency data. The measurements show that tractor, 3-point hitch, and boom center had similar dominant vibration frequencies. Figure 3.26 shows one measurement from the left end of the boom, and other measurements have similar results. Based on laboratory results, the conversion from voltage measurements to actual displacement was about 1 V to 10 mm. The detailed explanation of this conversion is described in Appendix A: Amplifier type 2635 from Bruel & Kjar. Thus, the maximum displacement in this test was about 33 mm as shown in Figure 3.26.

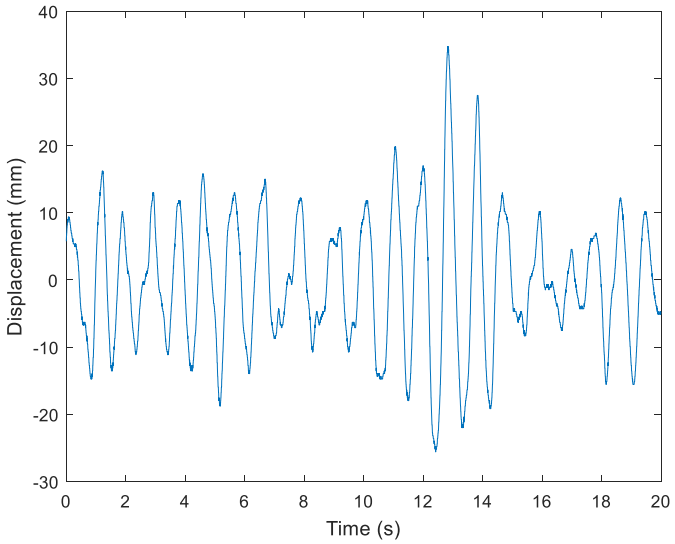

Figure 3.26: Measurements and FFT of 6-ft Tractor Left End Vertically (Oct 05, Scope 10)

Similar experiments were performed on the 4-ft tractor, where major results are shown in Table 3.10. Figure 3.27 shows displacement measurements in mm when the maximum deflection of the boom was about 100mm.

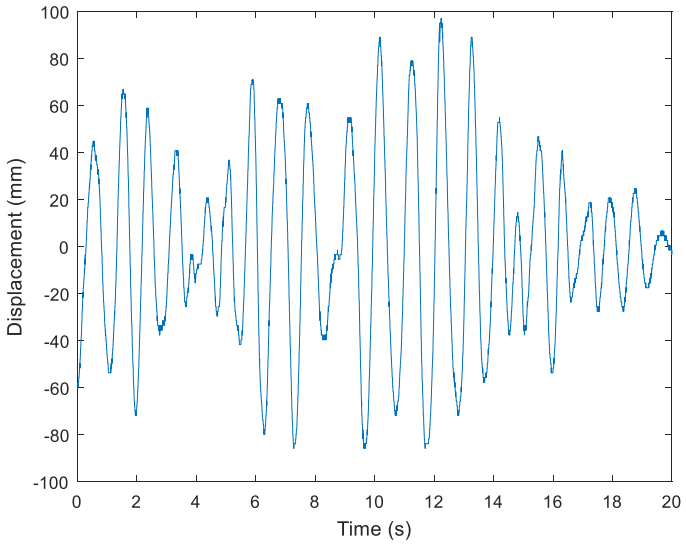

Figure 3.27: Vertical Displacement Measurements of 4-ft Tractor Left End (Oct 05, Scope 25)

A summary of experimental results from 2nd generation boom is demonstrated in Table 3.10, and completed test results are demonstrated in Frequency Analysis Results. Since 2nd generation boom has several components rather than a simple C-channel, both pre-tensioned winch cables and bolted joints provide extra stiffness to the boom. Therefore, measured frequencies were slightly higher than the FEA results.

Table 3.10: Tractors and 2nd Generation Boom Experiment Results

	Speed (Mph)	Road Condition	Frequencies (Hz)			
6ft tractor	1.6	unpaved	88	124	160	214
Boom on 6ft Tractor	1.6	unpaved	4.7	11.2	31.6	123.4
Boom on 4ft Tractor	1.6	unpaved	2	10.1	90.5	

3.3.3 Discussions about Vibration Experiment Results

By comparing measurements to analysis results, it showed that vibration in booms is affected by several factors, including types of vehicles, operating speed, field roughness, etc. First, the size of vehicles can significantly influence a boom's vibration. Displayed in Figure 3.28, the 4ft tractor had at least twice of the vibration amplitude as that measured in 6ft Tractor when operated on the same road at similar operating speed. Meanwhile, the 8-ft wide swather had less vibration than tractors. The major reason for different vibration amplitude is due to the size of the vehicles. The 4-ft tractor is the smallest vehicle which is shown in Figure 3.29; the 6-ft tractor is wider and larger shown in Figure 2.24; and, the 8-ft wide swather is demonstrated in Figure 2.23. Since a larger vehicle is also wider, it has a better resistant to vibration. Therefore, increasing the size of a vehicle benefits reducing the amplitude of the vibration.

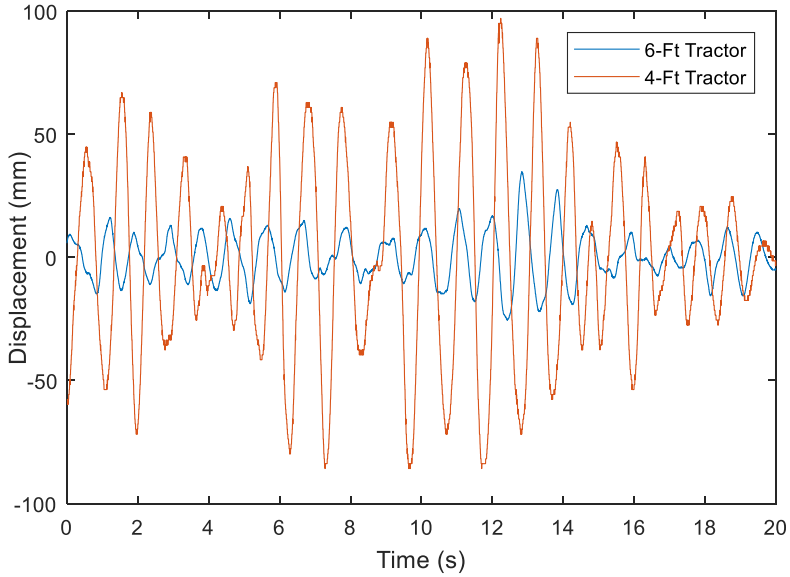

Figure 3.28: Displacement Comparison of Vertical Displacement at Beam End between 4-Ft and 6 Ft-Tractors (Scope 10 & 25)

Figure 3.29: 2nd Generation Boom Mounted on a 4ft-Tractor in the Vibration Test

Second, a vehicle's traveling speed also impacts boom's vibration. Frequencies measured in the swather are positively related to the swather speed where a 180% increase in speed caused the same percentage increase in the vibration frequency. In both cases, the dominant frequencies measured in the boom were very close to the swather's frequency, meaning the swather caused the boom to vibrate around certain frequencies close to its natural frequencies. To reduce vibration in the boom, the operating speed of the vehicle should be carefully selected to avoid resonance.

Third, road conditions influence the vibration frequency significantly. Frequency responses were matching when the boom was attached to the swather traveling at the same speed on similar paved farm fields. Meanwhile, vibration frequencies were very different in frequencies and amplitudes between different road conditions such as paved and unpaved roads. Figure 3.30 shows the data collected and analyzed from both paved and unpaved roads, in which the paved road induced more uniformed vibrations. There were fewer outstanding frequencies observed through FFT, and the dominant frequency had a much larger amplitude than the rest. On the other hand, the unpaved road had several peaks with similar values around the most dominant peak. The possible reason is that unpaved fields have diverse surface conditions affecting the operation of vehicles, so vibrations changes along traveling through the field.

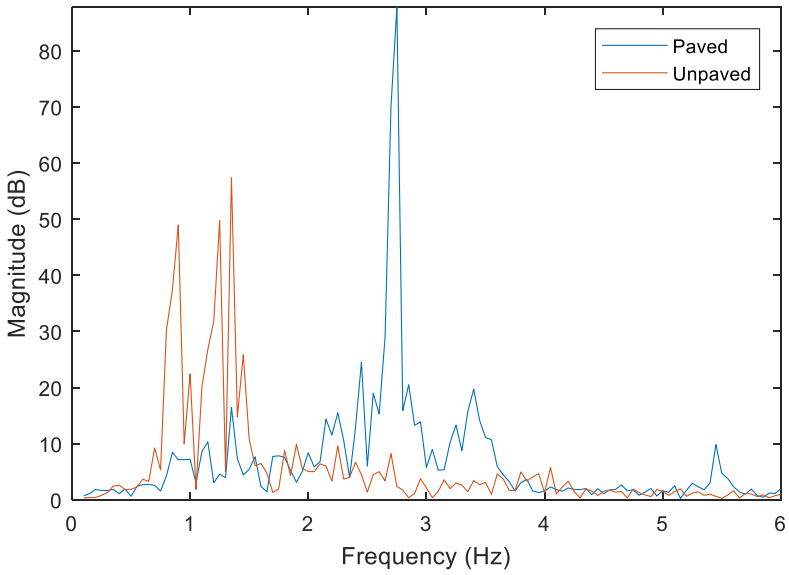

Figure 3.30: Frequency Response of Boom End of 4ft-Tractor Operated on Paved and Unpaved Road (Oct 05, Scope 26 & 39)

Finally, at different Locations on the boom, frequency responses are alike, but displacements are proportional to the distance from the center of the boom. It was observed that attaching sensors to different locations on the same boom gives matching outstanding frequencies. The dominant vibration frequency for the 1st generation boom is 4.3 Hz, and 4.7 Hz for 2nd generation boom attached to the 6ft tractor when it is 2 Hz on the 4ft tractor. However, the vibration magnitudes are proportional to the distance from the center of the boom. The further a sensor is located from the center of the boom, the more vibration amplitude it has. For example, three transducers attached to the left end (3 m from the center), middle of the left section (1.75 m from the center), and center of the boom on the 6ft-tractor colored as yellow, green and blue have displacement measurements shown in Figure 3.31. These sensors measured the same dominant frequency around 1.1 Hz. Nevertheless, magnitudes of the peaks were 5.8 dB, 3.4 dB, and 0.82 dB accordingly, so the closer a sensor is located to the end of a boom, the larger vibration amplitude is measured. Since the dominant frequency measured was 4.7 Hz for this boom mounted to the 6ft tractor, it was close to the first modal from FEA result. In this vibration, the location of measurements and vibration amplitudes were proportional to each other. This represents that the 2nd generation boom was in the first modal vibration. Measurements for the other boom indicated the same relationship.

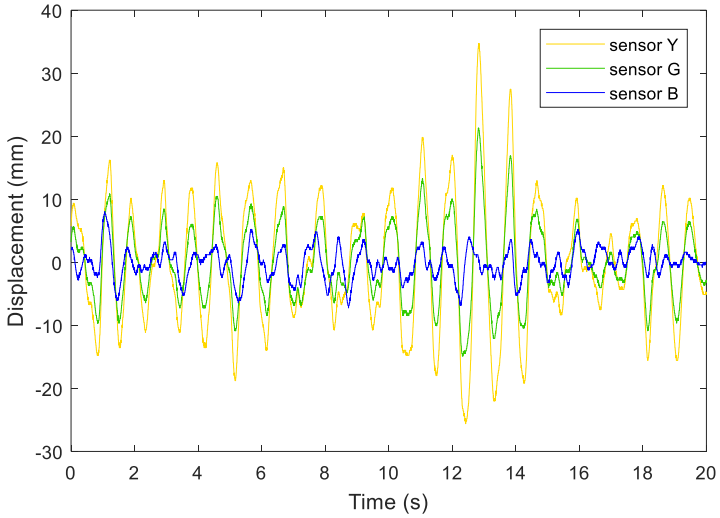

Figure 3.31-a: Displacement Measurements at 3 Selected Locations on the Boom Attached to a 6ft-Tractor (Oct 05, Scope 10, Y: left end, G: left-mid, B: center)

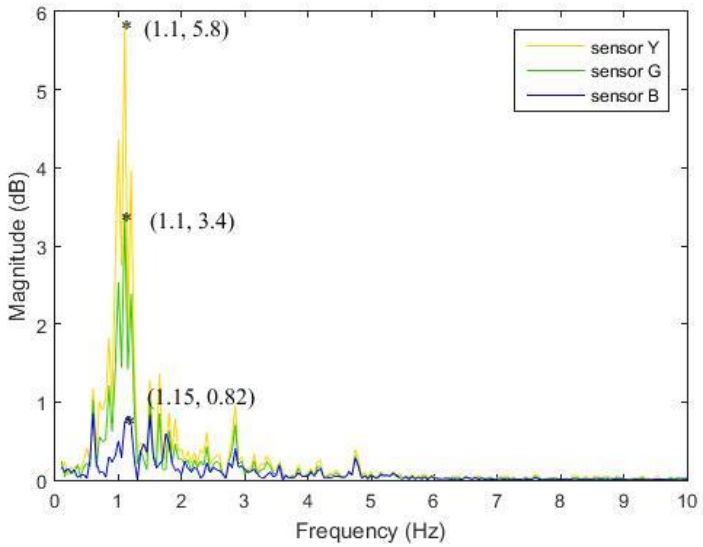

Figure 3.31-b Frequency Response of Boom Attached to a 6-ft Tractor (Y: left end, G: left-mid, B: center)

3.4 Summary

This chapter discussed how field and mechanical factors influence the functionality of a newly developed phenotyping platform. It proved that different vehicles, road conditions, operating speed, and sensor locations, can affect the phenotyping platform's vibration spectrum significantly. The vibrations were also quantified for different vehicles and their booms. Choosing a proper vehicle, boom which carries imaging equipment, and operating conditions are very important; in this case, a larger swather operated at moderate speed, 1.6 mph, can provide accurate measurements, even with vibration induced from rough farm fields.

Chapter 4 Analysis of the Third-Generation Boom/Robotic Arm

The 3rd generation boom is a hybrid 5 DOF robotic arm proposed for plant phenotyping application providing enough mobility and flexibility to collect data from crops grown in a large farm field. This arm meets the height and reach requirements of multiple sensors, including cameras, ultrasound sensors, thermometers, and NDVI sensors. To properly control the motion of this robotic arm, it is important to understand the reach of the arm and accurately identify the torque/force requirements at each joint in operations. Therefore, it is necessary to investigate the kinematics and dynamics of the manipulator. This chapter covers the analysis of forward and inverse kinematics, dynamics with Newton-Euler method, simulations, and experimental verifications. Derived theoretical kinematics results are compared with measurements of a small parallel robotic arm to verify its accuracy; the simulation of this robotic arm is performed through SIMULINK and compared with the Newton-Euler method to reveal if methods are appropriate for this robot.

Finally, the range of torques and forces from dynamics analysis at each joint is determined for a proposed preliminary design to select the proper actuators and control units.

4.1 Forward and Inverse Kinematics

To analyze the motion of the 3rd generation robotic arm, it is essential to precisely describe the orientation of the robotic arm and the relationship between individual sections and joints such that kinematics and dynamics analysis can be performed. Shown in Figure 4.1 and Figure 4.2, a coordinate system is assigned to each joint when the structure of the robotic arm is altered slightly for a better demonstration, where Table 4.1 demonstrates the coordinate systems associated to the robot and Figure 4.2 is the schematic of same coordinate systems for better illustration. The coordinate system with note ‘0’ is the world frame, and each subsequent coordinate system is assigned to one joint in the robotic arm, such as ‘1’ is associated to joint 1 which is the base motor. Meanwhile, coordinate systems from 7 to 9 are labeled at the joints in the parallel mechanism. In each coordinate system, the z-axis is coincident with the axis of rotation or the direction of linear motion; x-axis is the common normal, and y-axis follows the right-handed coordinate system. When a common normal does not exist, the x’ is assigned to facilitate calculating transform matrix. The coordinate system in red color shows the orientation

of the major arm section, and the blue system describes the orientation of the parallel arm section of the hybrid arm. The angle of rotation for each joint is demonstrated in Figure 4.3, where each angle shows the rotation of x-axis in two adjacent coordinate systems in a counter-clockwise direction. It shall be noticed that θ_6 describes the rotation from x_4' to x_5. Due to the parallelism, coordinate systems at joint 3 and 9 have the same angle of rotation. Finally, parameters L_i's indicating the length of each section are labeled in Figure 4.4.

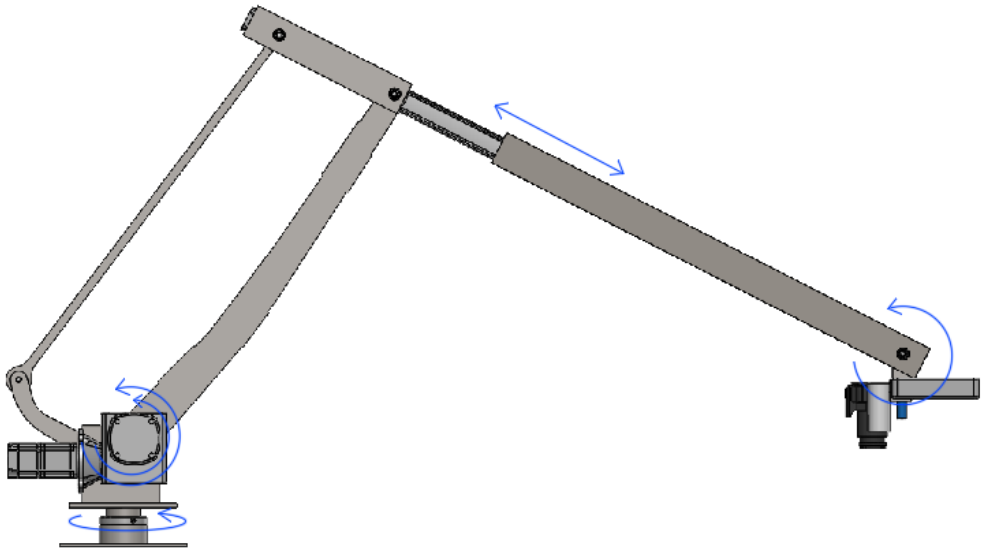

Figure 4.1: Schematic of DOFs in 5-DOF Robotic Arm

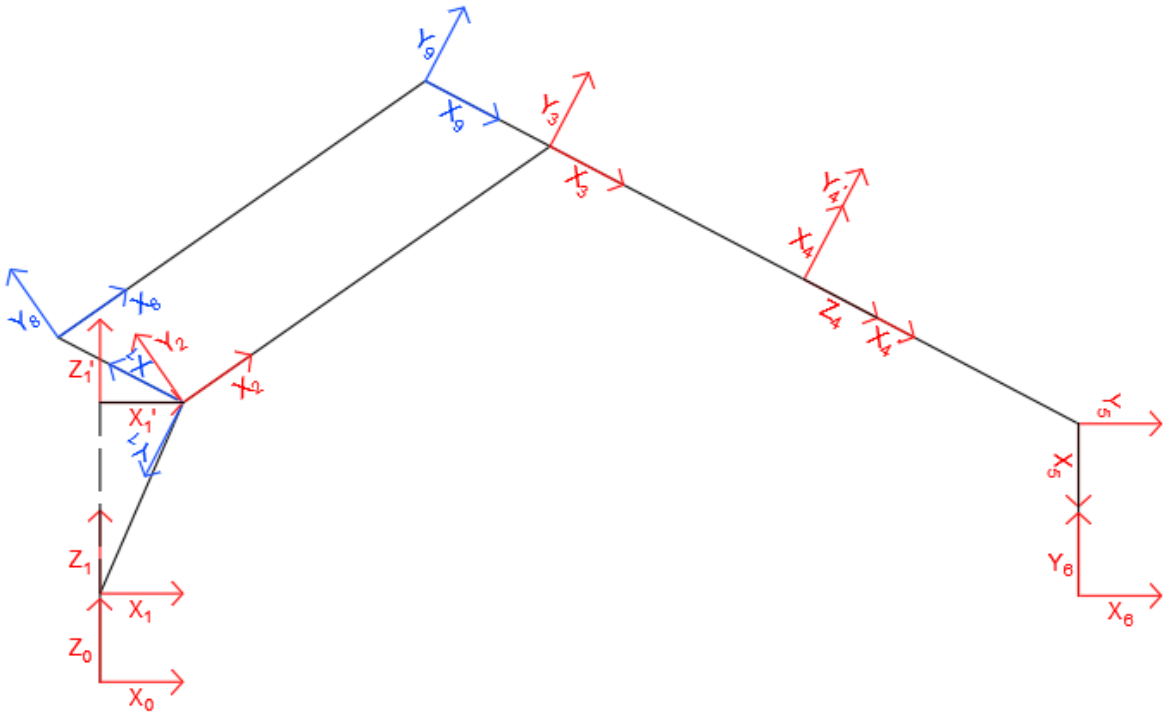

Figure 4.2: Coordinate System in the Front View of the Robotic Arm

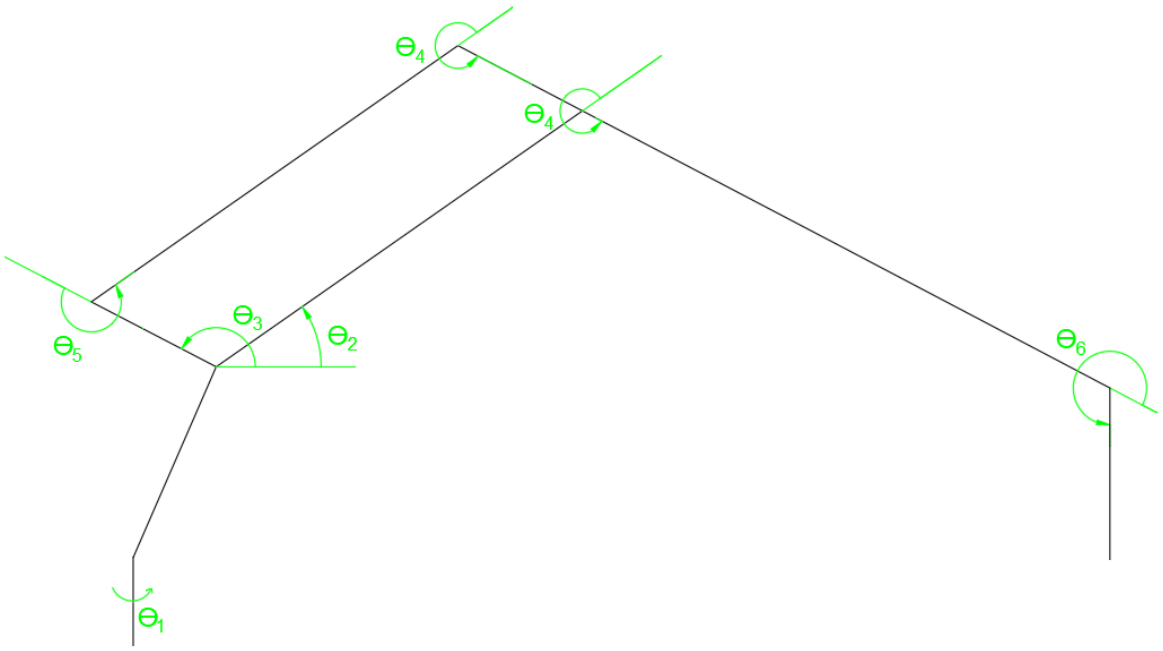

Figure 4.3: Angle in the Front View of the Robotic Arm

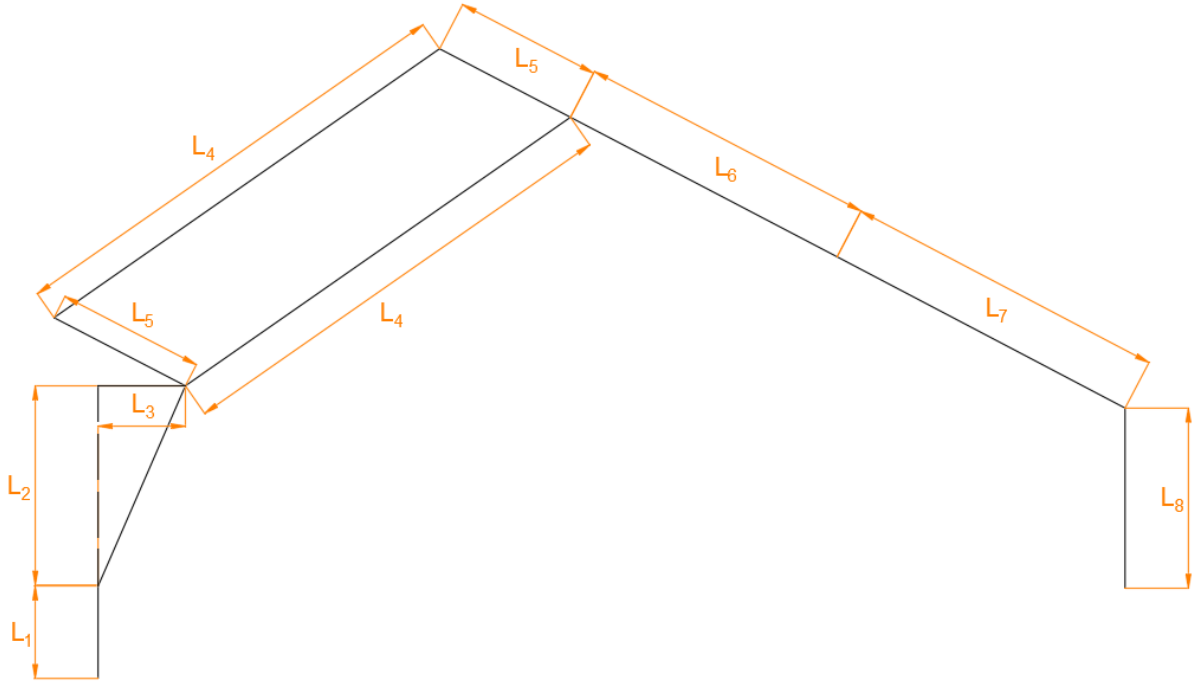

Figure 4.4: Length in the Front View of the Robotic Arm

Based on the assigned coordinate system, D-H (Denavit–Hartenberg) parameters are used to describe the position and orientation of the arm and to find its transform matrices [35]. In the modified D-H parameters, four variables are described as,

d: offset along previous z to the common normal,

θ: angle about the previous z, from old x to new x,

a: length of the common normal,

α: angle about common normal, from old z-axis to new z-axis.

With coordinate system and dimensions labeled in Figure 4.2 to Figure 4.4, the D-H parameters for this robot are summarized in Table 4.1, where i (from 1 to 9) indicates the new coordinated system at the current joint and i-1 describes the old ones at the previous joint; however, for parallel sections, the coordinate systems are indicated in the parentheses.

Table 4.1: DH Parameters for the 5 DOF Robotic Arm (3rd Gen Boom)

i	α_{i-1} (r)	a_{i-1}	d_i	Θ_i
1	0	0	L_1	Θ_1
1'	0	0	L_2	0
2	90°	L_3	0	Θ_2
3	0	L_4	0	Θ_4
5	0	0	L_7	Θ_6
6	0	L_8	0	90°
7(from 1')	90°	0	L_2	Θ_3
8(from 7)	0	L_5	0	Θ_5
9(from 8)	0	L_4	0	Θ_4
3(from 9)	0	L_5	0	0

$* where\ \Theta_4 = \Theta_3 - \Theta_2 + 180°, \Theta_5 = \Theta_2 - \Theta_3;$
$if\ the\ end\ effector\ facing\ down\ \Theta_6 = 90° - \Theta_3$

The D-H parameter method has some limitation. It is impossible to write the transfer matrices for the joints that are adjacent to prismatic joints with D-H method because x-axes and z-axes are collinear. However, the rotation matrix (R) and transform matrix (T) can still be written for frame 3 in terms of frame 2 as following

$$ {}^{3}_{4}R = \begin{bmatrix} 0 & 0 & 1 \\ 1 & 0 & 0 \\ 0 & 1 & 0 \end{bmatrix} \tag{4.1} $$

Since a transfer matrix can be written as rotation matrix and displacement matrix as

$$ {}^{i}_{i+1}T = \begin{bmatrix} {}^{i}_{i+1}R & {}^{i}_{i+1}P \\ 0 \quad 0 \quad 0 & 1 \end{bmatrix} \tag{4.2} $$

$$ {}^{3}_{4}T = \begin{bmatrix} 0 & 0 & 1 & L_6 \\ 1 & 0 & 0 & 0 \\ 0 & 1 & 0 & 0 \\ 0 & 0 & 0 & 1 \end{bmatrix} \tag{4.3} $$

$$ {}'^{4}_{4}T = \begin{bmatrix} 0 & 1 & 0 & 0 \\ 0 & 0 & 1 & 0 \\ 1 & 0 & 0 & 0 \\ 0 & 0 & 0 & 1 \end{bmatrix} \tag{4.4} $$

Based on the modified D-H parameters from the previous part and equation below, the transform matrices from frame 0 to frame 5 can be written as following, where c refers to cosine and s refers to sine. For example, c1 represents sin (θ_1) and c_{12} represents sin ($\theta_1 + \theta_2$).

$$ {}^{i-1}_{i}T = \begin{bmatrix} c\theta_i & -s\theta_i & 0 & a_{i-1} \\ s\theta_i c\alpha_{i-1} & c\theta_i c\alpha_{i-1} & -s\alpha_{i-1} & -d_i s\alpha_{i-1} \\ s\theta_i s\alpha_{i-1} & c\theta_i s\alpha_{i-1} & c\alpha_{i-1} & d_i c\alpha_{i-1} \\ 0 & 0 & 0 & 1 \end{bmatrix} \tag{4.5} $$

$$ {}^{0}_{1}T = \begin{bmatrix} c1 & -s1 & 0 & 0 \\ s1 & c1 & 0 & 0 \\ 0 & 0 & 1 & L_1 \\ 0 & 0 & 0 & 1 \end{bmatrix} \tag{4.6} $$

$$ {}^{1}_{2}T = \begin{bmatrix} 1 & 0 & 0 & 0 \\ 0 & 1 & 0 & 0 \\ 0 & 0 & 1 & L_2 \\ 0 & 0 & 0 & 1 \end{bmatrix} \begin{bmatrix} c2 & -s2 & 0 & L_3 \\ 0 & 0 & -1 & 0 \\ s2 & c2 & 0 & 0 \\ 0 & 0 & 0 & 1 \end{bmatrix} = \begin{bmatrix} c2 & -s2 & 0 & L_3 \\ 0 & 0 & -1 & 0 \\ s2 & c2 & 0 & L_2 \\ 0 & 0 & 0 & 1 \end{bmatrix} \tag{4.7} $$

$$ {}^{2}_{3}T = \begin{bmatrix} -c4 & s4 & 0 & L_4 \\ -s4 & -c4 & 0 & 0 \\ 0 & 0 & 1 & 0 \\ 0 & 0 & 0 & 1 \end{bmatrix} \tag{4.8} $$

$$ {}^{3}_{4}T = \begin{bmatrix} 0 & 0 & 1 & L_6 \\ 1 & 0 & 0 & 0 \\ 0 & 1 & 0 & 0 \\ 0 & 0 & 0 & 1 \end{bmatrix} \tag{4.9} $$

$$ {}^{4}_{5}T = {}'^{4}_{4}T\,{}^{4'}_{5}T = \begin{bmatrix} 0 & 1 & 0 & 0 \\ 0 & 0 & 1 & 0 \\ 1 & 0 & 0 & 0 \\ 0 & 0 & 0 & 1 \end{bmatrix} \begin{bmatrix} c1 & -s1 & 0 & L_7 \\ s1 & c1 & 0 & 0 \\ 0 & 0 & 1 & 0 \\ 0 & 0 & 0 & 1 \end{bmatrix} = \begin{bmatrix} s6 & c6 & 0 & 0 \\ 0 & 0 & 1 & 0 \\ c6 & -s6 & 0 & L_7 \\ 0 & 0 & 0 & 1 \end{bmatrix} \tag{4.10} $$

$$ {}^{5}_{6}T = \begin{bmatrix} 0 & -1 & 0 & L_8 \\ 1 & 0 & 0 & 0 \\ 0 & 0 & 1 & 0 \\ 0 & 0 & 0 & 1 \end{bmatrix} \tag{4.11} $$

Meanwhile, the transform matrices from frame 1 to frame 3 via the parallel mechanism shown in Figure 4.5 can be written as following,

$$ {}^{1}_{7}T = \begin{bmatrix} c3 & -s3 & 0 & L_3 \\ 0 & 0 & -1 & 0 \\ s3 & c3 & 0 & L_2 \\ 0 & 0 & 0 & 1 \end{bmatrix} \tag{4.12} $$

$$ {}^{7}_{8}T = \begin{bmatrix} c5 & -s5 & 0 & L_5 \\ s5 & c5 & 0 & 0 \\ 0 & 0 & 1 & 0 \\ 0 & 0 & 0 & 1 \end{bmatrix} \tag{4.13} $$

$$ {}^{8}_{9}T = \begin{bmatrix} c4 & -s4 & 0 & L_4 \\ s4 & c4 & 0 & 0 \\ 0 & 0 & 1 & 0 \\ 0 & 0 & 0 & 1 \end{bmatrix} \tag{4.14} $$

$$ {}^{9}_{3}T = \begin{bmatrix} 1 & 0 & 0 & L_5 \\ 0 & 1 & 0 & 0 \\ 0 & 0 & 1 & 0 \\ 0 & 0 & 0 & 1 \end{bmatrix} \tag{4.15} $$

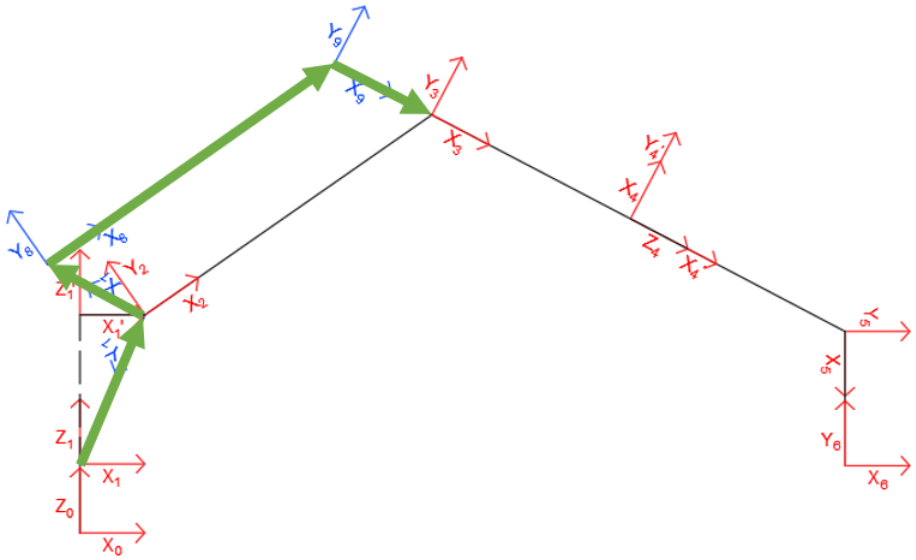

Figure 4.5: Schematic of the Transform Path from Frame 1 to Frame 3 via Parallel Mechanism

As a result, the forward kinematics for this 5-DOF robotic arm from base to the end effector is expressed as following,

$$ {}^{0}_{6}T = {}^{0}_{1}T\,{}^{1}_{2}T\,{}^{2}_{3}T\,{}^{3}_{4}T\,{}^{4}_{5}T\,{}^{5}_{6}T \tag{4.16} $$

Therefore, the transfer matrices can be calculated as following,

$$ {}^{0}_{5}T = \begin{bmatrix} -s_{246}c_1 & -c_{246}c_1 & s_1 & c_1(L_3 + L_4c_2 - L_6c_{24} - L_7c_{24} + L_8c_{246}) \\ -s_{246}s_1 & -c_{246}s_1 & -c_1 & s_1(L_3 + L_4c_2 - L_6c_{24} - L_7c_{24} + L_8c_{246}) \\ c_{246} & -s_{246} & 0 & L_1 + L_2 + L_4s_2 - L_6s_3 - L_7s_3 - L_8s_{246} \\ 0 & 0 & 0 & 1 \end{bmatrix} \tag{4.17} $$

Using the relationship between different joints, the equation is equivalent to the following,

$$ {}^{0}_{5}T = \begin{bmatrix} s_{36}c_1 & c_{36}c_1 & s_1 & c_1(L_3 + L_4c_2 - L_6c_3 - L_7c_3 + L_8c_{36}) \\ s_{36}s_1 & c_{36}s_1 & -c_1 & s_1(L_3 + L_4c_2 - L_6c_3 - L_7c_3 + L_8c_{36}) \\ -c_{36} & s_{36} & 0 & L_1 + L_2 + L_4s_2 - L_6s_3 - L_7s_3 - L_8s_{36} \\ 0 & 0 & 0 & 1 \end{bmatrix} \quad (4.18) $$

The forward kinematics can also be calculated via the parallel links, where the equation is as following,

$$ {}^{0}_{5}T' = {}^{0}_{1}T\,{}^{1}_{7}T\,{}^{7}_{8}T\,{}^{8}_{9}T\,{}^{9}_{3}T\,{}^{3}_{4}T\,{}^{4}_{5}T\,{}^{5}_{6}T \quad (4.19) $$

Same as before, when writing the transfer matrix in following format,

$$ {}^{0}_{5}T' = \begin{bmatrix} -s_{3456}c_1 & -c_{3456}c_1 & s_1 & c_1(L_3 + L_4c_2 + L_5c_3 + L_5c_{345} - L_6c_{345} - L_7c_{345} + L_8c_{3456}) \\ -s_{3456}s_1 & -c_{3456}s_1 & -c_1 & s_1(L_3 + L_4c_2 + L_5c_3 + L_5c_{345} - L_6c_{345} - L_7c_{345} + L_8c_{3456}) \\ -c_{36} & -s_{3456} & 0 & L_1 + L_2 + L_4s_2 + L_5c_3 + L_5c_{345} - L_6s_3 - L_7s_3 - L_8s_{3456} \\ 0 & 0 & 0 & 1 \end{bmatrix} \quad (4.20) $$

Due to the parallelism between link 7-8 and link 3-9, Θ_4 can be expressed in terms of Θ_2 and Θ_3. Similarly, Θ_6 is calculated from Θ_3, when the end effector is always facing down,

$$ \begin{cases} \Theta_4 = \Theta_3 - \Theta_2 + 180° \\ \Theta_5 = \Theta_2 - \Theta_3 \\ \Theta_6 = 90° - \Theta_3 \end{cases} \quad (4.21) $$

Then, rewriting the above equation 4.20 using equation 4.21 gives the same result as 4.18, and this verifies the calculation for parallel links is correct. The final position of the end effector is given as following,

$$ \begin{cases} x = c_1(L_3 + L_4c_2 - L_6c_3 - L_7c_3 + L_8c_{36}) \\ y = s_1(L_3 + L_4c_2 - L_6c_3 - L_7c_3 + L_8c_{36}) \\ \mathrm{z} = L_1 + L_2 + L_4s_2 - L_6s_3 - L_7s_3 - L_8s_{36} \end{cases} \quad (4.22) $$

When the end effector is facing down, the equation is simplified further. The sum of Θ_3 and Θ_6 shown in Figure 4.3 is 450°, so terms $c_{36} = 0$ and $s_{36} = 1$.

$$ \begin{cases} x = c_1(L_3 + L_4c_2 - L_6c_3 - L_7c_3) \\ y = s_1(L_3 + L_4c_2 - L_6c_3 - L_7c_3) \\ \mathrm{z} = L_1 + L_2 + L_4s_2 - L_6s_3 - L_7s_3 - L_8 \end{cases} \quad (4.23) $$

The inverse kinematics is achieved through the geometric approach. Basically, the location of the end effector is represented by joint angles and link lengths in 3 directions, X, Y, and Z, of a Cartesian coordinate system which is the '0' coordinate system in Figure 4.2. Through solving system of equations, the angle at each joint can be calculated. Assuming the goal point of the robotic arm is $[\mathrm{x\ y\ z}]^{\mathrm{T}}$, using dimensions in Figure 4.3 and Figure 4.4 generates the following equations,

$$\begin{cases} x = [L_3 + L_4 c2 - (L_6 + L_7)c3]c1 \\ y = [L_3 + L_4 c2 - (L_6 + L_7)c3]s1 \\ \mathrm{z} = L_1 + L_2 + L_4 s2 - (L_6 + L_7)s3 - L_8 \end{cases} \quad (4.24)$$

Considering the geometry, $L_4 c2 - (L_6 + L_7)$ is always greater than 0, where L_7 is a variable of the extended length of the prismatic joint. So,

$$\begin{cases} L_4 c2 - (L_6 + L_7)c3 = \sqrt{x^2 + y^2} - L_3 \\ L_4 s2 - (L_6 + L_7)s3 = z - L_1 - L_2 - L_8 \\ \Theta_1 = \arctan(y, x) \end{cases} \quad (4.25)$$

Due to the redundant design, there are more variables than equations. In the actual operation process, the length of the extension part shall be considered first, so it is possible to consider L_6+L_7 as a constant for further investigation. Then, let

$$\begin{cases} a = L_4 \\ b = (L_6 + L_7) \\ m = \sqrt{x^2 + y^2} - L_3 \\ n = z - L_1 - L_2 - L_8 \end{cases} \quad (4.26)$$

The set of equations are as following,

$$\begin{cases} a * c2 - b * c3 = m \\ a * s2 - b * s3 = n \end{cases} \quad (4.27)$$

The analytical solution is given by 4.21 and following equations,

$$\Theta_2 = 2 * \mathrm{atan}\left(\frac{2an \pm \sqrt{(-a^2 + 2ab - b^2 + m^2 + n^2) * (a^2 + 2ab + b^2 - m^2 - n^2)}}{a^2 + 2am - b^2 + m^2 + n^2}\right) \quad (4.28)$$

$$\Theta_3 = 2 * \mathrm{atan}\left(\frac{2bn \pm \sqrt{(-a^2 + 2ab - b^2 + m^2 + n^2) * (a^2 + 2ab + b^2 - m^2 - n^2)}}{a^2 - b^2 + 2bm - m^2 - n^2}\right) \quad (4.29)$$

4.2 Dynamics

The dynamics of this robotic arm is calculated through the iterative Newton-Euler dynamics algorithm [35]. This method calculates iteratively the relative kinematics and body forces to previous joints. As such, the absolute values corresponding to the base frame are determined for each joint through outward iterations. Then, the inward iterations are applied to the same manipulator for finding force and torque required at each joint. It calculates joint by joint from the end effector to the base frame. Thus, the force/Torque required at each joint is determined. The mathematical expressions for this method are described in equations 4.30 and equations 4.39. The outward iterations are as following,

Outward iteration i: 0-4

$$
\begin{aligned}
{}^{i+1}\omega_{i+1} &= {}^{i+1}_{i}R\ {}^{i}\omega_i + \dot{\theta}_{i+1}\,{}^{i+1}\hat{Z}_{i+1} \\
{}^{i+1}\dot{\omega}_{i+1} &= {}^{i+1}_{i}R\ {}^{i}\dot{\omega}_i + {}^{i+1}_{i}R\ {}^{i}\omega_i \times \dot{\theta}_{i+1}\,{}^{i+1}\hat{Z}_{i+1} + \ddot{\theta}_{i+1}\,{}^{i+1}\hat{Z}_{i+1} \\
{}^{i+1}\dot{v}_{i+1} &= {}^{i+1}_{i}R\left({}^{i}\dot{\omega}_i \times {}^{i}P_{i+1} + {}^{i}\omega_i \times \left({}^{i}\omega \times {}^{i}P_{i+1}\right) + {}^{i}\dot{v}_i\right) \\
{}^{i+1}\dot{v}_{C_{i+1}} &= {}^{i+1}\dot{\omega}_{i+1} \times {}^{i}P_{C\,i+1} + {}^{i+1}\omega_{i+1} \times \left({}^{i+1}\omega_{i+1} \times {}^{i}P_{C\,i+1}\right) + {}^{i+1}\dot{v}_{i+1} \\
{}^{i+1}F_{i+1} &= m_{i+1}\,{}^{i+1}\dot{v}_{C_{i+1}} \\
{}^{i+1}N_{i+1} &= {}^{C_{i+1}}I_{i+1}\,{}^{i+1}\dot{\omega}_{i+1} + {}^{i+1}\omega_{i+1} \times {}^{C_{i+1}}I_{i+1}\,{}^{i+1}\omega_{i+1}
\end{aligned}
\tag{4.30}
$$

where ω is the angular velocity of the joint; $\dot{\omega}$ is the angular acceleration of the joint; $\dot{v}$ is the acceleration of linear joint; $\dot{v}_c$ is the acceleration of the center of gravity; F is the force; N is the torque; R is the rotation matrix; P is the translation matrix; P_C is the translation matrix relate to the center of the body; m is mass; and, I is the mass moment of inertia. The outward iterations for link 1 are as following,

$$
{}^{1}\omega_1 = \dot{\theta}_1\,{}^{1}\hat{Z}_1 = \begin{bmatrix} 0 \\ 0 \\ \dot{\theta}_1 \end{bmatrix} \tag{4.31}
$$

$$
{}^{1}\dot{\omega}_1 = \ddot{\theta}_1\,{}^{1}\hat{Z}_1 = \begin{bmatrix} 0 \\ 0 \\ \ddot{\theta}_1 \end{bmatrix} \tag{4.32}
$$

$$
{}^{1}\dot{v}_1 = \begin{bmatrix} 0 \\ 0 \\ g \end{bmatrix} \tag{4.33}
$$

$$
{}^{1}\dot{v}_{C_1} = {}^{1}\dot{\omega}_1 \times {}^{i}P_{C\,i+1} + {}^{1}\omega_1 \times \left({}^{1}\omega_1 \times {}^{i}P_{C\,i+1}\right) + {}^{1}\dot{v}_1 = \begin{bmatrix} 0 \\ 0 \\ g \end{bmatrix} \tag{4.34}
$$

$$
{}^{1}F_1 = m_1\,{}^{1}\dot{v}_{C_1} = \begin{bmatrix} 0 \\ 0 \\ m_1 g \end{bmatrix} \tag{4.35}
$$

$$
{}^{1}N_1 = {}^{C_1}I_1\,{}^{1}\dot{\omega}_1 + {}^{1}\omega_1 \times {}^{C_1}I_1\,{}^{1}\omega_1 = \begin{bmatrix} I_{xx1} & I_{xy1} & I_{xz1} \\ I_{yx1} & I_{yy1} & I_{yz1} \\ I_{zx1} & I_{zy1} & I_{zz1} \end{bmatrix} \begin{bmatrix} 0 \\ 0 \\ \ddot{\theta}_1 \end{bmatrix} + \begin{bmatrix} 0 \\ 0 \\ \dot{\theta}_1 \end{bmatrix} \times \begin{bmatrix} I_{xx1} & I_{xy1} & I_{xz1} \\ I_{yx1} & I_{yy1} & I_{yz1} \\ I_{zx1} & I_{zy1} & I_{zz1} \end{bmatrix} \begin{bmatrix} 0 \\ 0 \\ \dot{\theta}_1 \end{bmatrix} \tag{4.36}
$$

$$
= \begin{bmatrix} I_{xz1}\ddot{\theta}_1 \\ I_{yz1}\ddot{\theta}_1 \\ I_{zz1}\ddot{\theta}_1 \end{bmatrix} + \begin{bmatrix} -I_{yz1}\dot{\theta}_1^2 \\ I_{xz1}\dot{\theta}_1^2 \\ 0 \end{bmatrix} = \begin{bmatrix} I_{xz1}\ddot{\theta}_1 - I_{yz1}\dot{\theta}_1^2 \\ I_{yz1}\ddot{\theta}_1 + I_{xz1}\dot{\theta}_1^2 \\ I_{zz1}\ddot{\theta}_1 \end{bmatrix} \tag{4.37}
$$

Same outward iterations can be performed for other links including prismatic joints and parallel links. Due to the parallel design and equation 4.21, the angular velocity and angular acceleration are expressed as following,

$$\begin{cases} \dot{\Theta}_4 = \dot{\Theta}_3 - \dot{\Theta}_2 \\ \dot{\Theta}_5 = \dot{\Theta}_2 - \dot{\Theta}_3 \\ \dot{\Theta}_6 = \dot{\Theta}_3 \end{cases} and \begin{cases} \ddot{\Theta}_4 = \ddot{\Theta}_3 - \ddot{\Theta}_2 \\ \ddot{\Theta}_5 = \ddot{\Theta}_2 - \ddot{\Theta}_3 \\ \ddot{\Theta}_6 = \ddot{\Theta}_3 \end{cases} \quad (4.38)$$

After outward iterations, inward iterations are applied to the arm to determine the feedback force and torque. Equations for this process are,

$$\begin{gathered} {}^{i}f_i = {}_{i+1}^{i}R\,{}^{i+1}f_{i+1} + {}^{i}F_i \\ {}^{i}n_i = {}^{i}N_i + {}_{i+1}^{i}R\;{}^{i+1}n_{i+1} + {}^{i}P_{C_i} \times {}^{i}F_i + {}^{i}P_{i+1} \times {}_{i+1}^{i}R\;{}^{i+1}f_{i+1} \\ \tau_i = {}^{i}n_i^T\,{}^{i}\hat{Z}_i \end{gathered} \quad (4.39)$$

where i is from 5 to 1; *f* is the force required at the joint; n is the torque required at the joint.

The free body diagram for this part is shown in Figure 4.6. In the diagram, ${}^{9}f_9$ is the force required at the joint 9; ${}^{9}n_9$ is the torque required at the joint 9; ${}^{8}f_8$ is the force required at the joint 8; ${}^{8}n_8$ is the torque required at the joint 8; ${}^{8}F_8$ *is* the body force from link 8-9; and, ${}^{8}N_8$ *is* the total torque in link 8-9. For link 8-9 at joint 8, the equilibrium of force and equilibrium of momentum are,

$${}^{8}f_8 = {}_{9}^{8}R\,{}^{9}f_9 + {}^{8}F_8 \quad (4.40)$$

$${}^{8}n_8 = {}^{8}N_8 + {}_{9}^{8}R\,{}^{9}n_9 + {}^{8}P_{C_8} \times {}^{8}F_8 + {}^{8}P_9 \times {}_{9}^{8}R\,{}^{9}f_9 \quad (4.41)$$

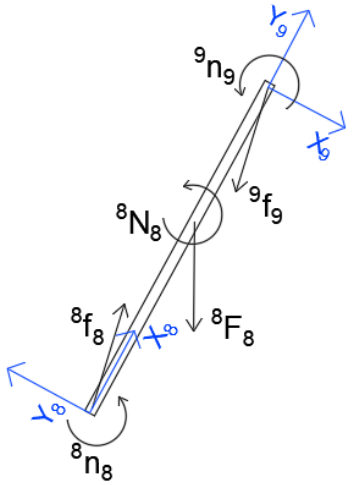

Figure 4.6: Free Body Diagram of the Parallel Link 8-9

Due pin connected link 8-9 is symmetric, ${}^{8}n_8$ and ${}^{9}n_9$ are 0. Also, the gravity center is at the geometry center. Thus, the equilibrium of momentum equation above is simplified as,

$$0 = {}^{8}N_8 + {}^{8}P_{C_8} \times {}^{8}F_8 + {}^{8}P_9 \times {}^{8}_{9}R\,{}^{9}f_9 \tag{4.42}$$

Since the parallel section, link 8-9, has 3 joints, the inward iteration equation is inappropriate for these joints. To analyze link 9-4 at joint 3, a free body diagram is shown as following Figure 4.7,

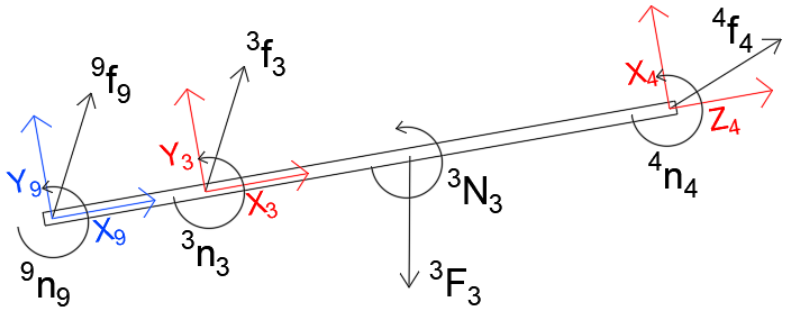

Figure 4.7: Free Body Diagram of the Link 9-4

The equilibrium of forces gives

$${}^{3}f_3 + {}^{3}f_9 - {}^{3}f_4 - {}^{3}F_3 = 0 \tag{4.43}$$

and equilibrium of moment gives,

$${}^{3}n_3 + {}^{3}n_9 = {}^{3}N_3 + {}^{3}n_4 + {}^{3}P_4 \times {}^{3}f_4 - {}^{3}P_9 \times {}^{3}f_9 + {}^{3}P_{c3} \times {}^{3}F_3 = 0 \tag{4.44}$$

where, ${}^{9}n_9$ is 0 when joint 3 is assumed to be rigid and joint 9 is a pin connection. ${}^{3}n_3$ is 0 in z-direction for pin connection. Thus,

$${}^{3}n_3 + {}^{3}P_9 \times {}^{3}_{9}R\,{}^{9}f_9 = {}^{3}N_3 + {}^{3}_{4}R\,{}^{4}n_4 + {}^{3}P_{c3} \times {}^{3}F_3 + {}^{3}P_4 \times {}^{3}_{4}R\,{}^{4}f_4 \tag{4.45}$$

and from D-H parameters,

$${}^{9}_{3}T = \begin{bmatrix} 1 & 0 & 0 & L_5 \\ 0 & 1 & 0 & 0 \\ 0 & 0 & 1 & 0 \\ 0 & 0 & 0 & 1 \end{bmatrix} \tag{4.46}$$

$${}^{3}_{9}R = \begin{bmatrix} 1 & 0 & 0 \\ 0 & 1 & 0 \\ 0 & 0 & 1 \end{bmatrix}, and\ {}^{3}P_9 = \begin{bmatrix} L_5 \\ 0 \\ 0 \end{bmatrix} \tag{4.47}$$

$${}^{3}P_9 \times {}^{3}_{9}R\,{}^{9}f_9 = \begin{bmatrix} -L_5 \\ 0 \\ 0 \end{bmatrix} \times \begin{bmatrix} F_x \\ F_y \\ 0 \end{bmatrix} = \begin{bmatrix} 0 \\ 0 \\ -L_5 F_y \end{bmatrix} \tag{4.48}$$

Since the pin connection at joint 9, ${}^{9}f_9 = \begin{bmatrix} F_x \\ F_y \\ 0 \end{bmatrix}$, the equilibrium equations give

$$ {}^{3}f_3 + \begin{bmatrix} F_x \\ F_y \\ 0 \end{bmatrix} = {}^{3}_{4}R\, {}^{4}f_4 + {}^{3}F_3 \tag{4.49} $$

$$ {}^{3}n_3 + \begin{bmatrix} 0 \\ 0 \\ -L_5 F_y \end{bmatrix} = {}^{3}N_3 + {}^{3}_{4}R\, {}^{4}n_4 + {}^{3}P_{c3} \times {}^{3}F_3 + {}^{3}P_4 \times {}^{3}_{4}R\, {}^{4}f_4 \tag{4.50} $$

So, the solve equation in for z component, there is

$$ F_y = -\frac{({}^{3}N_3 + {}^{3}_{4}R\, {}^{4}n_4 + {}^{3}P_{c3} \times {}^{3}F_3 + {}^{3}P_4 \times {}^{3}_{4}R\, {}^{4}f_4)\, {}^{i}\hat{Z}_i}{L_5} \tag{4.51} $$

and, combined with 4.42, there is

$$ {}^{8}P_9 \times {}^{8}_{9}R\, {}^{9}f_9 = L_4 \begin{bmatrix} 0 \\ 0 \\ c4F_y + s4F_x \end{bmatrix} = -{}^{8}N_8 - {}^{8}P_{C_8} \times {}^{8}F_8 \tag{4.52} $$

$$ F_x = -\frac{\left({}^{8}N_8 + {}^{8}P_{C_8} \times {}^{8}F_8\right) {}^{i}\hat{Z}_i}{s4L_4} - \frac{c4}{s4} F_y \tag{4.53} $$

Therefore, the overall reaction force at the joint 9 is given as

$$ {}^{9}f_9 = \begin{bmatrix} -\frac{\left(-{}^{8}N_8 - {}^{8}P_{C_8} \times {}^{8}F_8\right) {}^{i}\hat{Z}_i}{s4L_4} - \frac{c4}{s4} F_y \\ -\frac{({}^{3}N_3 + {}^{3}_{4}R\, {}^{4}n_4 + {}^{3}P_{c3} \times {}^{3}F_3 + {}^{3}P_4 \times {}^{3}_{4}R\, {}^{4}f_4)\, {}^{i}\hat{Z}_i}{L_5} \\ 0 \end{bmatrix} \tag{4.54} $$

For joint 2 and joint 7, the force and torque requirements are also derived from inward iterations using equations 4.39. At joint 1, the total force is the sum of both parts of the parallel links, and, same as the torque calculations. Then,

$$ {}^{1}f_1 = {}^{1}_{2}R\, {}^{2}f_2 + {}^{1}_{7}R\, {}^{7}f_7 + {}^{1}F_1 \tag{4.55} $$

$$ {}^{1}n_1 = {}^{1}N_2 + {}^{1}N_7 + {}^{1}_{2}R\, {}^{2}n_2 + {}^{1}_{7}R\, {}^{7}n_7 + {}^{1}P_{C_1} \times {}^{1}F_1 + {}^{1}P_2 \times {}^{1}_{2}R\, {}^{2}f_2 + {}^{1}P_7 \times {}^{1}_{7}R\, {}^{7}f_7 \tag{4.56} $$

With the above equations, the force and torque requirements for each joint are calculated. The complete equations are derived through MATLAB with symbolic toolbox. Due to the complexity and limited space, the detailed symbolic solution is omitted. Instead, the following section shows kinematics and dynamics analysis with a number from a proposed mechanical design with actual physical properties were obtained from a SolidWorks Model.

4.3 Verification of the Analysis through Simulations

To verify the accuracy of kinematics and dynamics analysis, it typically requires testing a robotic arm with the proposed structure and accurately controlling the joint movement while measuring the force and torque at each joint. However, physically constructing the robotic arm is expensive and time-consuming. Instead, the simulation method is applied to test and verify theoretically derived dynamics expressions. A 5-DOF robotic arm model with the proposed structure is constructed initially, and its components are transferred into SIMULINK with defined relationships. The reactions at each joint are calculated by the software when angles of rotation are input into the system.

A robotic arm model is built first before performing numerical analysis and simulation. Based on the requirements of collecting data in the same fields where the 1st and 2nd generation boom were tested, this arm has a maximum of 2.5 m reach to cover 6 m wide plots and undertakes a maximum of 10 kg payload at 2.5 m distance. The structure, component, and size of this arm are optimized with FEA, so the structure does not fail or deflect too much during the operation. The proposed robotic arm has major physical properties as following,

$L_1 = 0.1\,m$
$L_2 = 0.15\,m$
$L_3 = 0.025\,m$
$L_4 = 1\,m$
$L_5 = 0.2\,m$
$L_7 = 1.0\,m$
$L_8 = 0.05\,m$
$m_1 = 10.84\,kg$
$m_2 = 13.2\,kg$
$m_3 = 15\,kg$
$m_4 = 14.07\,kg$
$m_5 = 3.7\,kg$
$I_0 = [0.035100\ 0\ 0;\ 0\ \ 0.035244\ 0;\ 0\ 0\ 0.066867]\,kg * m^2$

$I_1 = [0.107209\ -0.000470\ 0.002665;\ -0.000470\ \ 0.104277\ -0.000897;\ 0.002665\ -0.000897\ 0.079165]\ kg * m^2$

$I_2 = [0.02844284\ 0\ 0;\ 0\ \ 4.65136350\ 0;\ 0\ 0\ 4.63702358]\ kg * m^2$

$I_3 = [\ 0.023255\ \ 0.150032\ 0;\ \ 0.150032\ \ 3.870636\ 0;\ 0\ 0\ \ 3.879762]\ \ kg * m^2$

$I_4 = [5.091832\ 0\ 0.093505;\ 0\ 5.065538\ 0;\ 0.093505\ 0\ 0.049158]\ kg * m^2$

$I_5 = [0.049503\ -0.003261\ 0\ -0.003261;\ \ 0.073610\ 0\ 0;\ 0\ 0.027510]\ kg * m^2$

$P_{C0} = [0\ 0\ \ 0.010448]\ m$

$P_{C1} = [0.002644\ -0.000788\ 0.047891]\ m$

$P_{C2} = [\ 0.50161833\ \ 0\ 0]\ m$

$P_{C3} = [0.334742\ 0.027056\ 0]\ m$

$P_{C4} = [0\ 0.014022\ 0\ 0.581606]\ m$

$P_{C5} = [0.074812\ -0.010134\ 0]\ m$

Figure 4.8: Schematic of the Proposed 3rd Generation Boom for Plant Phenotyping.

The workspace of this robotic arm is derived to find the proper operating range. Considering the physical limitation of each link, such as preventing collision and actuator traveling distance, constrains of each joint are listed in Table 4.2. Then, forward kinematics is applied to identify the workspace under such angle restrains. As a result, Figure 4.9 provides detailed dimension of the cross-section of the workspace of this robotic arm. The boarder of the workspace is shown in color blue, and the arm can reach all points inside yellow region. Since the base of this robotic arm rotates 360°, rotating this cross-section about vertical axis provides the whole workspace shown in Figure 4.10. However, when implementing multiple robotics arms at the same

platform, the workspace for each robotic arm can be slightly altered. Instead, they can be constrained in the software to avoid collision between robotic arms.

Table 4.2: Constrains of each Joint

Joint	Constrains
1	$0 \leq \Theta_1 \leq 360°$
2	$0 \leq \Theta_2 \leq 120°$
3	$\Theta_2 \leq \Theta_3 \leq 180°$
4	$0 \leq L_7 \leq 1$ m
5	$-90° \leq \Theta_6 \leq 90°$

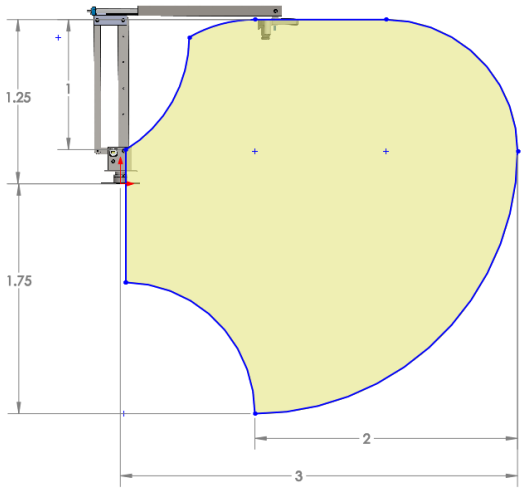

Figure 4.9: Demonstration of the Cross-section of the Workspace of the robotic

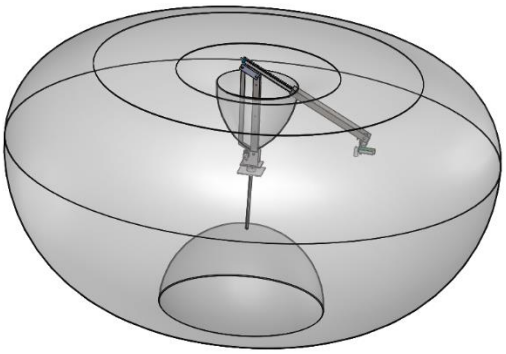

Figure 4.10: Demonstration of the Workspace of the robotic arm in 3D

To verify kinematics and dynamics results, a SIMULINK model shown in Figure 4.11 is built in MATLAB. Each block is corresponding to one section of the robotic arm which contains the physical properties, such as mass and mass moment of inertia, which are calculated by the program automatically. The Simscape toolbox is then applied to define the relative location and orientation between two adjacent components. The final constructed 3D model of this arm is

shown in Figure 4.12. The details of this model are demonstrated in Appendix E: SIMULINK Model of the Robotic Arm. To inspect the performance, rotation/linear motions are defined by an input signal to each specified joint, so this simulated arm has the same kinematic and dynamics properties like the one described in the theoretical analysis.

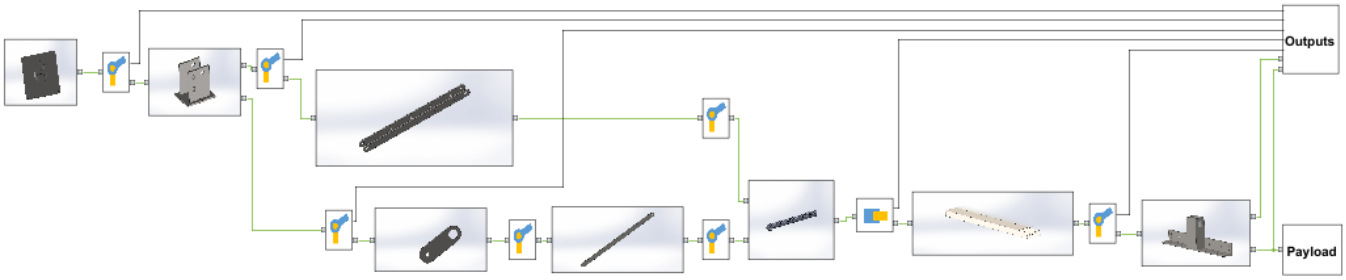

Figure 4.11: SIMULINK Model of the Robotic Arm

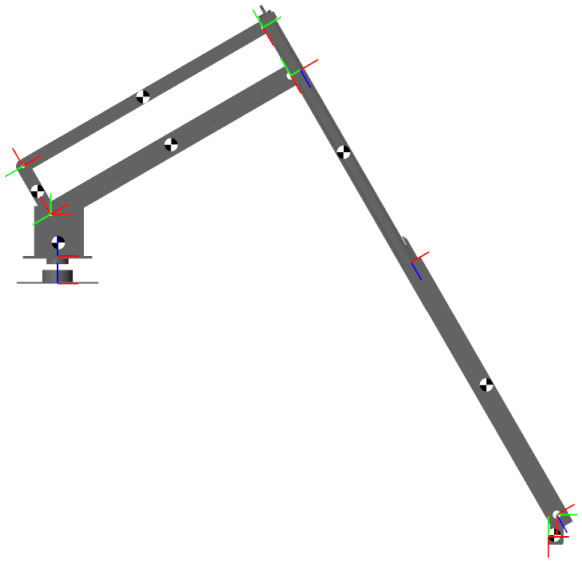

Figure 4.12: Constructed Model of the Robotic Arm in Simulation

Simulation results are compared to the iterative Newton-Euler method to find the difference between the two approaches. For kinematics analysis, positions of the effector from both methods are matched with each other. The torque and force requirements for each joint at selected angles are demonstrated in Table 4.3 when the robot arm is stationary. For example, the 2nd row shows calculated torque and force at each joint when $\theta_1 = 0°$, $\theta_2 = 30°$, $\theta_3 = 120°$, $L_6 = .6$ m, $\theta_4 = 180°$, $\theta_5 = 90°$, and $\theta_6 = -30°$, are assigned to the corresponding joints where joint 4 to 6 are calculated from equation 4.21, and the velocity, acceleration, angular velocity, and angular acceleration are 0. The same joint angles are assigned to the simulation model to

estimate the reaction force and torque. Simulated results are demonstrated in Table 4.4. Even though both tables show identical values for same input angles after rounding up, they are not the same after several decimal places. The reason is from the modeling and round up in the model.

Table 4.3: Force/Torque Required at Each Joint from Newton Euler Methods

Joint Angles of $[\theta_1 \ \theta_2 \ \theta_3]$	Revolute Joint 1 (N-m)	Revolute Joint 2 (N-m)	Revolute Joint 3 (N-m)	Prismatic Joint (N)	Revolute Joint 5 (N-m)
[0 30 120]	0	347	132	-151	-0.37
[0 30 140]	0	347	199	-112	-0.37
[0 60 120]	0	200	132	-151	-0.37
[0 90 180]	0	0	255	0	-0.37

Table 4.4: Force/Torque Required at Each Joint from MATLAB Simulation

Joint Angles of $[\theta_1 \ \theta_2 \ \theta_3]$	Revolute Joint 1 (N-m)	Revolute Joint 2 (N-m)	Revolute Joint 3 (N-m)	Prismatic Joint (N)	Revolute Joint 5 (N-m)
[0 30 120]	0	347	132	-151	-0.37
[0 30 140]	0	347	199	-112	-0.37
[0 60 120]	0	200	132	-151	-0.37
[0 90 180]	0	0	255	0	-0.37

Comparing Table 4.3 and Table 4.4, it also shows that analytical and numerical solutions provide the same results for the same orientation of the robotic arm in the static situation. Both results show that joint 2 and 3 are independent to each other, and they are only related to the angle of rotation at the corresponding joint. The torque required at joint 2 decreases when the angle increases from 0 to 90 degrees is observed because the lever arm is becoming shorter for the vertical gravitational load. Meanwhile, the torque at joint 3 increases when the angle changes from 90 to 180 degrees. Since the end effector is always facing to the ground, the torque at joint 5 which is only related to the payload which should not change. The results in Table 4.4 also verify this. Thus, the analytical solution matches with the simulation results for the static case.

To further compare the dynamic performance, torque and force requirements are calculated when the arm is rotating. In this case, there are a few assumptions for operating conditions to make it more realistic to the actual condition. Assuming the height of the vehicle is 1.2 m high, and a fully matured canola crop is 1.4 m tall. The data are taken at two similar locations, A and B shown in Figure 4.13, which are 1 m and 2.5 m from the base of the arm. When sensors are placed 0.2 m from the crop for best measurements, the corresponding location of end effector in the global Cartesian system with $[X_0, Y_0, Z_0]$, is [1, 0, 0.4] and [2.5, 0, 0.4] for position A and B. Since the arm has a redundant DOF, the prismatic joint is fixed to a total length of 1.6 m. Using

inverse kinematics equation 4.27, the initial values for revolute joint 1, 2, 3, and 5 are calculated as (0°, 118.21°, 154.8°, 244.8°), and final values are (0°, 26.59°, 171.1°, 261.1°) in joint space. In the planned movement, all joints rotate simultaneously for 10 s where the initial and final speeds are 0. The angular velocity of each joint is expressed as following,

$$\omega = \frac{\pi}{2t_{end}}(\theta_{\text{end}} - \theta_{\text{ini}}) * \sin(\frac{\pi}{t_{end}}t) \tag{4.57}$$

Where t is time; t_{end} is total moving duration; θ_{ini} is the initial location; and, θ_{end} is the final rotate angle. Theoretically, the angle of rotation and angular acceleration are

$$\theta = -\frac{(\theta_{\text{end}} - \theta_{\text{ini}})}{2} * \cos\left(\frac{\pi}{t_{end}}t\right) + \frac{(\theta_{\text{end}} + \theta_{\text{ini}})}{2} \tag{4.58}$$

$$\dot{\omega} = \frac{\pi^2}{2t_{end}^2}(\theta_{\text{end}} - \theta_{\text{ini}}) * \cos\left(\frac{\pi}{t_{end}}t\right) \tag{4.59}$$

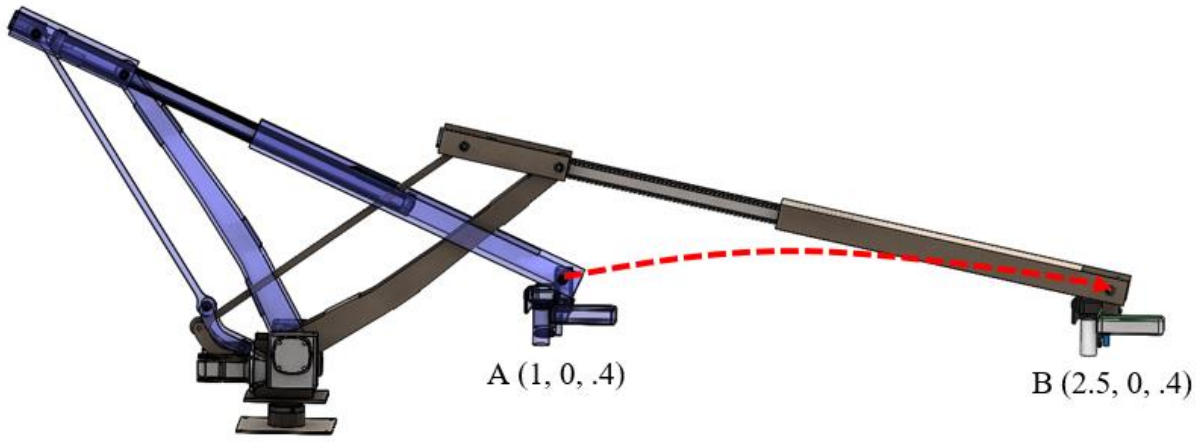

Figure 4.13: Demonstration of Path Planning from 1 m Reach to 2.5 m Reach

Meanwhile, the input of the SIMULINK model is a position which has the same expression as equation 4.58, but angular velocity and acceleration are calculated numerically from the model in Figure 4.11 with the solver ode45.

Results from two methods are also compared to find the difference. When there is no payload, the trajectory of the tip of the manipulator is shown in Figure 4.14. It shows that both theoretical and simulation results have the same trajectory. Figure 4.14 also reveals the reaction force or torque for each joint when the whole robotic arm is rotating. Comparing results from both methods, simulation ones are close to those from theory; however, there are some differences for joint 2, joint 3, and linear actuator part where the maximum difference is about 1%. When there

is 100 N payload, the trajectory of the tip of the manipulator is shown in Figure 4.15. This trajectory is the same as the one with no payload. In Figure 4.15, reaction force or torque are found like that without payload, but joint 2, joint 3, and linear actuator are experiencing a larger reaction force/torque.

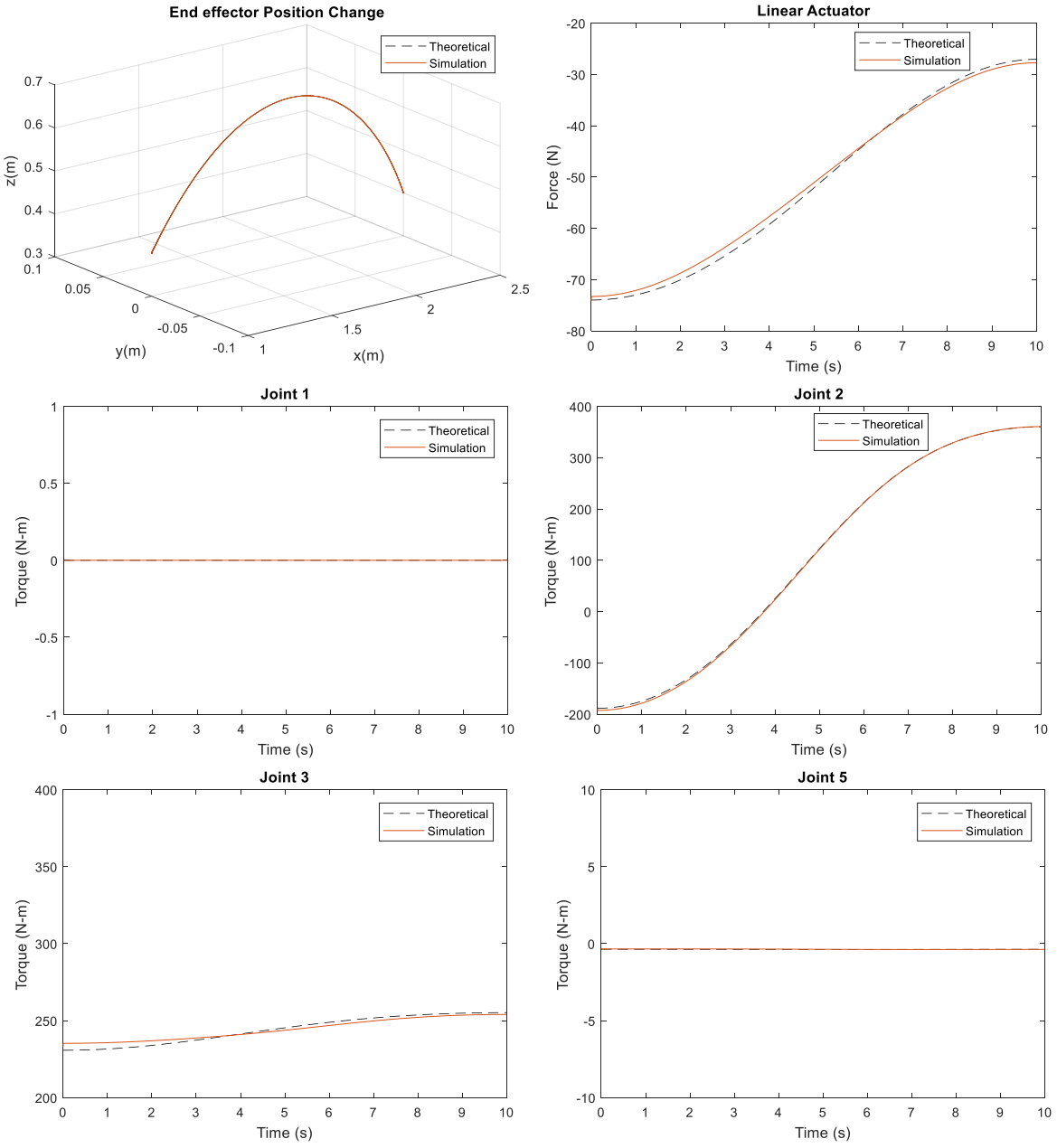

Figure 4.14:Comparison Between Theoretical and Simulation Results with no Payload (Top-left, trajectory of the end effector; Top-right, reaction force at the linear joint; Middle-left, torque requirement at the joint 1;Middle-left, torque requirement at the joint 2; Bottom-left, torque requirement at the joint 3; Bottom-right, torque requirement at the joint 4)

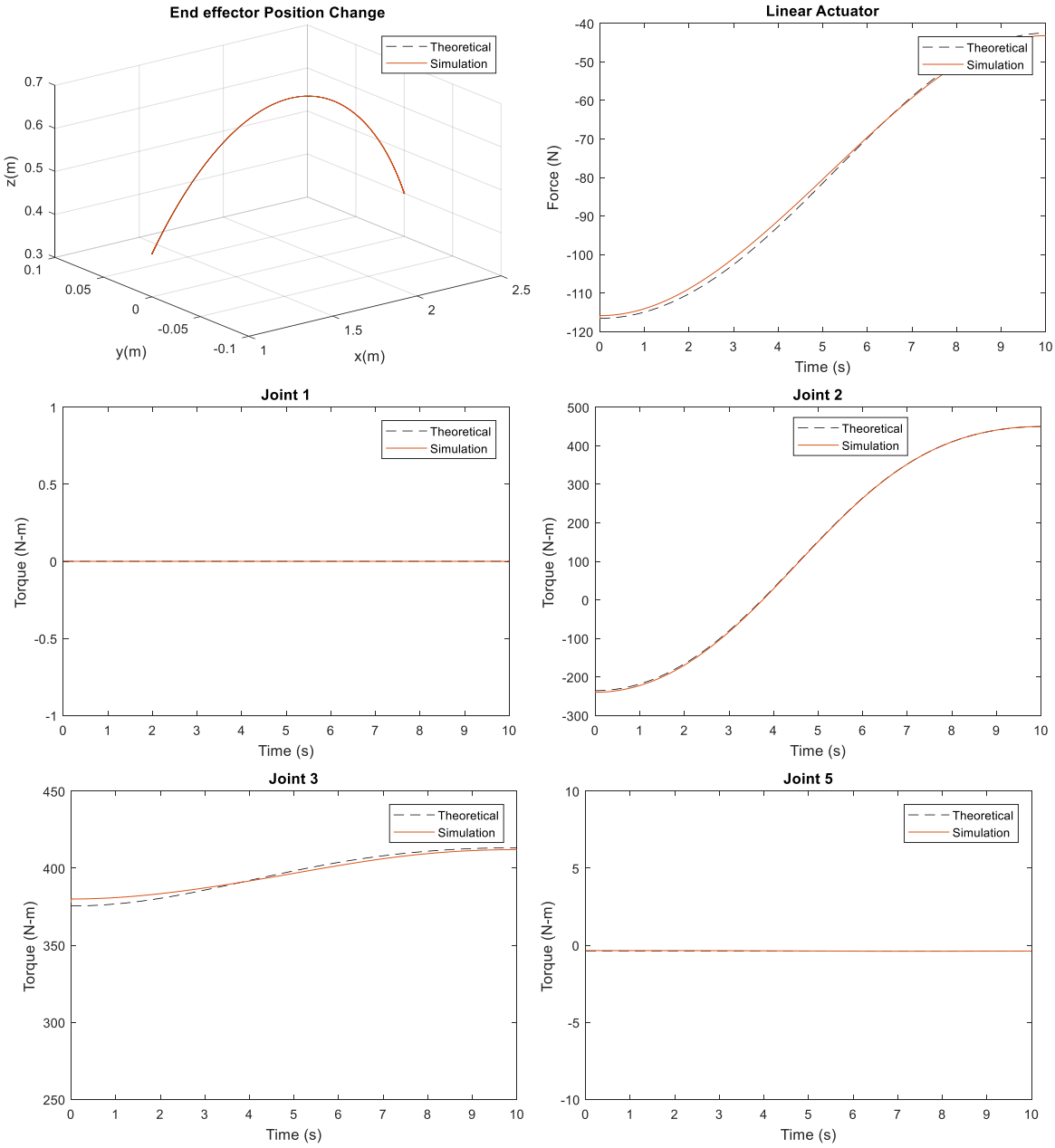

Figure 4.15: Comparison Between Theoretical and Simulation Results with 100 N Payload (Top-left, trajectory of the end effector; Top-right, reaction force at the linear joint; Middle-left, torque requirement at the joint 1;Middle-left, torque requirement at the joint 2; Bottom-left, torque requirement at the joint 3; Bottom-right, torque requirement at the joint 4)

There are few factors contribute to the difference between two models. First, the Newton-Euler method provides the exact solution at each moment when velocity and acceleration are calculated directly from the position expression; however, SIMULINK model calculated the velocity, acceleration, and reactions numerically. There is an accumulated round-off error during the time. Second, the SIMULINK model constructs the equations automatically, so the assumptions for the parallel link Section can be a slight difference. Finally, the properties of

links are found through SolidWorks and imported into the MATLAB code manually while SIMULINK model calculated it directly from the 3D model, so there is some round off error.

4.4 Verification of the Kinematics on Similar Robotic Arm

The forward and inverse kinematics are further verified on a 4 DOF robotic arm experimentally by comparing the calculated end effector position from assigned rotation angle to the actual movements. Shown in Figure 4.16, the tested parallel robotic arm (dimensions as labeled) can be considered as a simplified version of the 3rd generation boom. Since this simplified arm does not involve a linear actuator, it has one less degree of freedom. It should be noticed that the end effector of this manipulator is always facing down due to the parallel links connected to the end effector. In order to control the movement, the arm is programmed through the open source software, Arduino 1.8.5, which programs the controller, an Arduino UNO R3.0 board, to control servomotors' angle of rotation and speed. Since these servomotors have built-in potentiometers that measure the actual angle of rotation, the rotations of joints are controlled considerably accurately with such closed-loop control.

Figure 4.16: Robotic Arm for Verifying the Kinematics

Comparing to the proposed robotic arm, the corresponding dimensions of this arm are listed in Table 4.5. Besides, the horizontal distance from the last joint to the gripper is 25 mm when the vertical distance is 40 mm, so the position matrix for end effector is $[25\ -40\ 0\ 1]^T$. Therefore, the forward kinematics for this parallel robotic arm in Equation 4.18 is simplified to 4.57.

$$ {}^{0}_{5}T = \begin{bmatrix} s_{36}c_1 & c_{36}c_1 & s_1 & c_1(L_4c_2 - L_6c_3) \\ s_{36}s_1 & c_{36}s_1 & -c_1 & s_1(L_4c_2 - L_6c_3) \\ -c_{36} & s_{36} & 0 & L_1 + L_2 + L_4s_2 - L_6s_3 \\ 0 & 0 & 0 & 1 \end{bmatrix} \tag{4.60} $$

The end effector location in the global coordinate system is calculated as following

$$ P = {}^{0}_{5}T \cdot P_{eff} = \begin{bmatrix} 25s_{36}c_1 - 40c_{36}c_1 + c_1(L_4c_2 - L_6c_3) \\ 25s_{36}s_1 - 40c_{36}s_1 + s_1(L_4c_2 - L_6c_3) \\ -25c_{36} - 40s_{36} + L_1 + L_2 + L_4s_2 - L_6s_3 \\ 1 \end{bmatrix} \begin{bmatrix} 25 \\ -40 \\ 0 \\ 1 \end{bmatrix} \tag{4.61} $$

Table 4.5: Physical Dimensions of the Parallel Robotic Arm (Figure 4.4)

Link	Length (mm)
L_1	45
L_2	60
L_3	0
L_4	140
L_5	50
L_6	152
L_7	0
L_8	0

The robotic arm is tested to verify the forward kinematic method. First, different angles, are selected for each joint. In this case, Θ_1, Θ_2, and Θ_3 refer to the rotation of the base joint, lower arm and parallel arm separately, which is the same as angles demonstrated in Figure 4.3. Then, the end effector position is calculated with these angles through equation 4.58. Meanwhile, these angles are input into the program that controls the robotic arm, and the robotic arm is moved. When the arm stops, the distance from the end effector to the base of the arm is measured and recorded in a Cartesian system in Figure 4.2. Finally, measured results are compared with the calculated results. For example, Figure 4.17 demonstrates one of the sample measurements along x-axis when the input angle is $\Theta_1 = 0°$, $\Theta_2 = 30°$, and $\Theta_3 = 150°$, and the measurement is 290 mm in x direction. Some of the test results are demonstrated in Table 4.6 including input angles along with theoretical results and experimental measurements. Overall, theoretical and experimental results have good constancy where the average difference is less than 2%. Considering the limited accuracy of the servomotors and inadequate quality of the robotic arm, these results are

acceptable. Therefore, experiments verified the correctness of the derived forward kinematics equation.

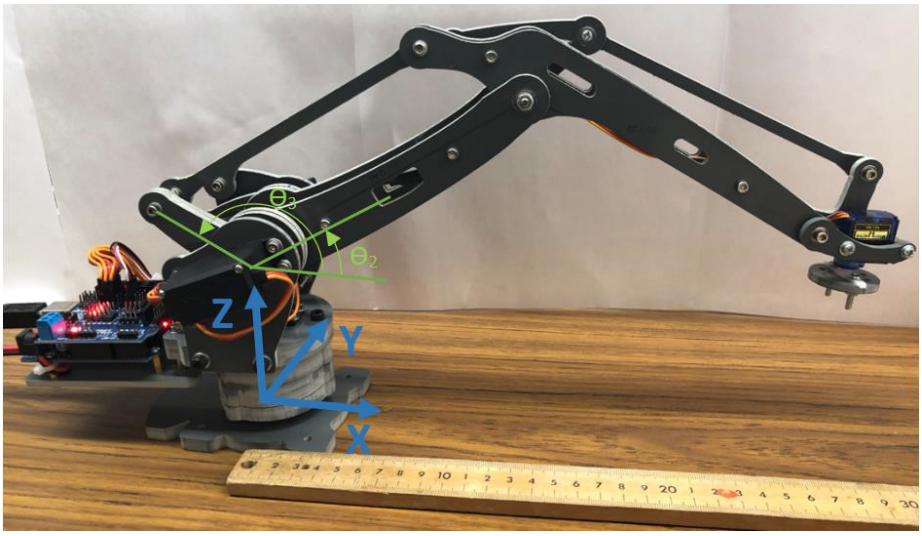

Figure 4.17: Sample Measure of the Robotic Arm reach (4-DOF Parallel Robotic Arm)

Table 4.6: Theoretical vs Experiment Results

Input angle (degrees) Θ_1	Θ_2	Θ_3	Theoretical Location (mm)	Experimental Location (mm)
0	0	90	[165 0 -87]	[165 0 -88]
0	0	150	[297 0 -11]	[302 0 -10]
0	45	135	[231 0 57]	[233 0 54]
0	90	135	[132 0 98]	[137 0 99]
0	90	150	[157 0 129]	[160 0 131]
0	90	180	[177 0 205]	[176 0 206]
90	90	180	[0 177 205]	[0 176 206]

The inverse kinematics is verified through the same robotic arm. Using values in Table 4.5, the equations 4.27 for inverse kinematics are simplified as following.

$$\begin{cases} 140 * c2 - 152 * c3 = \sqrt{(x-25)^2 + y^2} \\ 140 * s2 - 152 * s3 = z - 65 \end{cases} \quad (4.62)$$

The verification is performed as follows. First, the locations of the end effector are selected. Then, parameters in the above equation are substituted by the position value, and rotation angles are calculated. At the meantime, the end effector is moved to the desired position, and the angle of each joint is measured manually with a protractor. Finally, both results are compared to find the difference between theoretical analysis and experimental results. Some results are listed in Table 4.7. It indicates that experimental measurements are very close to theoretical results.

Therefore, the derived inverse kinematics equations of the 3rd generation robotic arm are valid for the similar parallel robotic arm.

Table 4.7: Inverse Kinematics Theoretical vs Experiment results

Desired Location (mm)	Theoretical (degrees)			Experimental (degrees)		
	Θ_1	Θ_2	Θ_3	Θ_1	Θ_2	Θ_3
[300 0 0]	0	2	153	0	4	155
[200 0 100]	0	67	142	0	67	157
[100 100 100]	45	84	137	48	84	140

4.5 Summary

This chapter discussed the kinematics, dynamics, and workspace of the 3rd boom/robotic arm that is proposed for phenotyping. Initially, the D-H parameters were found to calculate transform matrices and applied for deriving forward kinematics, inverse kinematics, and workspace. Next, the Newton-Euler iterative method was modified for deriving the dynamics of the robotic arm. Moreover, a simulation model was constructed in the SIMULINK to demonstrate the performance of this robotic arm. By comparing results from theoretical method and simulation for a sample path planning, it showed they were matched with each other. Finally, the kinematics equations were verified on a similar robot of the 3rd generation arm.

Chapter 5 Conclusion and Future Work

To solve food security concerns, HTP platforms were demanded for collecting crop traits in large scale to discover the relationship between phenotypes and genotypes. This study was part of the P^2IRC Project 2.2 which focused on field-based HTP mobile systems for crop monitoring. By developing a new robotic platform in this project, it improved monitoring crop health by collecting crop traits, such as height, temperature, color, and photos. Moreover, results from this project would facilitate understanding of the relationship between genotypes and phenotypes, selecting crops with stronger genes, increasing the yield, and solving food security problems. However, developing a new robotic HTP platform involved a large amount of efforts in building mechanical structure and electrical system. My primary role in this project was to design and evaluate the mechanical structure, especially, the phenotyping boom/ robotic arm. In this thesis, the discoveries of developing mechanical structures of a wheeled mobile platform for HTP of canola and wheat were discussed. These findings solved shortcomings from previous research, such as limited capability, field accessibility, or data collection speed, and helped to achieve autonomous data collection scope with higher accuracy and faster operating speed in the future.

This study developed three types of general-purpose mechanical structures. These platforms were 1st generation fixed C-channel boom, 2nd generation foldable C-channel boom, and the 3rd generation a 5-DOF robotic arm. Initially, the 1st generation phenotyping boom using C-channel was developed for measuring crop traits of canola plots. The major component of this boom was a 6 m long C-channel beam acting as a bridge connecting sensors and a farm vehicle. To enhance both transportability and accessibility, the boom was redesigned and a 2nd generation boom was developed; this happened by dividing the main C-channel into 3 pieces and equipped with electric powered winches for folding purpose and adjusting mechanism for better sensor performance. The 2nd generation boom was a universal platform that worked with two different vehicles, a 6-ft tractor and a Zürn swather; however, this boom can easily be used with other farm tractors. Besides, the developed booms were foldable, transportable, and adjustable for various sensors. Finally, to have more flexible operation for the phenotyping platform in the farm field, a 5-DOF hybrid robotic arm for phenotyping was proposed and analyzed. The arm had a long reach with relatively high payload to carry desired phenotyping equipment.

Different analyses were applied to understand the performance of these platforms. For 1st and 2nd generation booms, FEA was applied to analyze vibrations, stresses, and deformations of different booms. Besides, vibration tests were performed on both types of the booms to quantify the factors influencing vibration magnitude. Since most delicate sensors were sensitive to vibrations, it was necessary to discover how vibrations affected the performance of sensors and how they were induced. Vibration test equipment was tested and studied in a laboratory setting, and it was attached to different booms and vehicles to monitor vibration frequencies and patents. After data collection, measurements were further processed and through FFT and FEA approaches. The results showed that the vibration amplitude and frequency were influenced by several factors, including the type of vehicle, operating speed, road condition, and sensor location. In general, to have better operating performance, a larger vehicle with slower operating speed would be recommended. Meanwhile, a paved road or proper surface treatment to the unpaved road was preferred to have a more uniformed vibration and smaller vibration amplitude. Sensors that were sensitive to vibrations should be placed closer to the center of the boom. With a good combination of these considerations, the boom's vibration transmitted to sensors was significantly reduced such that measurements were reliable when compared with manual measurements. For 3rd generation robotic arm, it was theoretically analyzed for kinematics and dynamics. Meanwhile, a model was constructed in MATLAB to verify the performance of this arm both statically and dynamically. Moreover, the derived forward and backward equations were compared and verified by testing a similar parallel robotic arm.

For future works, more research shall be conducted in improving and verifying the existing structure and the proposed robotic arm. First, the structure of the 2nd generation booms can be improved. To have a better leveling capability, the wrenches can be replaced by hydraulics, so it is safer during folding operation and can be better leveled against tilt during the data collection. Besides, during the transportation, the 2nd generation boom experiences large vibration due to the cantilever structure. To solve this issue, the vibration of the boom can be measured while the vehicle is traveling, and results will help redesign the connection between the vehicle and boom. Second, the FEA model for the 2nd generation boom can be refined to include tensioned cables and sensors; and, on the vibration testing side, booms can be tested in other types of fields as well to better verify forced vibration results. Third, the active vibration control by redesigning the connections of the three-parts of the boom can be investigated if higher traveling speed or

measurement accuracy is required. This will potentially increase the height measurement accuracy from the ultrasound sensors. Forth, finalizing the 3rd generation robotic arm design and testing its performance after fabrication should be done. The mechanical structure of the proposed robotic arm shall be determined, finalized, and manufactured. After fabrication, the actual robotic arm shall be tested to verify the theory and investigate its actual performance. Furthermore, since this robotic arm has a long-reach and several flexible joints, it shall be analyzed for vibration characteristics to achieve autonomous data collection with higher accuracy and faster speed. The results can be critically evaluated and implemented to active vibration control, if necessary.

References

[1] I. U. W. a. W. FAO, "The state of food in security and nutrition in the world 2017," FAO, Rome, 2017.

[2] D. o. E. a. S. A. P. D. United Nations, "World population prospects: the 2017 revision," United Nations, New York, 2017.

[3] M. Tester and P. Langridge, "Breeding technologies to increase crop production in a changing world," *Science,* vol. 327, no. 5967, pp. 818-822, 2010.

[4] J. L. Araus and J. E. Cairns, "Field high-throughput phenotyping: the new crop breeding frontier," *Trends in plant Science,* vol. 19, no. 1, pp. 52-61, 2014.

[5] M. E. Ghanem, H. Marrou and T. R. Sinclair, "Physiological phenotyping of plants for crop improvement," *Trends in Plant Science,* vol. 20, no. 3, pp. 139-144, 2015.

[6] J. W. White, P. Andrade-Sanchez, M. A. Gore, K. F. Bronson, T. A. Coffelt, M. M. Conley, K. A. Feldmann, A. N. French, J. T. Heun, D. J. Hunsaker, M. A. Jenks, B. A. Kimball, R. L. Roth, R. J. Strand, K. R. Thorp, G. W. Wall and G. Wang, "Field-based phenomics for plant genetics research," *Field Crops Research,* vol. 133, no. 11, pp. 101-112, 2012.

[7] C. Zhang and J. M. Kovacs, "The application of small unmanned aerial systems for precision agriculture: a review," *Precision Agriculture,* vol. 13, no. 6, pp. 693-712, 2012.

[8] D. Xiao, L. Gong, C. Liu and Y. Huang, "Phenotype-based robotic screening platform for leafy plant breeding," *IFCA,* vol. 49, no. 16, pp. 237-241, 2016.

[9] L. Li, Q. Zhang and D. Huang, "A review of imaging techniques for plant phenotyping," *Sensors,* vol. 14, no. 11, pp. 20078-20111, 2014.

[10] J. F. Humplík, D. Lazár, A. Husičková and L. Spíchal, "Automated phenotyping of plant shoots using imaging methods for analysis of plant stress responses – a review," *Plant methods,* vol. 11, no. 1, p. 29, 2015.

[11] "The economic impact of canola on the Canadian economy," LMC international, 2016.

[12] S. Sankaran, L. R. Khot, C. Z. Espinoza, S. Jarolmasjed, V. R. Sathuvalli, G. J. Vandemark, P. N. Miklas, A. H. Carter, M. O. Pumphrey, N. R. Knowles and M. J. Pavek, "Low-altitude, high-resolution aerial imaging systems for row and field crop phenotyping: A review," *European Journal of Agronomy,* vol. 70, pp. 112-123, 2015.

[13] Y. Shi, J. Thomasson, S. C. Murray, N. A. Pugh, W. L. Rooney, S. Shafian, N. Rajan, G. Rouze, C. L. S. Morgan, H. L. Neely, A. Rana, M. V. Bagavathiannan, J. Henrickson, E. Bowden, J. Valasek, J. Olsenholler, M. P. Bishop, R. Sheridan, E. B. Putman, S. Popescu, T. Burks, D. Cope, A. Ibrahim, B. F. McCutchen, D. D. Baltensperger, R. V. J. Avant,, M. Vidrine and C. Yang, "Unmanned aerial vehicles for high-throughput phenotyping and agronomic research," *PLoS ONE,* vol. 11, no. 7, 2016.

[14] A. F. Martins, M. Bessant, L. Manukyan and M. C. Milinkovitch, "R2OBBIE-3D, a fast robotic high-resolution system for quantitative phenotyping of surface geometry and colour-texture," *PLoS ONE,* vol. 10, no. 6, 2015.

[15] N. Yazdanbakhsh and J. Fisahn, "High throughput phenotyping of root growth dynamics, lateral root information, root architecture and root hair development enabled by PlaRoM," *Functional Plant Biology,* vol. 36, no. 11, pp. 938-946, 2009.

[16] R. R. Mir, M. Thudi, S. K. Chamarthi, L. Krishnamurthy, P. M. Gaur and R. K. Varshney, "Translational root genomics for crop improvement," in *Root genomics and soil interactions*, Oxford, John Wiley & Sons, Inc., 2013, pp. 249-265.

[17] R. C. Kuijken, F. A. Eeuwijk, L. F. Marcelis and H. J. Bouwmeester, "Root phenotyping: from component trait in the lab to breeding," *Journal of experimental botany*, vol. 66, no. 18, pp. 5389-5401, 2015.

[18] J. Zhang, L. Gong, C. Liu, Y. Huang, D. Zhang and Z. Yuan, "Field phenotyping robot design and validation for the crop breeding," *IFAC,* vol. 46, no. 16, pp. 281-286, 2016.

[19] N. Virlet, K. Sabermanesh, P. Sadeghi-Tehran and M. J. Hawkesford, "Field Scanalyzer: an automated robotic field phenotyping platform for detailed crop monitoring," *Functional Plant Biology,* vol. 44, no. 1, pp. 143-153, 2017.

[20] P. Sadeghi-Tehran, K. Sabermanesh, N. Virlet and M. J. Hawkesford, "Automated method to determine two critical growth stages of wheat: heading and flowering," *Frontiers Plant Science,* vol. 8, p. 252, 2017.

[21] J. Barker III, N. Zhang, J. Sharon, R. Steeves, X. Wang, Y. Wei and J. Poland, "Development of a field-based high-throughput mobile phenotyping platform," *Computers and Electronics in Agriculture,* vol. 122, pp. 74-85, 2016.

[22] J. W. Baker, "Development of a field-based high-throughput mobile phenotyping platform," 2014. [Online]. Available: https://krex.k-state.edu/dspace/handle/2097/17543. [Accessed 15 January 2018].

[23] A. Ruckelshausen, P. Biber, M. Dorna, H. Gremmes, R. Klose, A. Linz, R. Rache, R. Resch, M. Thiel, D. Trautz and U. Weiss, "BoniRob: an autonomous field robot platform

for individual plant phenotyping," in *7th European Conference on Precision Agriculture*, Wageningen, Netherlands, 2009.

[24] I. Burud, G. Lange, M. Lillemo, E. Bleken, L. Grimstad and P. J. From, "Exploring robots and UAVs as phenotyping tools in plant breeding," *IFAC-PapersOnLine*, vol. 50, no. 1, pp. 11479-11484, 2017.

[25] S. Vijayarangan, P. Sodhi, P. Kini, J. Bourne, S. Hu, H. Sun, B. poczos, D. Apostolopoulos and D. Wettergreen, "High-throughput robotic phenotyping of energy sorghum crops," in *Field and Service Robotics*, Zurich, 2017.

[26] M. G. S. Fernandez, Y. Bao, L. Tang and P. S. Schnable, "A high-throughput, field-based phenotyping technology for tall biomass crops," *Plant Physiol*, vol. 17, no. 4, pp. 2008-2022, 2017.

[27] A. Kicherer, K. Herzog, M. Pflanz, M. Wieland, P. Rüger, S. Kecke, H. Kuhlmann and R. Töpfer, "An automated field phenotyping pipeline for application in grapevine research," *Sensors*, vol. 15, no. 3, pp. 4823-4836, 2015.

[28] P. Andrade-Sanchez, . J. T. Heun, M. A. Gore, A. N. French, E. Carmo-Silva and M. E. Salvucci, "Use of a moving platform for field deployment of plant," in *Proceedings of the 2012 ASABE Annual International Meeting*, Dallas, TX, 2012.

[29] C. Urrea, J. Cortés and J. Pascal, "Design, construction and control of a SCARA manipulator with 6 degrees of freedom," *Journal of Applied Research and Technology*, vol. 14, no. 6, pp. 296-404, 2016.

[30] Y. Tao, F. Chen and H. Xiong, "Kinematics and workspace of a 4-DOF hybrid palletizing robot," *Advances in Mechanical Engineering*, vol. 6, 2015.

[31] B. Gherman, D. Pisla, C. Vaida and N. Plitea, "Development of inverse dynamic model for a surgical hybrid parallel robot with equivalent lumped masses," *Robotics and Computer-Integrated Manufacturing*, vol. 28, no. 3, pp. 402-415, 2012.

[32] T. Mueller-Sim, M. Jenkins, J. Abel and G. Kantor, "The Robotanist: a ground-based agricultural robot for high-throughput crop phenotyping," in *IEEE International Conference on Robotics and Automation (ICRA)*, Singapore, 2017.

[33] A. Shafiekhani, S. Kadam, F. B. Fritschi and G. N. DeSouza, "Vinobot and Vinoculer: two robotic platforms for high-throughput field phenotyping," *Sensors*, vol. 17, no. 1, p. 214, 2017.

[34] S. S. Rao, Mechanical Vibrations, Upper Saddle River, NJ: Prentice Hall, 2011.

[35] J. J. Craig, Introduction to robotics: mechanics and control, Third ed., Upper Saddle River, NJ: Pearson Education, Inc., 2004.

[36] W. Zhang, Y. Lin and N. Sinha, "On the Function-Behavior-Structure Model for Design," *Proceedings of the Canadian Engineering Education Association,* 2011.

Appendix A: Amplifier type 2635 from Bruel & Kjar.

Refer to chapter 3 section 3.1 this is about. Amplifiers, type 2635, have 3 different channels to measure acceleration, velocity, and displacement. Before tests, acceleration and displacement channel are calibrated individually in the lab environment. It is a four-stage amplifier consisting of an input amplifier, low-pass filter-amplifier, integrator amplifier, and output amplifier. Since the observation shows the boom vibrates at low-frequency, the amplifier is set up to measure the vibration between 10 to 100 Hz. This configuration allows accurate measurement in this range and damps other frequencies. These amplifiers can measure off-limit frequency depending on the frequency and amplitude. Bruel & Kjar amplifier's profile is demonstrated in the following Figure A.1.

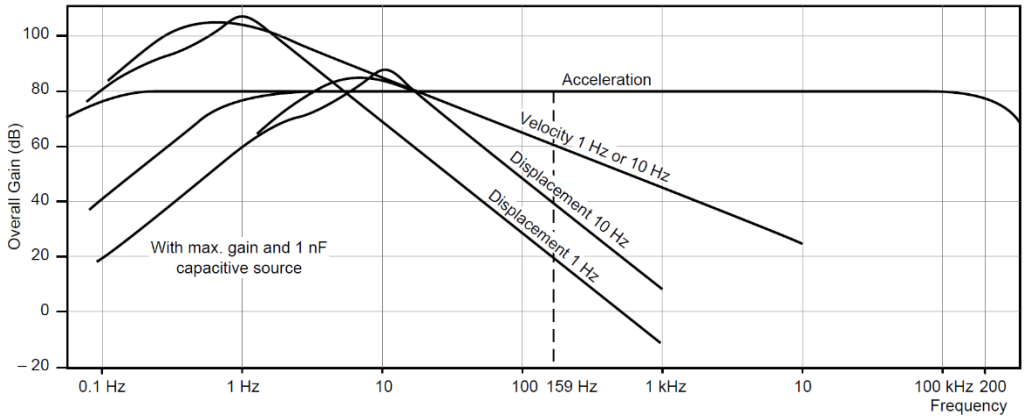

Figure A.1: Amplifier Profile from Bruel & Kjar

The displacement at 1Hz is measured as 10mm/V is the lab setting. In the experiment shown in Figure 3.3, the output frequency from the shaker table was set to 1 Hz. After adjusting the amplifier, the voltage difference between the peak and valley is 1V on the oscilloscope when actual reading from the laser measurement is 10 mm. Thus, the relationship between voltage and displacement is determined.

Appendix B: Analytical Solution of Vibrations of C-channel Boom

This section shows the hand calculation of 1st mode vibration frequency of the C-channel in 2nd gen boom discussed in chapter 3 section 3.2.3. The dimension of this 5x6.7 C-channel is shown in Figure B.1 where all dimensions are in inches,

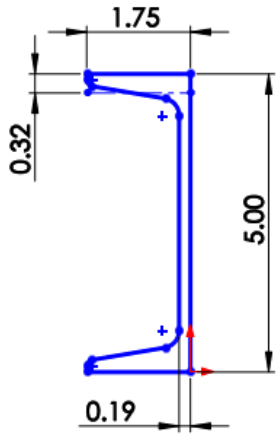

Figure B.1: Cross-Section of the 5x6.7 C-channel Steel Structure Beam

From S. Rao *Mechanical Vibrations* [34],

$$\omega = (\beta l)^2 \sqrt{\frac{EI}{\rho A l^4}}$$

Where, f, natural frequency of vibration is ω/2π,

E, Young's modulus is 200 GPa,

I, area moment of inertia 3102808 mm^4,

ρ, material density is 7800kg/m^3,

A, cross-section area is 1257 mm^2,

l, length of the beam is 3 m,

and $\beta_1 l$ = 1.875 for first mode vibration.

$$f = \frac{\omega}{2\pi} = \frac{(\beta l)^2}{2\pi} \sqrt{\frac{EI}{\rho A l^4}} = \frac{(1.875)^2}{2\pi} \sqrt{\frac{200GPa * 3102808mm^4}{7800kg/m^3 * 1257mm^2 * (3m)^4}} = 15.641\ Hz$$

Appendix C: ANSYS Code for Vibration Verification

This section shows the code in ANSYS Classic used for vibration analysis of the same 5x6.7 C-channel in the previous chapter 3 section 3.2.3. There are two parts of the code where the first one analyzes the natural frequency of the C-channel with Beam188, and the second part solves the vibration with transient analysis when an instant load is applied for 0.0001s.

```
/clear
/prep7
/PNUM,KP,1                          !Show keypoints
/PNUM,LINE,1
/PNUM,NODE,1
NoEl = 8                            ! number of elements
*SET,g,9.81

K,1,0,0
K,2,3,0
L,1,2
ET,1,BEAM188
SECTYPE, 1, BEAM, CHAN, Center, 4
SECOFFSET, CENT
SECDATA,0.0444,0.0444,.127,.008135,.008135,.00483,0,0,0,0,0,0
MP,EX,1,200E9
MP,PRXY,,0.3
MP,DENS,1,7800                      ! Density lbs/in^3

LESIZE, ALL,,,NoEl                  ! Element size
SECNUM,1                            ! turn on section property set #1
LMESH,1                             ! LMESH,1,7,1

FINISH
/SOLU
ANTYPE,2                            ! Modal analysis
MODOPT,SUBSP,5                      ! Subspace, 5 modes
EQSLV,FRONT                         ! Frontal solver
MXPAND,5                            ! Expand 5 modes

NSEL,S,,,2,1+NoEl,
!D,ALL,UZ,,,,,ROTX,ROTY
D,ALL,UY,,,,,ROTX,ROTZ
!M,All,UY,,,UX,ROTZ,                ! Define Master DOFs
NSEL,ALL
D,1,ALL                             ! Constrain key point one

SOLVE
FINISH

/POST1                              ! List solutions
SET,LIST
SET,FIRST
PLDISP                              ! Display first mode shape
ANMODE,10,0.5, ,0                   ! Animate mode shape
```

The following codes are used for transient analysis

```
FINISH
/SOLU                          ! Enter solution phase
timeStp = .0001

ANTYPE, TRANS                  ! Transient analysis
TRNOPT,REDUC,                  ! reduced solution method
DELTIM,timeStp                 ! Specifies the time step sizes

!At time equals 0s
NSEL,S,,,2,1+NoEl,             ! select nodes 2 - 11
D,ALL,UY,,,,,ROTX,ROTZ
M,All,UZ, , ,                  ! Define Master DOFs
NSEL,ALL                       ! Reselect all nodes
D,1,ALL                        ! Constrain left end

! Load Step 1
TIME, timeStp
AUTOTS,1
DELTIM,timeStp, , ,1
KBC,0
TSRES,ERASE
LSWRITE,1,

! Load Step 2
F,2,FZ,-100
TIME,timeStp*2
AUTOTS,1
DELTIM,timeStp, , ,1
KBC,0
TSRES,ERASE
LSWRITE,2,

!Load Step 3
FDELE,2,ALL
TIME,5                         ! Maximum Time
AUTOTS,1
DELTIM,timeStp, , ,1
KBC,0
TSRES,ERASE
LSWRITE,3,

LSSOLVE,1,3,1                  ! solve multiple load steps

FINISH
/POST26                        ! Enter time history
```

Appendix D: Frequency Analysis Results

Refer to chapter 3 section 3.3 this is about. This part shows the vibration test results from different data using FFT method. It includes results from all applied sensors in each test and calculated three most outstanding frequencies with their peak value.

Vibration Analyzation Results from Acceleration Measurements on May 31, 2017

	Sensor 1			Sensor 2		
Scope #	First	Second	Third	First	Second	Third
1	3.0	44.0	31.0	4.0	31.0	63.0
Amplitude	0.6983	0.3205	0.2134	2.4068	0.4948	0.3985
2	2.0	45.0	25.0	5.0	21.0	132.0
Amplitude	0.6628	0.2846	0.1518	1.8732	0.4529	0.2726
3	45.0	4.0	30.0	7.0	133.0	30.0
Amplitude	0.4454	0.4168	0.1154	0.7765	0.3497	0.3245
4	46.0	4.0	31.0	4.0	63.0	132.0
Amplitude	0.3854	0.2591	0.1098	1.9407	0.3503	0.2601
5	9.0	45.0	31.0	4.0	31.0	63.0
Amplitude	0.4650	0.3335	0.1525	1.9468	0.3523	0.3487
6	36.0	48.0	6.0	4.0	46.0	59.0
Amplitude	0.2655	0.1393	0.1135	1.0479	0.5187	0.3118
7	36.0	48.0	5.0	4.0	47.0	178.0
Amplitude	0.2778	0.2191	0.1304	0.7895	0.4411	0.4290
8	45.0	83.0	23.0	5.0	45.0	23.0
Amplitude	0.8418	0.1070	0.0960	1.2079	1.0707	0.4053
9	45.0	1.0	19.0	45.0	5.0	179.0
Amplitude	0.8492	0.1873	0.1089	1.1105	0.7304	0.4026
10	44.2	82.1	56.9	3.2	44.2	82.1
Amplitude	0.7434	0.2152	0.0884	1.1839	0.8661	0.5131
11	4.0	19.0	45.0	4.0	19.0	90.0
Amplitude	0.9469	0.2577	0.1934	0.9158	0.2473	0.2091
12	4.0	131.0	64.0	4.0	131.0	64.0
Amplitude	1.8932	0.6048	0.3212	1.9665	0.6079	0.3155
13	3.0	34.0	50.0	4.0	31.0	62.0
Amplitude	2.0124	0.6409	0.6379	2.0312	0.4335	0.2973
14	4.0	44.0	82.0	4.0	131.0	31.0
Amplitude	1.6537	0.6542	0.6046	1.8322	0.3395	0.3371
15	4.0	44.0	89.0	4.0	31.0	64.0
Amplitude	1.9127	0.5212	0.4613	1.9802	0.3155	0.2195
16	4.0	44.0	83.0	5.0	132.0	63.0
Amplitude	1.4722	0.8804	0.5428	1.7567	0.4264	0.2397
17	4.0	45.0	83.0	4.0	45.0	131.0

Amplitude	1.4216	1.0168	0.5253	1.0253	0.2151	0.2038
18	43.0	138.0	7.0	4.0	132.0	43.0
Amplitude	0.7079	0.5776	0.5730	1.3060	0.2944	0.2592
19	5.0	44.0	63.0	5.0	63.0	22.0
Amplitude	1.8563	0.5004	0.4000	2.5825	0.3406	0.3010
20	4.0	45.0	64.0	4.0	64.0	30.0
Amplitude	1.5802	0.6781	0.4214	1.8196	0.3882	0.3158
21	5.0	44.0	63.0	5.0	63.0	31.0
Amplitude	1.9598	0.5923	0.4411	2.2723	0.4554	0.4042
22	4.0	44.0	17.0	5.0	131.0	44.0
Amplitude	1.8966	0.8227	0.2046	1.4134	0.3183	0.3037
23	45.0	2.0	14.0	2.0	45.0	136.0
Amplitude	0.3985	0.3579	0.0903	0.2970	0.2290	0.1316
24	45.0	3.0	89.0	4.0	45.0	137.0
Amplitude	0.3332	0.3260	0.0885	0.2412	0.2184	0.1177
25	45.0	3.0	31.0	3.0	45.0	179.0
Amplitude	0.5429	0.4191	0.0890	0.4142	0.2662	0.1111
26	44.0	3.0	30.0	3.0	44.0	175.0
Amplitude	0.5813	0.3005	0.2044	0.3182	0.1938	0.1193
27	44.0	8.0	32.0	1.0	44.0	174.0
Amplitude	0.3944	0.2757	0.2088	0.1780	0.1614	0.0954
28	44.0	5.0	22.0	44.0	5.0	87.0
Amplitude	0.5322	0.1268	0.1015	2.5839	0.1600	0.1382
29	44.0	172.1	33.0	44.0	1.0	55.0
Amplitude	0.7710	0.1321	0.1316	2.6383	0.2519	0.2113
30	46.0	1.0	35.0	46.0	1.0	183.1
Amplitude	0.2375	0.1908	0.1668	2.3544	0.2819	0.1641
31	44.0	1.0	34.0	44.0	1.0	174.1
Amplitude	0.8473	0.3983	0.2020	3.2953	0.4023	0.1283
32	45.0	1.0	83.0	45.0	1.0	180.1
Amplitude	0.7321	0.3055	0.1182	2.6625	0.2280	0.1377
33	158.5	31.7	16.7	63.4	131.8	158.5
Amplitude	0.9898	0.5965	0.1482	3.8368	2.4983	1.7058
34	158.0	32.0	90.0	64.0	158.0	134.0
Amplitude	0.4407	0.1758	0.0621	2.7756	0.9223	0.8077
35	158.0	84.0	26.0	26.0	4.0	160.0
Amplitude	0.3229	0.1775	0.1403	2.1007	1.3176	0.7533
36	157.2	83.1	36.0	26.0	83.1	157.2
Amplitude	0.9021	0.7469	0.3050	1.9412	1.7975	1.4368

Vibration Analyzation Results from Displacement Measurements on July 25, 2017

	Sensor 1			Sensor 2		
Scope #	First	Second	Third	First	Second	Third
2	1.1	5.0	7.4	9.3	7.2	5.1
Amplitude	0.5511	0.1552	0.0968	0.0420	0.0337	0.0260
3	1.4	5.7	9.9	9.0	6.8	11.8
Amplitude	0.3924	0.1576	0.0797	0.0295	0.0242	0.0207
4	120.2	146.9	155.3	1.6	4.3	7.3
Amplitude	0.0125	0.0123	0.0111	0.1820	0.0952	0.0750
5	4.4	8.8	12.8	4.4	8.8	12.8
Amplitude	0.0725	0.0288	0.0249	0.0873	0.0358	0.0217
6	4.4	9.0	12.8	4.4	29.4	6.8
Amplitude	0.1184	0.0289	0.0279	0.1356	0.0175	0.0087
7	4.3	30.2	12.0	4.3	30.2	8.9
Amplitude	0.0904	0.0616	0.0116	0.1098	0.0592	0.0261
8	4.3	29.0	12.8	8.7	4.4	29.5
Amplitude	0.1211	0.0263	0.0253	0.0264	0.0188	0.0124
9	4.3	29.9	11.9	29.9	12.8	8.5
Amplitude	0.1450	0.0557	0.0127	0.0244	0.0088	0.0058
10	4.1	8.5	12.0	4.1	8.7	10.9
Amplitude	0.1309	0.0320	0.0258	0.0227	0.0081	0.0079
11	4.3	29.9	11.4	4.3	29.9	9.1
Amplitude	0.1587	0.0376	0.0128	0.0165	0.0078	0.0056
12	4.4	9.6	13.5	4.4	9.0	12.0
Amplitude	0.0358	0.0221	0.0120	0.0265	0.0172	0.0053
13	30.0	12.8	4.4	4.4	29.8	8.2
Amplitude	0.0227	0.0176	0.0072	0.0126	0.0079	0.0050
14	11.3	9.2	29.6	12.2	8.8	29.6
Amplitude	0.0527	0.0255	0.0156	0.0179	0.0159	0.0074
15	11.9	8.7	22.9	12.5	10.3	2.6
Amplitude	0.0854	0.0228	0.0078	0.0560	0.0299	0.0129
16	12.7	9.3	4.8	12.7	5.0	7.3
Amplitude	0.2380	0.0637	0.0323	0.1556	0.0401	0.0331
17	11.9	4.2	23.2	11.7	9.5	9.5
Amplitude	0.0640	0.0480	0.0327	0.1106	0.0479	0.0479
18	11.9	9.8	4.5	11.9	9.5	2.7
Amplitude	0.2378	0.0463	0.0329	0.1017	0.0388	0.0253
19	12.2	4.2	14.6	12.4	10.1	14.6
Amplitude	0.0861	0.0559	0.0412	0.0937	0.0331	0.0312
20	30.0	4.2	12.5	30.0	12.8	16.5
Amplitude	0.0780	0.0718	0.0111	0.0381	0.0080	0.0052
21	4.2	8.6	29.0	8.6	4.4	29.0
Amplitude	0.0715	0.0217	0.0204	0.0274	0.0168	0.0088
22	4.4	29.1	8.7	4.2	8.8	29.1
Amplitude	0.0544	0.0303	0.0210	0.0599	0.0582	0.0281
23	30.0	4.3	12.3	4.5	30.0	11.1
Amplitude	0.0719	0.0666	0.0119	0.0708	0.0679	0.0201

Vibration Analyzation Results from Displacement Measurements on Oct 05, 2017

	Sensor 1 (Yellow)			Sensor 2 (Blue)			Sensor 3 (Green)		
Scope #	First	Second	Third	First	Second	Third	First	Second	Third
4	1.0	1.2	2.6	2.6	2.1	2.4	1.0	2.6	0.8
Amplitude	0.0417	0.0381	0.0332	0.0331	0.0325	0.0309	0.0402	0.0337	0.0325
5	0.2	2.3	2.5	2.3	2.5	2.0	1.0	1.2	0.2
Amplitude	0.0704	0.0430	0.0393	0.0413	0.0387	0.0307	0.0431	0.0416	0.0371
6	0.2	2.6	2.3	0.3	2.6	2.4	2.1	1.1	2.3
Amplitude	0.0490	0.0369	0.0324	0.0272	0.0228	0.0184	0.0551	0.0287	0.0249
7	2.4	2.6	2.2	0.3	2.4	2.6	2.2	1.1	0.9
Amplitude	0.0369	0.0321	0.0304	0.0256	0.0218	0.0192	0.0602	0.0395	0.0358
8	2.1	3.4	1.8	2.1	1.8	1.6	1.1	0.9	1.2
Amplitude	0.1791	0.0365	0.0313	0.0895	0.0164	0.0152	0.0802	0.0706	0.0684
9	0.9	1.1	1.3	0.9	1.1	1.3	0.9	1.1	1.3
Amplitude	0.8658	0.4586	0.3065	0.7751	0.3977	0.2926	0.4581	0.3138	0.2696
10	1.1	0.9	1.7	1.1	0.9	0.6	0.6	1.2	1.5
Amplitude	0.7838	0.2547	0.1714	0.4597	0.1680	0.1495	0.1242	0.1100	0.1067
11	1.2	0.9	0.8	1.2	0.9	0.6	1.2	0.6	1.8
Amplitude	0.7127	0.4262	0.2707	0.4666	0.2412	0.2167	0.1916	0.1492	0.0798
12	1.1	0.9	1.2	1.1	0.9	1.2	1.2	0.6	1.5
Amplitude	0.5643	0.4296	0.2857	0.3406	0.2429	0.2148	0.1935	0.1255	0.1093
13	1.2	0.9	1.8	1.2	1.5	1.8	1.2	1.5	1.8
Amplitude	0.3855	0.3310	0.2822	0.2611	0.2045	0.1850	0.2290	0.1724	0.1563
14	1.0	1.2	1.8	0.6	1.2	1.8	1.2	1.8	1.5
Amplitude	0.3035	0.2938	0.2612	0.2079	0.2034	0.1997	0.2097	0.1650	0.1444
15	1.1	0.6	1.6	0.6	1.2	1.8	1.2	0.6	1.8
Amplitude	0.3691	0.3043	0.2604	0.2588	0.1984	0.1648	0.2161	0.1884	0.1515
16	1.2	0.6	1.5	1.1	0.6	0.9	1.2	0.6	1.8
Amplitude	0.1180	0.1064	0.0484	0.1183	0.1146	0.0645	0.1575	0.1391	0.1231
17	1.0	1.2	0.6	1.0	0.6	1.2	1.0	0.6	1.2
Amplitude	0.0836	0.0729	0.0682	0.1158	0.0936	0.0862	0.1163	0.1050	0.0830
18	1.1	1.2	0.6	0.6	1.0	1.8	1.5	1.2	0.6
Amplitude	0.2320	0.1749	0.1716	0.1075	0.1044	0.0794	0.1544	0.1515	0.1495
19	124.0	88.0	160.0	124.0	88.0	214.0	588.0	124.0	534.0
Amplitude	0.1316	0.1304	0.0860	0.1512	0.1396	0.1344	0.0665	0.0630	0.0581
20	4.7	158.6	123.4	4.7	123.4	158.6	4.7	123.4	140.9
Amplitude	0.0931	0.0430	0.0241	0.0693	0.0257	0.0243	0.0516	0.0175	0.0110
21	1.7	1.6	1.9	1.7	1.6	1.9	1.6	1.7	1.9
Amplitude	0.0879	0.0840	0.0702	0.0926	0.0893	0.0666	0.0992	0.0901	0.0786
22	1.7	1.6	0.2	1.7	0.3	0.5	1.7	1.9	0.2
Amplitude	0.0823	0.0556	0.0536	0.0525	0.0521	0.0379	0.0596	0.0437	0.0274
23	1.9	3.3	1.6	1.9	1.7	3.3	1.9	1.7	1.2
Amplitude	0.1563	0.0680	0.0677	0.0791	0.0324	0.0295	0.0810	0.0680	0.0285
24	1.0	1.2	1.4	1.0	1.2	1.4	1.0	1.2	1.4
Amplitude	2.8045	1.1159	0.7493	2.6279	1.0720	0.7350	2.4760	1.3914	1.0021
25	1.0	1.1	1.3	1.0	1.1	1.3	1.0	2.0	1.1
Amplitude	2.8539	2.2039	1.0627	1.6187	1.3143	0.6392	1.0386	0.6379	0.3977
26	1.0	1.3	1.5	1.0	1.3	1.5	1.0	2.0	1.1
Amplitude	3.0804	1.9332	1.1249	1.7211	1.1289	0.7226	0.9441	0.5918	0.3346
27	1.0	1.1	1.3	1.0	1.1	1.3	1.0	2.0	1.2
Amplitude	3.2506	2.3141	1.0201	2.0947	1.4538	0.5261	0.5835	0.5434	0.4157
28	1.0	1.5	2.0	1.0	2.0	1.5	1.0	1.9	1.2
Amplitude	2.6562	0.6689	0.6135	2.0449	0.4676	0.4423	0.6620	0.5511	0.4636
29	1.0	2.0	1.2	1.0	2.0	1.2	1.0	2.0	1.2
Amplitude	1.4970	1.1101	0.8241	1.3533	0.8713	0.4457	0.8293	0.6064	0.3511

30	2.0	1.5	1.0	2.0	1.0	1.2	2.0	1.1	0.9
Amplitude	1.3503	0.7968	0.7678	1.0781	0.8610	0.4661	0.7542	0.5713	0.5330
31	1.0	2.0	1.3	1.2	1.0	1.5	2.0	1.0	1.3
Amplitude	0.5989	0.2476	0.1215	0.3925	0.2712	0.2027	0.6480	0.5217	0.2363
32	1.0	2.0	1.3	1.0	1.2	1.9	2.0	1.0	1.5
Amplitude	0.6699	0.2839	0.1523	0.4686	0.3102	0.2239	0.7472	0.6102	0.1984
33	1.0	2.0	1.2	1.0	1.2	2.0	2.0	1.0	1.2
Amplitude	0.4784	0.2573	0.1474	0.5432	0.4141	0.2324	0.6006	0.5094	0.3681
34	10.0	2.0	87.9	10.0	87.9	2.0	2.0	10.0	6.2
Amplitude	0.1864	0.0877	0.0758	0.1029	0.0797	0.0792	0.0828	0.0337	0.0279
35	10.1	1.2	90.5	10.1	90.4	0.9	10.1	2.0	90.4
Amplitude	0.2985	0.1022	0.0646	0.1722	0.0735	0.0633	0.0603	0.0579	0.0359
36	2.0	55.6	15.1	2.0	21.2	55.6	2.0	137.4	157.4
Amplitude	0.1460	0.0761	0.0501	0.1299	0.0628	0.0436	0.0851	0.0499	0.0431
37	1.4	0.9	0.7	1.4	0.9	1.2	1.3	1.8	2.7
Amplitude	2.9956	2.7184	0.5264	2.0054	1.7281	1.2737	0.5635	0.4163	0.4032
38	1.4	1.2	1.0	1.4	1.2	1.0	2.7	2.2	1.5
Amplitude	2.1973	2.1751	1.8444	1.5787	1.3975	1.1469	0.5239	0.4852	0.4393
39	2.8	2.5	3.4	2.8	1.4	2.5	2.8	1.4	2.5
Amplitude	4.0348	1.1515	0.8701	2.1916	0.7886	0.6964	0.9992	0.4098	0.4043

Appendix E: SIMULINK Model of the Robotic Arm

This section shows the details of SIMULINK model of the robotic arm in chapter 4 section 4.3. Figure E.1 shows the detailed whole SIMULINK model of the 3rd generation robotic arm, and Figure E.2 shows the simplified version with masks to each subsystem. The details of each subsystem are demonstrated in Figure E.3 to Figure E.10.

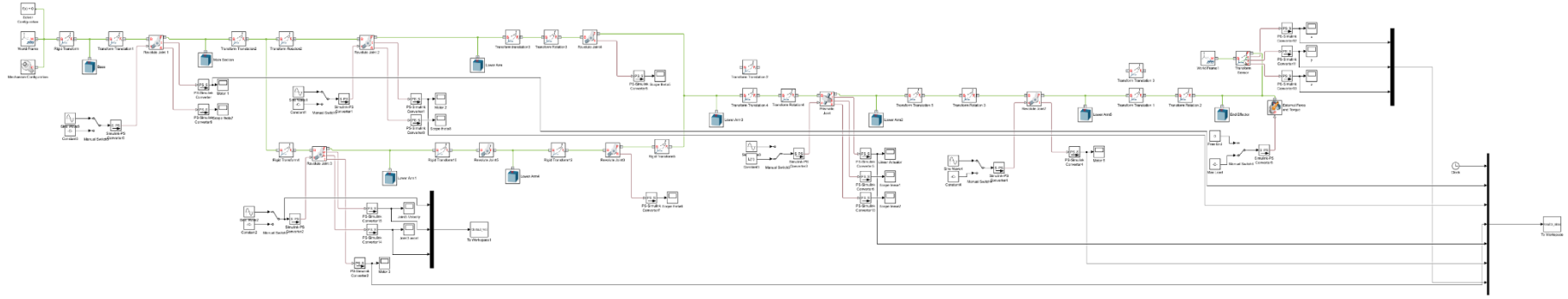

Figure E.1: Detailed Layout of the SIMULINK Model of the Robotic Arm

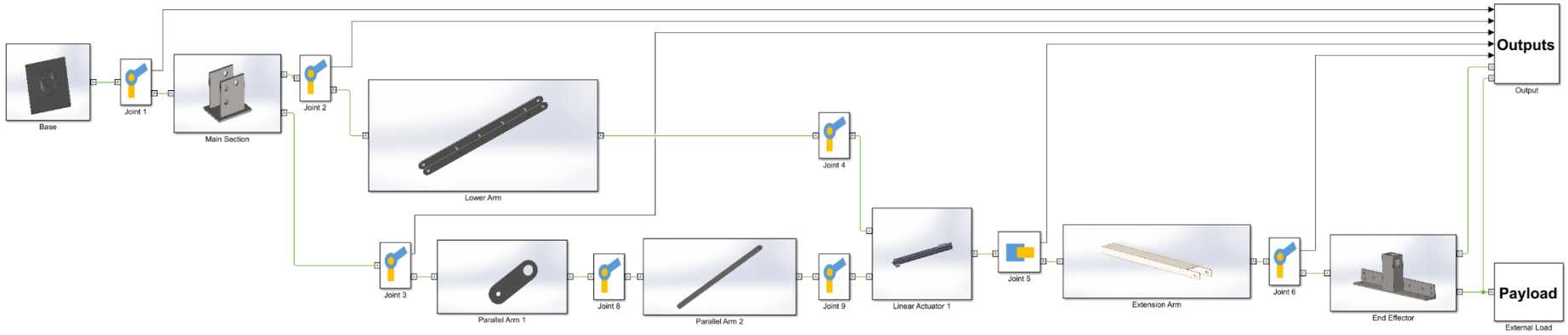

Figure E.2: Layout of the SIMULINK Model of the Robotic Arm with Masks to Subsystem

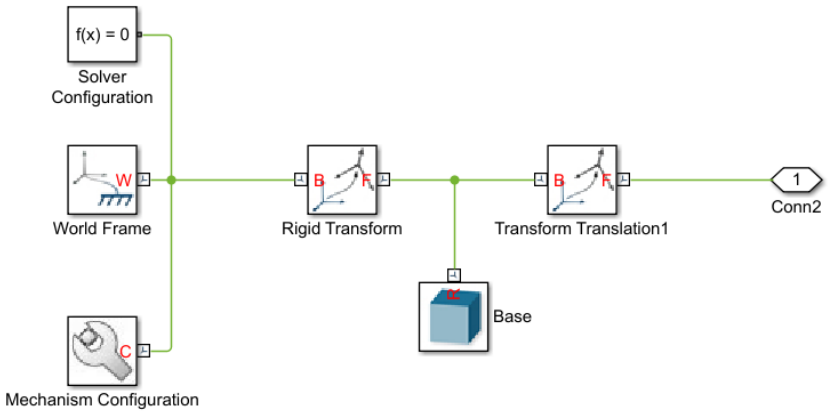

Figure E.3: Layout of the Base Subsystem in the SIMULINK Model

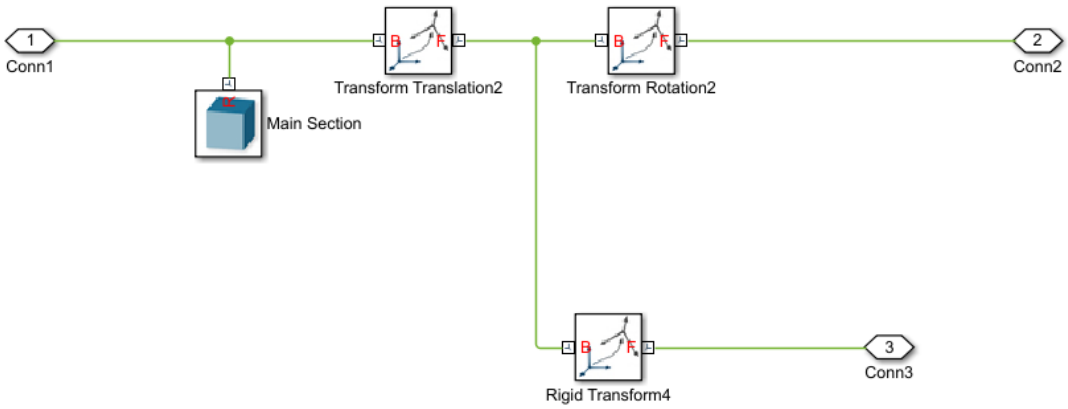

Figure E.4: Layout of the Main Section Subsystem in the SIMULINK Model

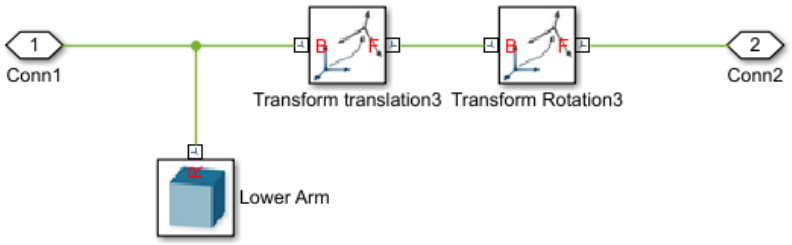

Figure E.5: Layout of the Lower Arm Subsystem in the SIMULINK Model

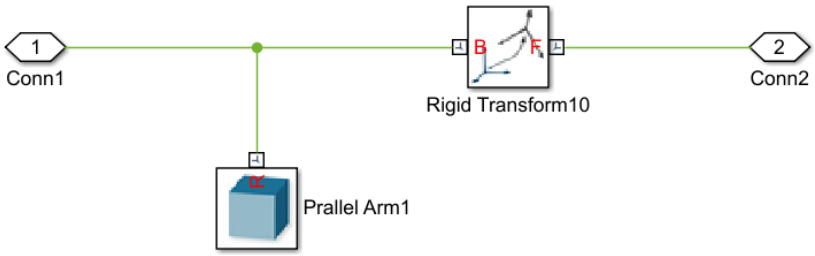

Figure E.6: Layout of the Parallel Arm 1 Subsystem in the SIMULINK Model

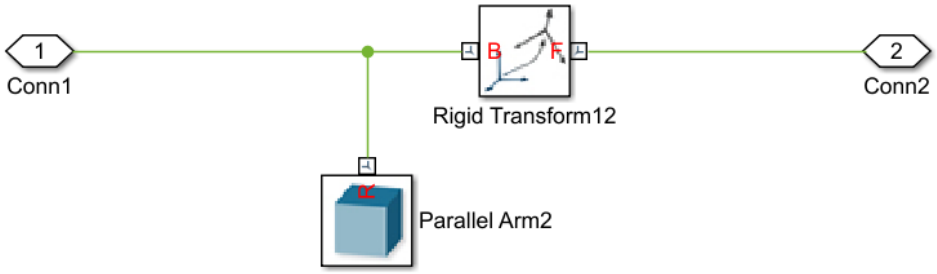

Figure E.7: Layout of the Parallel Arm 2 Subsystem in the SIMULINK Model

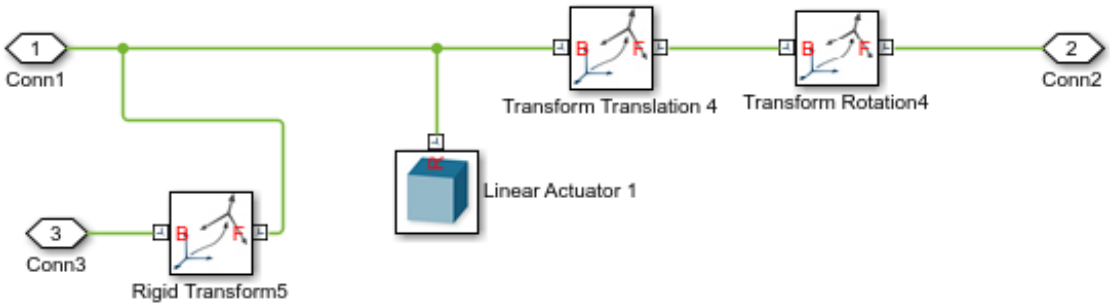

Figure E.8: Layout of the Linear Actuator Subsystem in the SIMULINK Model

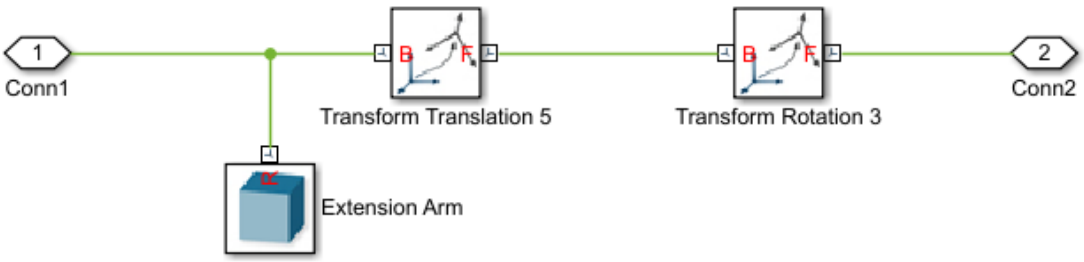

Figure E.9: Layout of the Extension Arm Subsystem in the SIMULINK Model

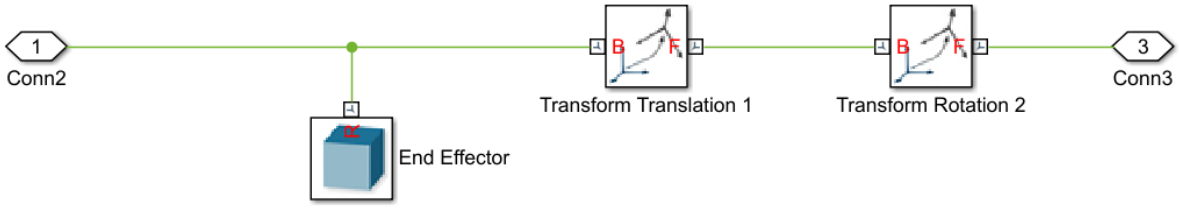

Figure E.10: Layout of the End Effector Subsystem in the SIMULINK Model